Ph.D. Dissertation of natural sciences

Mechanisms of the interannual to decadal thermal variability of the upper ocean in the western boundary region of the North Pacific

북태평양 서안 경계 해역의 상층 열용량 장기 변동 기작 연구

February 2017

Graduate School of Earth and Environmental Sciences
Seoul National University
Physical Oceanography Major

Gyundo Pak

Abstract

Mechanisms of the interannual to decadal thermal variability of the upper ocean in the western boundary region of the North Pacific

Gyundo Pak
The Graduate School of Earth and Environmental Sciences, Seoul National University
Dual Ph.D. Program with Université Pierre et Marie CURIE (Paris VI), France

Winter upper-ocean heat content variability and its causal mechanisms are investigated using observational and reanalysis products in the western North Pacific. The relationship between the East Asian winter monsoon (EAWM) and the North Pacific Oscillation (NPO) and their impact on the sea surface temperature (SST) are nonstationary, with a sudden change at 1987/1988. During the 1973–87, the EAWM and NPO were significantly correlated to each other, but their correlation practically vanishes during the 1988–2002. This nonstationary relationship is related to the pronounced decadal weakening of the Siberian high after the 1988 regime shift as well as the concomitant positive NPO-like dipole change. The influence of EAWM and NPO to the winter SST in the study region is significantly decreased after the sudden change near-1990. The upper 400 m heat budget in the western North Pacific is analyzed using outputs from a high resolution ocean general circulation model. Winter heat storage rate on interannual to decadal time scales is mainly determined by oceanic heat advection rather than by net air-sea heat flux. The role of heat advection becomes particularly prominent after the 1990 regime shift in association with the reduced variability of surface heat flux caused by weakened SST variability. The net heat flux acts to dampen temperature anomalies caused by the ocean dynamics principally associated with the meridional shift of the Oyashio Extension front, which is significantly correlated with the West Pacific (WP) and Pacific-North America (PNA) teleconnection patterns.

Keyword: Heat budget, Long-term variability, Ocean advection, Air-sea heat flux, Kuroshio-Oyashio Extension, Regime shift
Student Number: 2010-30943

Table of Contents

List of Tables

List of Figures

Chapter 1. Introduction

1.1. Importance of ocean dynamics in the western North Pacific on climate

The western boundary region of the North Pacific including the Kuroshio-Oyashio Extension (KOE) region has been known as the region where the ocean circulation is most variable in the North Pacific [*Nakamura et al.*, 1997; *Qiu*, 2000] due to the inflow of the energetic Kuroshio and Oyashio. In the recent decades (1970-2009), the western boundary regions such as the KOE region show the highest rate of increasing winter sea surface temperature (SST) over the global ocean (Figure 1.1a). Subsurface ocean variability exerts a strong influence on SST in the KOE region, yielding the strongest long-term SST variability in the North Pacific [*Nakamura et al.*, 1997], and strong ocean-atmosphere interaction takes place in the KOE region [*Latif and Barnett*, 1994; *Seager et al.*, 2001; *Schneider et al.*, 2002; *Qiu et al.*, 2007; *Kwon et al.*, 2010; *Frankgnoul et al.*, 2011]. In contrast to the conventional extratropical ocean-atmosphere interaction characterized by atmospheric forcing on SST variations [*Cayan*, 1992], the SST forcing upon the overlying atmosphere is prevalent in the KOE region where ocean dynamics is very important [*Tanimoto et al.*, 2003]. This ocean-to-atmosphere feedback occurs through vigorous turbulent heat fluxes, responsible for considerable oceanic heat release to the atmosphere especially in the boreal winter [*Sugimoto and Hanawa*, 2011], affecting the atmospheric boundary layer and storm track activity [*Nonaka and Xie*, 2003; *Tanimoto et al.*, 2003]. The winter net surface heat flux (Q_{net}) indicates that the heat releases from ocean to atmosphere with strong temporal variability in the KOE region over the North Pacific (Figures 1.1b and 1.1c). These ocean-atmosphere interactions play an important role in generating interannual to decadal climate variability of ocean and atmosphere in local and remote regions in the North Pacific [*Kwon and Deser*, 2007; *Yamamoto and Hirose*, 2011; *Seo et al.*, 2014a]. Oceanic processes can induce remarkable interannual to decadal upper-ocean heat content variability in the KOE region [*Vivier et al.*, 2002; *Kwon and Deser*, 2007], which in turn influence the atmosphere through the SST variability

and resultant turbulent heat flux changes [*Tanimoto et al.*, 2003].

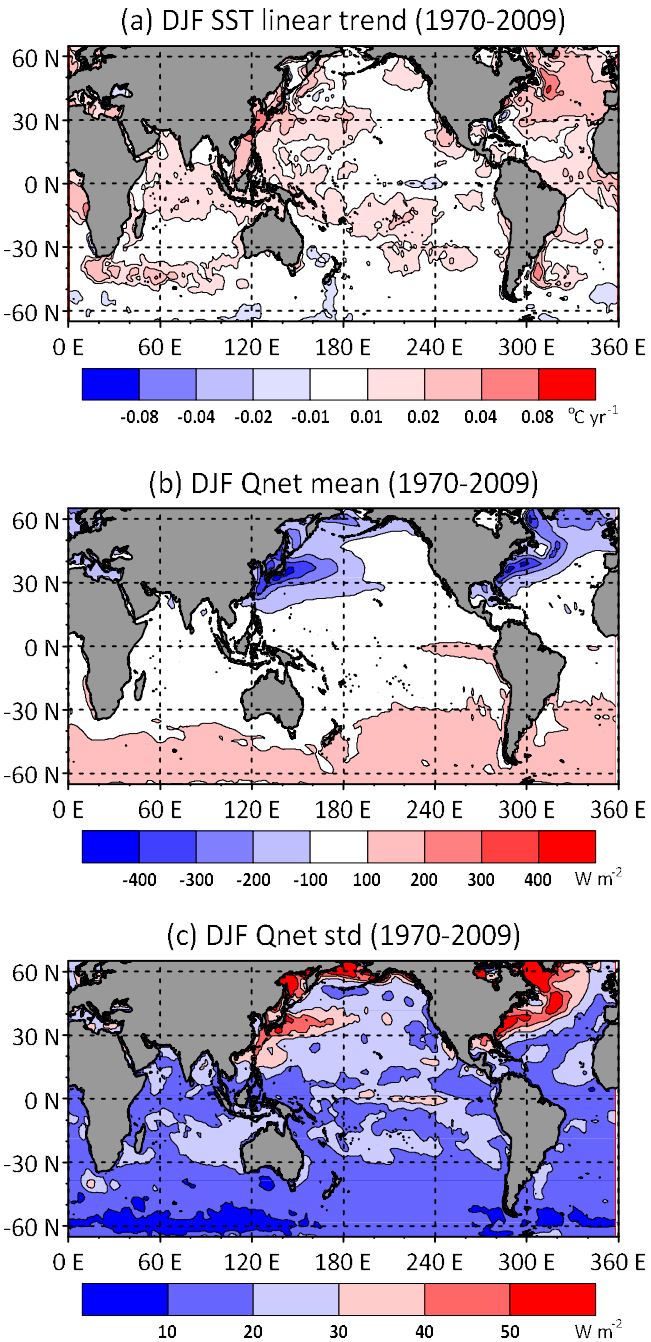

Figure 1.1. Spatial distribution of winter (a) SST linear trends, (b) mean and (c) temporal standard deviation of net surface heat flux for boreal winter (December to February) during 1970–2009. Sign convention for heat flux is downward positive.

1.2. KOE region in the western North Pacific

The Kuroshio Extension (KE) system is well reviewed by *Qiu* [2001] and *Qiu and Chen* [2005]. The KE is the western boundary current extension of the subtropical gyre in the North Pacific. The KE front, located at ~35°N, is strongest between 200 and 600 m below the surface [*Kwon et al.*, 2010]. After separating from the coast of Japan near 35°N, the mean path of the upstream KE is characterized by the presence of two quasi-stationary meanders with their ridges located at 144°E and 150°E, respectively [see Figure 1 of *Qiu and Chen*, 2005]. South of the quasi-stationary meanders, the KE jet is flanked by a tight recirculation gyre, whose existence has been observed to increase the eastward transport of the KE from the local Sverdrup transport value of ~50 to ~130 Sv (where 1 Sv ≡ 10^6 m^3 s^{-1}). Near 159°E, the KE jet encounters the Shatsky Rise where it often bifurcates: the main body of the jet continues eastward, and a secondary branch tends to move northeastward to 40°N where it joins the Subarctic Current. Recent high-resolution observational and modeling data show that there are at least two prominent oceanic frontal zones in the KOE region: along the KE, and the subarctic frontal zone associated with the Oyashio Extension (OE). The OE front is strongest at ~41°N at the surface located in the north of the KE front [*Kwon et al.*, 2010]. *Nonaka et al.* [2008] revealed that the basin-scale wind stress curl and local Ekman pumping can intensify the southward flowing Oyashio via barotropic and baroclinic Rossby wave propagations. Those KE and OE systems are parts of the subtropical and subpolar gyres in the North Pacific, respectively (Figure 1.2). The KOE region mostly consisting of the mixed water between the two extensions is the focus of the thesis.

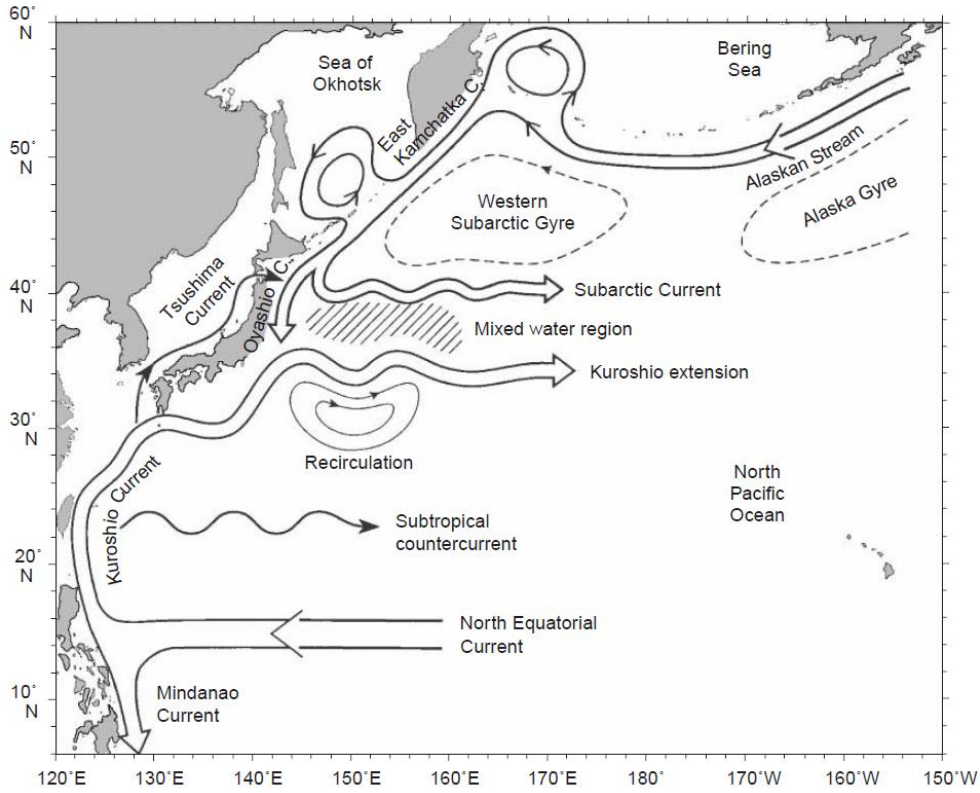

Figure 1.2. Schematic current patterns associated with the subtropical and subarctic gyres in the western North Pacific [*Qiu*, 2001].

1.3. Winter SST variability in the KOE region

The interannual to decadal SST variability in the North Pacific has been explained by the Pacific Decadal Oscillation [PDO, *Mantua and Hare*, 2002] and the Victoria mode [*Bond et al.*, 2003]; see also *Di Lorenzo et al.* [2008] for the North Pacific Gyre Oscillation (NPGO) which is the sea surface height (SSH) expression of the Victoria mode. *Yeh et al.* [2011] showed that a negative to positive PDO change, which is related to a strengthening of the Aleutian low (AL) and a warming of the tropical SST, is responsible for the winter North Pacific SST variability in the 1976/77 regime shift. Also, the NPGO-like mode, which is the oceanic expression of the North Pacific Oscillation [NPO, *Linkin and Nigam*, 2008] and West Pacific teleconnection pattern [WP, *Wallace and Gutzler*, 1981; *Linkin and Nigam*, 2008], is shown to explain most of the SST variability in the 1988/89

regime shift. Another SST regime shift in the winter of 1998/1999 from a positive to a negative PDO change was reported by *Jo et al.* [2013].

An attempt was made by *An* [2008] to understand the chain of these long-term SST variability and regime shifts with a multi-decadal oscillation mechanism associated with SST-zonal wind coupling and slow dynamic adjustment of the ocean. However, this multi-decadal oscillation mechanism explains only long-term and basin-scale SST variability, but not so well interannual to decadal SST variations in the KOE region where oceanic variability and the ocean-atmosphere interaction are much stronger compared to the rest of the North Pacific. For example, unlike a direct atmospheric influence on the SST in the central and eastern North Pacific [*Cayan*, 1992], the SST variability in the KOE region reveals a lagged response by a few years to changes in atmospheric forcing, related to the PDO [*Qiu*, 2003] or WP/NPGO [*Sugimoto and Hanawa*, 2009; *Ceballos et al.*, 2009] in the central North Pacific via westward propagating Rossby waves [*Miller et al.*, 2004]. These results emphasize an important contribution of ocean dynamics to the KOE region thermal variability, although the degree of relative contribution of ocean dynamics as compared to the atmospheric influence has been shown to vary with epoch [*Kelly and Dong*, 2004; *Park et al.*, 2012].

1.4. Oceanic contributions responsible for SST variability in the KOE region

Attempts have been made to understand KOE SST variations on a variety of time scales. Seasonal SST changes are dominated by the net surface heat flux and entrainment from below the surface mixed layer [*Qiu and Kelly*, 1993; *Alexander et al.*, 2000; *Vivier et al.*, 2002]. On interannual to decadal timescales the KOE SST variability is associated with the latitudinal frontal shift [*Seager et al.*, 2001; *Nonaka et al.*, 2006] and changes in geostrophic advection [*Vivier et al.*, 2002; *Taguchi et al.*, 2007; *Kwon and Deser*, 2007; *Nonaka et al.*, 2008] induced by the arrival of westward propagating baroclinic Rossby waves generated by wind stress curl forcing [*Deser et al.*, 1999; *Schneider and Miller*, 2001; *Seager et al.*, 2001; *Qiu*, 2003; *Qiu and Chen*, 2005; *Ceballos et al.*, 2009; *Sugimoto and Hanawa*,

2009]. *Sugimoto and Hanawa* [2011] showed, based on satellite observations, a great influence of meso scale anticyclonic eddies detached from the KE on the KOE SST variability, although such a feature may represent the intrinsic frontal-scale dynamics superimposed on the broad-scale meridional structure generated by basin-wide wind forcing [*Taguchi et al.*, 2007]. *Sugimoto and Hanawa* [2011] claimed that westward propagating Rossby wave signals and frontal displacement effects become greatly obscured by powerful eddy activity in the eddy-populated western boundary area west of 150°E. This is in line with the failure of the linear Rossby wave model hindcast in the westernmost KOE region by *Qiu* [2003], as previously remarked by *Park et al.* [2012].

Based on an extensive statistical analysis of observed SST and atmospheric variables in the western North Pacific, *Park et al.* [2012] evidenced an epoch-dependency of the dominant contributors to the KOE SST variability averaged over the area (142°–160°E, 35°–40°N). They found that, before 1990, the KOE SST variability was well correlated with the wind stress curl in the central/eastern basin of North Pacific at lags of 1, 3, and 4 yr, with the 3–4 year lags being suggestive of an influence of baroclinic Rossby wave propagation, consistent with previous works [*Deser et al.*, 1999; *Schneider and Miller*, 2001; *Seager et al.*, 2001; *Nonaka et al.*, 2008]. After 1990, however, only the 1-yr lag correlation between the KOE SST and the central North Pacific wind stress curl was significant. The reason for this change in lags is still unclear. *Park et al.* [2012] regarded the 1-yr lagged signal of wind stress curl, which is always evident lagged signal before and after 1990, as the contribution of the ocean dynamics to the KOE SST. The multi-variable linear regression with this lagged wind stress curl and winter monsoon indices to the SST suggests the change of the main contributor to determine SST variability, from both ocean dynamics and atmospheric forcing for 1970-1989 to a predominantly ocean dynamics for 1990-2005. Consequently, this result suggests that the ocean dynamics has played a central role for driving the long-term SST variability in the western North Pacific after the abrupt decline of the East Asian winter monsoon (EAWM) around 1990.

1.5. Atmospheric influences to the themal variability in the western North Pacific

The wintertime surface climate over the western North Pacific is under strong influence of the EAWM, whose intensity is predominantly determined by that of the Siberian high (SH) [*Gong et al.*, 2001; *Park et al.*, 2012]. As the prominent flow feature along the eastern flank of the anticyclonic SH, the EAWM is characterized by prevailing northerlies blowing over eastern China, Korea, Japan, and the surrounding marginal seas [*Park et al.*, 2012]. The SH experienced a pronounced decadal weakening in the late 1980s [*Nakamura et al.*, 2002; *Panagiotopoulos et al.*, 2005], which resulted in changes in the relative importance between the EAWM and ocean dynamics in driving the regional SST variability [*Park et al.*, 2012].

In addition to the EAWM, the NPO, a surface expression of the WP [*Wallace and Gutzler*, 1981], is also known to influence the winter oceanic temperature variability in the western North Pacific. For example, *Yeh and Kim* [2010] claimed that the long-term winter SST variability in the Yellow/East China Sea is best attributable to the NPO. *Park et al.* [2012] showed that winter SST anomalies averaged over the East Asian marginal seas are much better correlated with the EAWM than with the WP although these indices are significantly correlated to each other.

Not only the local atmospheric forcing, which takes only a month to influence to the SST, related to the EAWM/SH and NPO/WP as mentioned above, but also the remote forcing, which needs several years' time lag to affect KOE SST, related to the Pacific-North America (PNA) and WP, are known to influence the thermal variability in the western North Pacific. As discussed in section 1.4, the Rossby waves carry the oceanic thermal anomaly induced by wind stress curl anomaly in the central and eastern North Pacific. *Qiu* [2003] showed that the westward propagation of positive (negative) SSH anomalies in the KOE are caused by negative (positive) wind stress curl anomalies in the east associated with variability in the PDO, which is highly related to the PNA and the AL. In contrast to this, *Ceballos et al.* [2009] showed that the NPGO-related wind forcing, also well correlated with WP and related to the meridional shift of the AL system, is rather

responsible for this mechanism using both the statistical (lagged correlation) and dynamical method (simple linear Rossby wave model).

1.6. Purpose of the study

Despite a great number of previous studies, present knowledge about the dynamics and causes of the interannual to decadal upper-ocean thermal variability in the KOE region remains limited and often debated as will be seen later. Especially, it is not reported yet the reason of the sudden change of the relationship between EAWM and SST in the western North Pacific [*Park et al.*, 2012]. *Pak et al.* [2014] presented that the influence of atmospheric forcing is dominant before the sudden weakening of SH and EAWM (~1990), but its impact is significantly decreased, indicating that ocean dynamics may play an important role in deriving the SST variability in this region, after near-1990, consistent with *Park et al.* [2012]. In addition, the relationship is not clear between the EAWM and NPO which constitute two outstanding surface atmospheric circulation patterns affecting the winter SST variability in the western North Pacific, except their marginal correlation [*Park et al.*, 2012]. Therefore, the thesis reveals relative importance of atmospheric forcing (surface heat flux) and ocean dynamics (heat advection) on upper ocean thermal variability for different epochs, as well as interrelationship among the atmospheric forcing patterns (i.e., EAWM and NPO) influencing winter SST in the western North Pacific.

To investigate underlying dynamics of changes of the relationship between atmosphere/ocean dynamics and upper ocean thermal variability, heat budget analysis is also conducted in this thesis. However, the subsurface observational data record is too short to investigate the upper ocean heat budget at long time scales. So, both the SST products and 35-year long simulation from a high-resolution ocean general circulation model (OGCM) are used to represent long-term oceanic states. Comparing with atmospheric circulation, it is investigated that the upper-ocean heat budget in the climatically important KOE region focuses on the regime-dependent thermal variability and its major causes, especially in the winter season when the ocean-atmosphere interaction is strongest.

The thesis is organized as followings. In Chapter 2, description of the data including the high resolution OGCM, reanalysis product, and observational data sets used in the thesis together with their validation are given. In Chapter 3, the regime-dependent changes in atmospheric circulation patterns and their influences to oceanic thermal variability focused on the nonstationary relationship between EAWM and NPO before and after 1988 are given. In Chapter 4, an upper-ocean heat budget analysis for two contrasting climate regimes that occurred before and after 1991 in the western North Pacific, with an emphasis on the wintertime thermal variability and negative feedback of ocean temperature in the KOE region is shown. The major causes of the interannual to decadal scale variability of upper-ocean heat content in the KOE region are discussed also in Chapter 4, followed by a summary in Chapter 5.

Chapter 2. Data and method

The following two sub-sections (2.1 and 2.2) describe observational data, reanalysis product, and climate indices, used in the thesis to investigate the regime-dependent nonstationary relationship between the winter atmospheric circulation and the SST as a representative indicator of the ocean upper-layer thermal state. The next sub-section (2.3) describes OGCM data for heat budgeting in the study area to investigate the causes of thermal variability of the upper ocean. Also, analysis methods and periods are introduced in the last sub-section (2.4).

2.1. Observational and reanalysis data sets

Two principal datasets are used to investigate the relationship between the atmospheric circulation and oceanic upper-layer thermal state, which are the Hadley Centre Sea Ice and Sea Surface Temperature dataset (HadISST; available online at http://www.metoffice.gov.uk/hadobs/hadisst/) [*Rayner et al.*, 2003] and the so-called Trenberth sea level pressure (SLP) data [*Trenberth and Paolino*, 1980]. The SLP of 20th Century reanalysis V2 [*Compo et al.*, 2011] (20C reanalysis, hereafter) is also used to evaluate Trenberth SLP. In addition, the daily fields of geopotential height at 300 hPa (Z300) and 500 hPa (Z500) from the National Centers for Environmental Prediction/National Center for Atmospheric Research (NCEP/NCAR) Reanalysis 1 [*Kalnay et al.*, 1996] (NCEP, hereafter) are used to investigate upper-level blocking events and storm track activity. Other supplementary data used here are monthly averaged atmospheric SLP from the NCEP. Surface net heat fluxes from NCEP and OAFlux [*Yu et al.*, 2008] are also used to validate the net heat flux in the ocean model which will be described in section 2.3.

2.2. Climate indices

2.2.1 Definition and acquisition of climate indices

The SH index is defined as the area-mean SLP anomalies over the SH center (85°–105°E, 45°–55°N) and the EAWM index as the difference between the SH index and area-mean SLP anomalies in the southeastern Japan/East Sea (JES, 135°–140°E, 35°–40°N) following *Park et al.* [2012]. The NPO index is defined as the difference of SLP anomalies between two centers of action (170°E, 65°N and 165°E, 25°N) following *Wallace and Gutzler* [1981]. The NPO is positive when the SLP in the southern center is higher. Note that this NPO index has no significant difference (r = 0.82) from that suggested by *Linkin and Nigam* [2008] (NPO_L), which used the second principal component (PC) of SLP anomalies in the North Pacific (north of 20°N). Both the NPO and NPO_L indices are compared to each other in the following section. The Aleutian low (AL) index is used as a synonym of the North Pacific index defined as the area-mean SLP anomalies over the area (160°E–140°W, 30°–65°N) following *Trenberth and Hurrell* [1994]. To represent the intensity of the low pressure system with the AL index, sign of the AL index was reversed (positive AL index indicates strong AL intensity). The WP index, Arctic Oscillation (AO) index, and PNA teleconnection pattern index are taken from the NOAA Climate Prediction Center website (http://cpc.ncep.noaa.gov/data/teledoc/telecontents.shtml). The El Nino-Southern Oscillation (ENSO) index is defined as the multivariate ENSO index (MEI) from the NOAA/Earth System Research Laboratory website (http://www.esrl.noaa.gov/psd/enso/mei/). Moreover, PDO and NPGO indices are obtained from the websites http://research.jisao.washington.edu/pdo/ and http://www.o3d.org/npgo/, respectively, to investigate the relationship between atmospheric forcing patterns and major oceanic variability patterns. Cross-correlations among those winter atmospheric circulation pattern indices during different periods are presented in Table 2.1.

Table 2.1. Correlation coefficients between pairs of climate indices for 1965-2012, with significant correlations at the 95% confidence level being marked in boldface. Shown in 1st, 2nd and 3rd rows in the cell are correlation coefficients for three epochs: ALL (1965-2012), SM-HC (1973-1987) and WM-LC (1988-2002), respectively.

Indices	EAWM	NPO	WP	AO	ENSO	PNA	AL
SH	**0.91** **0.93** **0.77**	**−0.40** **−0.81** 0.18	**−0.45** **−0.85** 0.09	−0.16 −0.10 0.02	**−0.28** −0.42 −0.14	0.19 0.52 0.13	0.10 0.35 −0.13
EAWM		**−0.53** **−0.89** −0.11	**−0.57** **−0.92** −0.15	−0.29 −0.09 −0.13	**−0.32** −0.53 −0.18	0.14 0.44 0.02	0.12 0.33 −0.09
NPO			**0.80** **0.92** **0.61**	0.14 0.04 0.00	**0.53** **0.76** 0.14	0.12 −0.14 0.33	0.13 −0.01 0.28
WP				0.10 0.08 −0.14	**0.45** **0.68** 0.14	−0.04 −0.26 0.31	−0.12 −0.22 0.04
AO					−0.18 −0.00 −0.33	−0.24 −0.24 −0.59	**−0.38** −0.34 **−0.63**
ENSO						**0.44** 0.36 0.60	**0.51** 0.37 **0.72**
PNA							**0.92** **0.93** **0.86**

2.2.2 Justification of EAWM and NPO indices

a. EAWM index

Wang and Chen [2010] classified 18 existing indices into four categories according to the definition of the monsoon strength using different parameters, such as the east–west SLP gradient, low-level meridional winds, upper-level zonal wind shear, and East Asian trough for the 1957–2001 period. These authors assessed the spatial performance of these indices for representing the monsoon-related circulation, precipitation, and lower tropospheric air temperature anomalies

as well as their predictability based on knowledge of ENSO and AO. It is remarked that most of indices based on low-level meridional winds have been defined for the regions composing the tropics and subtropics (10°–30°N) over East Asia and the western North Pacific (110°–140°E), showing a high correlation (order 0.65) with the ENSO index [see Table 1 of *Wang and Chen*, 2010]. On the other hand, the SLP gradient-based indices have been defined mostly for the regions centered at midlatitudes (20°–60°N) using the SLP difference between the eastern lobe of the SH system (110°E) and the western lobe of the AL system (160°E). These latter indices show a moderate correlation (order 0.4) with the ENSO index. More recent work by *Wang and Chen* [2014b] suggests that, in addition to the east–west pressure gradient, the north–south pressure gradient between midlatitudes and equatorial region is also important for the winter monsoon. Correspondingly, an index was defined to well reflect these features.

Because main focus of the thesis is on the regime-dependent nonstationary relationship of the EAWM and NPO as well as their connection to the tropical influence (Chapter 3), the optimal EAWM index should be the one that shows in climatology the weakest relationship with ENSO but at the same time the strongest correlation with surface climate variables over the midlatitude western boundary region, where the winter monsoon northerlies prevail. In this sense, *Park et al.* [2012] compared several frequently cited winter monsoon indices with observations based products of surface variables (air temperature, SST, and wind speeds) in the midlatitude East Asian marginal seas. They concluded that their new EAWM index (defined as the normalized DJF SLP difference between the area-mean SLP over the Siberian center and that near the JES center) shows the best performance in explaining the variability of winter surface variables of the region from selected station data. Thus, the index is used here, $EAWM_{Park}$, reveals the practically same performance as the SH index, an indisputable index for gauging the winter monsoon strength over East Asia [*Gong et al.*, 2001], indicating the weakest relationship with (thus most independent from) ENSO and AO (see Table 2.1). Figure 2.1 shows how the $EAWM_{Park}$ correlates well (r = 0.83) with a recent EAWM index proposed by *Takaya and Nakamura* [2013], $EAWM_{Takaya}$, which is defined as normalized winter surface air temperature anomalies averaged over the midlatitude East Asian marginal seas (25°–40°N, 100°–140°E). However, these

surface air temperature anomalies show only a marginal correlation (r = 0.35) with 850-hPa meridional wind anomalies over the region, corresponding to the index proposed by *Yang et al.* [2002] ($EAWM_{Yang}$). Other EAWM indices defined in regions composing the tropics are not considered because of their inevitable ‘‘contamination’’ by strong ENSO signals (see section 3.2.3).

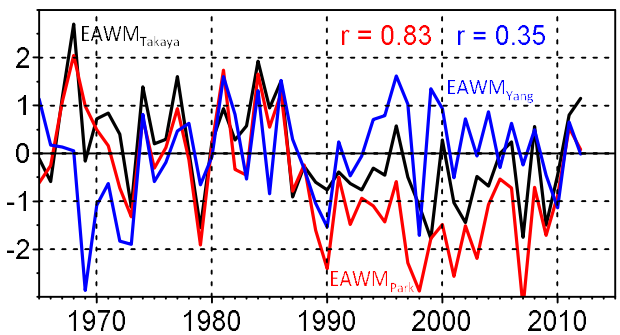

Figure 2.1. Comparison of $EAWM_{Park}$ (red) and $EAWM_{Yang}$ (blue) in reference to $EAWM_{Takaya}$ (black), with corresponding correlation coefficients given ($EAWM_{Park}$:$EAWM_{Takaya}$ = 0.83; $EAWM_{Yang}$:$EAWM_{Takaya}$ = 0.35).

Using 20C reanalysis, similar EAWM index is reproduced with same definition of $EAWM_{Park}$ (Figure 2.2). The correlation coefficient between EAWM indices obtained from Trenberth SLP and 20C reanalysis SLP is 0.82. However, the EAWM index from 20C reanalysis does not show significant depression after 1990 as in Trenberth SLP, although the interannual variation is similar to that from Trenberth SLP. *Jeong et al.* [2011] reported that various SLP data sets show weakening of SH, which influences the intensity of the EAWM, during 1990s and Trenberth SLP shows the strongest depression. Indeed, in Figure 2.2, 20C reanalysis also shows a slight weakening of EAWM after 1990 although its magnitude is not evident as in Trenberth SLP. So, it can be said that the EAWM index obtained from Trenberth SLP may represent the interannual to decadal variability of EAWM.

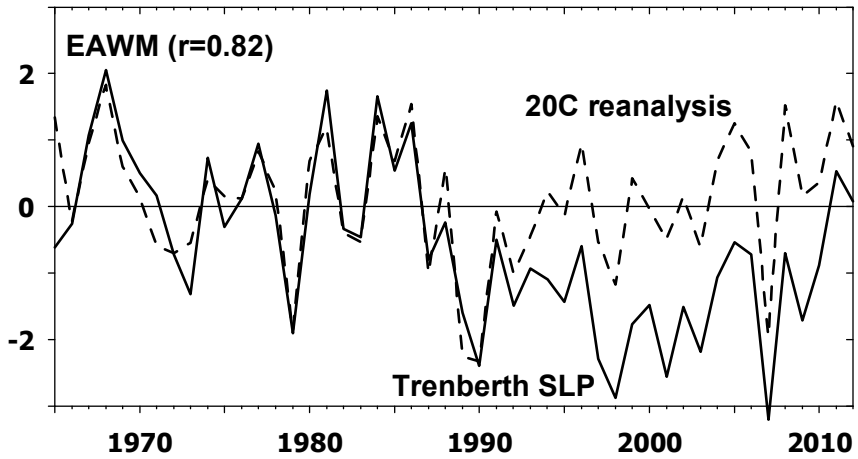

Figure 2.2. Comparison of EAWM indices obtained from Trenberth SLP (solid line) and 20C reanalysis (dotted line).

b. NPO index

As mentioned in section 2.2.1, the NPO index can be defined by two methods. *Wallace and Gutzler* [1981] used the difference of SLP anomalies between two centers of action (170°E, 65°N and 165°E, 25°N). In the thesis, the NPO index is defined using the SLP data (Trenberth SLP) with *Wallace and Gutlzer*'s [1981] method. On the other hand, *Linkin and Nigam* [2008] used the PC2 of the SLP anomalies over the monthly fields of winter in the North Pacific north of 20°N. Note that they took December to March as their winter and they considered each of the monthly field in the EOF analysis. This means that 4 spatial fields are contained for each year. In the thesis, the NPO_L index is defined using almost same method of *Linkin and Nigam* [2008] but DJF fields for consistency with the definition of winter in the thesis (three fields for each year). Then the yearly NPO_L index is obtained by taking annual averages for December-February value for each year.

Figure 2.3 shows the normalized winter (DJF) NPO indices defined by two methods. Both indices show evident and similar interannual variability which is discussed later (Chapter 3). The correlation coefficient between NPO index and NPO_L index during 1965–2012 is 0.82 which is high enough to be significant at 99% confidence level, indicating no sensitivity of the selection of the definion. In the

thesis, the NPO index using *Wallace and Gutzler*'s [1981] method is adopted for convenience. Note that the correlation between the NPO indices obtained from Trenberth SLP and 20C reanalysis is 0.98 (Figure 2.4), indicating both indices are almost identical.

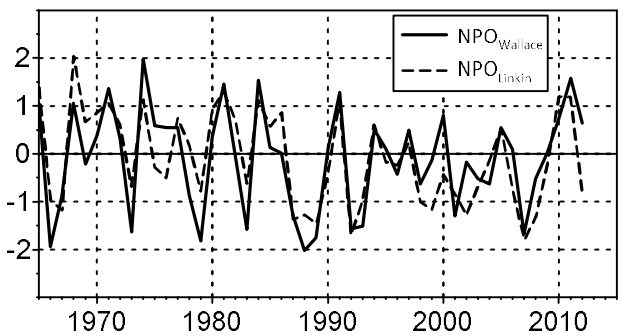

Figure 2.3. Comparison of NPO index following *Wallace and Gutzler* [1981] ($NPO_{Wallace}$, solid line) and following *Linkin and Nigam* [2008] (NPO_{Linkin}, dashed line). The correlation coefficient between two indices is 0.82.

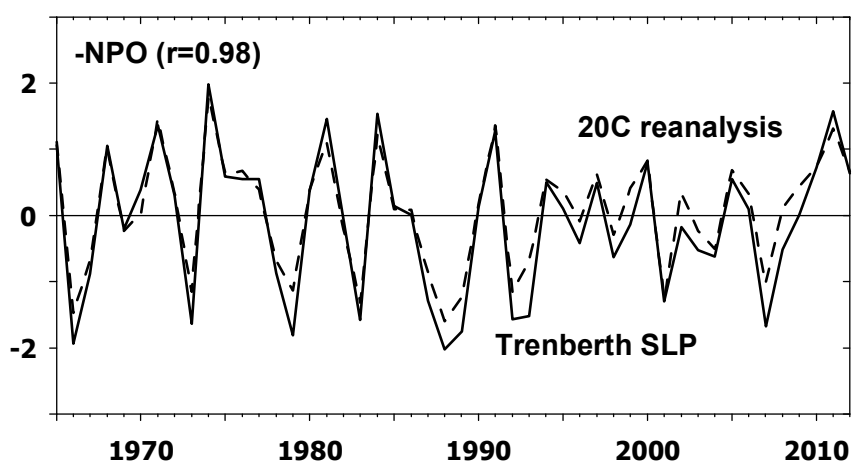

Figure 2.4. Comparison of NPO indices obtained from Trenberth SLP (solid line) and 20C reanalysis (dotted line).

2.3. Ocean General Circulation Model (OGCM) data

2.3.1 Model description

A 35-year (1979–2013) simulation with a high resolution global OGCM is used to investigate interannual to decadal thermal variability in the KOE region. The model (referred to as ORCA12 hereafter) is based on the NEMO 3.5 [*Madec*, 2008] which is a framework of ocean related engines including ocean dynamics/thermodynamics and sea-ice parts. The model solves the ocean primitive equations on C-grid system with hydrostatic and Boussinesq approximations. The OGCM has a 1/12° horizontal resolution operating on a tripolar ORCA grid type [*Madec et al.*, 1996; *Penduff et al.*, 2010]. The ORCA12 grid delivers a horizontal resolution of 9.25 km at the equator, 7 km in mid-latitude region, and 1.8 km in the Ross and Weddell Seas. The grid has 4,322 x 3,059 points in X and Y directions, respectively. The vertical grid has 75 z-level coordinate with a grid space ranging from 1 m near the surface to 250 m at 5,750 m. The topography is expressed with bottom partial cells [*Adcroft et al.*, 1997; *Barnier et al.*, 2006] using a combination of three databases: 1) ETOPO1 [*Amante et al.*, 2009], 2) GEBCO08 [*Becker et al.*, 2009] merged for continental shelves shallower than 200 m, and 3) Base 10 (personal communication with *Dr. F. Lyard* (lyard@legos.obs-mip.fr) around the European coasts.

The total variance dissipation (TVD) formulation scheme, widely known as flux corrected transport scheme [*Boris and Book*, 1973], with anti-diffusive flux term is employed for the tracer advection. An energy and enstrophy conserving scheme [*Arakawa and Lamb*, 1981] is adopted for the momentum advection. To represent the exchange of the horizontal momentum and tracer due to the sub-grid scale processes, an isolevel-biLaplacian and a Laplacian-isopycnal diffusion schemes are employed, respectively. The K-epsilon scheme parameterizes the vertical mixing coefficients. A partial-slip condition is applied for lateral boundary condition.

All the surface heat and momentum fluxes are calculated by bulk formulation [*Large and Yeager*, 2004], using model-generated SST and meteorological variables such as wind vector, atmospheric temperature, relative humidity, and

radiative/freshwater fluxes from ERA interim [*Dee et al.*, 2011]. The time interval of flux data is one day allowing diurnal cycle to the shortwave radiation, while the other atmospheric variables are subsampled at every 3 hours. The heat, freshwater, and momentum fluxes are modified in the presence of sea ice which is modeled by LIM2 sea ice model [*Bouillon et al.*, 2009]. The monthly run-off climatology is built with data from *Dai and Trenberth* [2002].

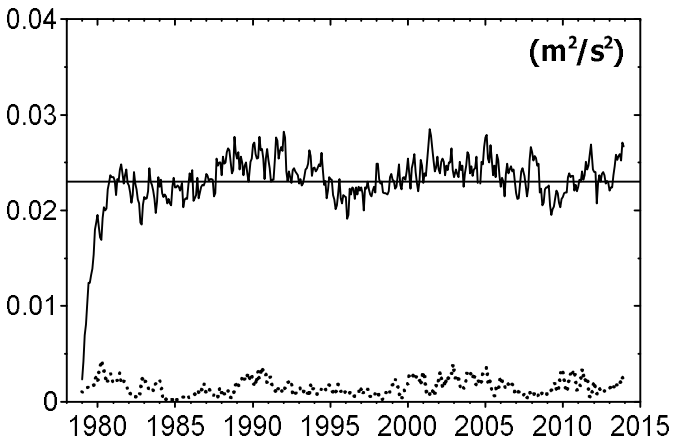

Figure 2.5. Temporal evolution of volume-averaged kinetic energy (unit is $m^2\ s^{-2}$) over the upper 400 m in the western North Pacific (140°–180°E, 28°–46°N, solid line) obtained from monthly averaged horizontal velocities. Kinetic energy obtained from volume-averaged velocity over the upper 400 m in the KOE region (150°–165°E, 36°–42°N, dotted) is also overlaid and a solid line indicating constant value of 0.023 $m^2\ s^{-2}$ is superimposed.

Model run is performed from cold start with initial hydrographic data from January climatology [*Levitus et al.*, 2005]. Temporal evolution of kinetic energy averaged over the upper 400 m in the western North Pacific region (140°–180°E, 28°–46°N) indicates that at least the upper 400 m of the model ocean has reached equilibrium since the end of 1980, with the area-mean energy fluctuating around a constant value of 0.023 $m^2\ s^{-2}$ (Figure 2.5). In addition, the kinetic energy obtained from volume-averaged velocity is also just fluctuate and does not have any

monotonic linear trend (dotted line in Figure 2.5). Hence, the first 2-year integration is considered as a spin-up period and 3-day averaged outputs are analyzed for the last 33 years (1981–2013).

Although the model was integrated globally, the domain of analysis is mostly limited in the western North Pacific (140°–180°E, 28°–46°N). To obtain a representative area-averaged time series, the KOE region is selected as the region (150°–165°E, 36°–42°N) corresponding to the primary center of the upper-ocean thermal variability, as will be shown later in Chapter 4. The KOE region of the thesis corresponds to regions of interest in previous studies using observational data such as *Tanimoto et al.* [2003] (140°–165°E, 35°–45°N) and *Park et al.* [2012] (142°–160°E, 35°–40°N). The region west of 150°E was excluded due to the prevalence of mesoscale activity which obscures large-scale upper-ocean thermal variability caused by basin-scale atmospheric forcing [*Sugimoto and Hanawa*, 2011]. The KOE region lies approximately between the KE (along 36°N in ORCA12) and the Oyashio Extension (OE, along 41°N in ORCA12), and corresponds to the mixed water region according to *Qiu* [2001]. The results of subsequent analyses are not so sensitive to the selection of the KOE region within a few degrees in longitudes or latitudes. The model has ocean-only component without any data assimilation and coupling with atmospheric models, and it provides dynamically-consistent, long and continuous three-dimensional physical fields.

2.3.2 Model validation

a. Data sets for validation

The ORCA12 SSH and SST are compared with the daily 1/4° gridded absolute dynamic topography (ADT) product distributed by Archiving, Validation, and Interpretation of Satellite Oceanographic data (AVISO, http://www.aviso.altimetry.fr./duacs/) and the version 2 of the optimally interpolated 1/4° daily AVHRR (Advanced Very High Resolution Radiometer) SST [OISST, *Reynolds et al.*, 2002]. The ORCA12 MLT is often considered as its SST,

because both MLT and SST are frequently used interchangeably [*Grodsky et al.*, 2008]. Indeed, the temporal variability of MLT is nearly the same as that of the model's temperature at the first z-level in the KOE region (Figure 2.6). Note that the temporal correlation coefficient for DJF time series during 1984-2013 between MLT and first z-level temperature is 0.9999 and RMS (root-mean-square) difference is only 0.045°C, where the mixed layer depth is defined as the depth where the temperature difference becomes 0.2°C with the temperature at 10 m.

The SSH and SST were compared for periods of 1993–2013 and 1982–2013, respectively, considering overlapping periods between ORCA12 and other datasets. Note that the comparison period for winter (DJF) interannual variability of SSH (Figure 2.8e) is set to 1994–2013 because the daily ADT in December 1992 is not provided. Similarly, the comparison period for winter SST is also limited to 1983–2013 (Figure 2.8f). Here, the winter SST (or SSH) of 1994 refers to the mean SST (or SSH) during December 1993–February 1994. The interannual standard deviation (shading in Figure 2.7) is calculated from annual mean SSH and SST fields of both ORCA12 and satellite datasets.

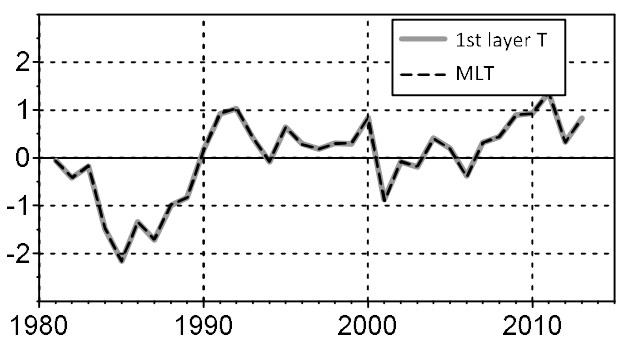

Figure 2.6. Comparison of the area-averaged winter MLT and temperature at first model-level in the KOE region.

b. Spatial distribution

The record-length (1993–2013) mean SSH field of ORCA12 (Figure 2.7a)

well reproduces the major features of KE seen in AVISO ADT (Figure 2.7b) such as two quasi-stationary meanders locating near 144°E and 150°E [*Qiu and Chen*, 2005]. Model-data discrepancies include model's overshooting of the Kuroshio by about 1° northward and stronger meander south of Japan (137°E, 32°N). The record-length (1982–2013) mean ORCA12 SST field (Figure 2.7c) shows a spatial distribution similar to that of OISST (Figure 2.7d). Note that the original ORCA12 variables have been averaged and resampled in a 0.25° by 0.25° grid, consistent with the horizontal grid spacing of AVISO ADT and OISST.

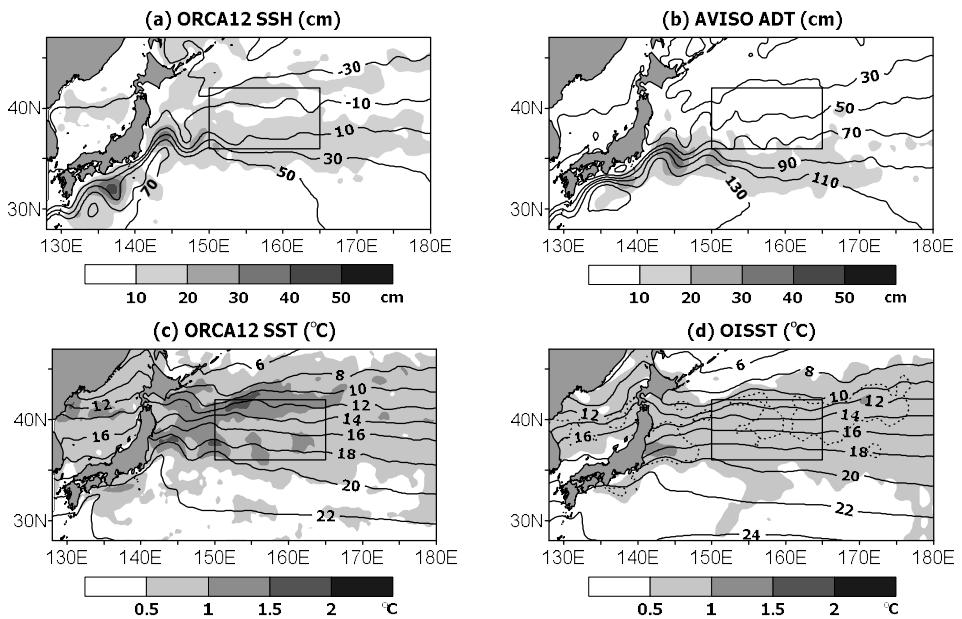

Figure 2.7. Climatological mean (1993-2013) SSH from (a) ORCA integration and (b) AVISO ADT. Contour interval is 20 cm. Climatological mean (1982-2013) SST from (c) ORCA integration and (d) OISST. Contour interval is 2°C. Standard deviations of annual averaged are marked as shading. Dotted lines in (d) indicate standard deviation of 0.75°C. The rectangular domain (150°-165°E, 36°-42°N) indicated in (a)~(d) is used for defining the KOE region.

The spatial distribution of interannual standard deviation (shading) is also well

reproduced by ORCA12 especially for SSH (Figures 2.7a and 2.7b). The interannual variability of SSH is strong along the KE, and particularly enhanced (>30 cm RMS) for the western quasi-stationary meander centered at (144°E, 35°N) in both ORCA12 SSH and AVISO ADT. The region south of Japan also shows relatively strong interannual variability for both ORCA12 SSH and AVISO ADT. The interannual variability south of Japan, however, is much stronger (>40 cm) in ORCA12 SSH than that of AVISO ADT (~25 cm). This is related to the vigorous spatial variability of the warm eddy-like features south of Japan in the ORCA12, while it is relatively stable in AVISO ADT. The ORCA12 SSH shows also stronger temporal variability compared to that of the AVISO ADT just north of 40°N where the OE is generally located [*Frankignoul et al.*, 2011].

c. Seasonal and interannual variations

To examine the temporal variability of ORCA12 SSH and SST in more detail, time series of spatially-averaged SSH and SST in the KOE region are shown in Figure 2.8. The seasonal cycle of ORCA12 SSH and SST has a good agreement with that of AVISO ADT and OISST (Figures 2.8a and 2.8b), both in terms of amplitude and phase, with a correlation coefficient exceeding 0.99. Note that a bias for the difference in the reference between ORCA12 SSH and AVISO ADT (-37.5 cm) is added to the seasonal variability of AVISO ADT to fit the range of ORCA12 SSH. The seasonal cycle of ORCA12 SST is almost the same as that of OISST except for a warm bias of 0.5 °C in ORCA12 SST during cold season (January-March). ORCA12 T400 (depth-averaged temperature from surface to 400 m) shows similar seasonal cycle with much smaller amplitude and a lag of one month compared to seasonal SST cycle, so that the T400 has a maximum and minimum on October (11.9°C) and April (10.0°C), respectively.

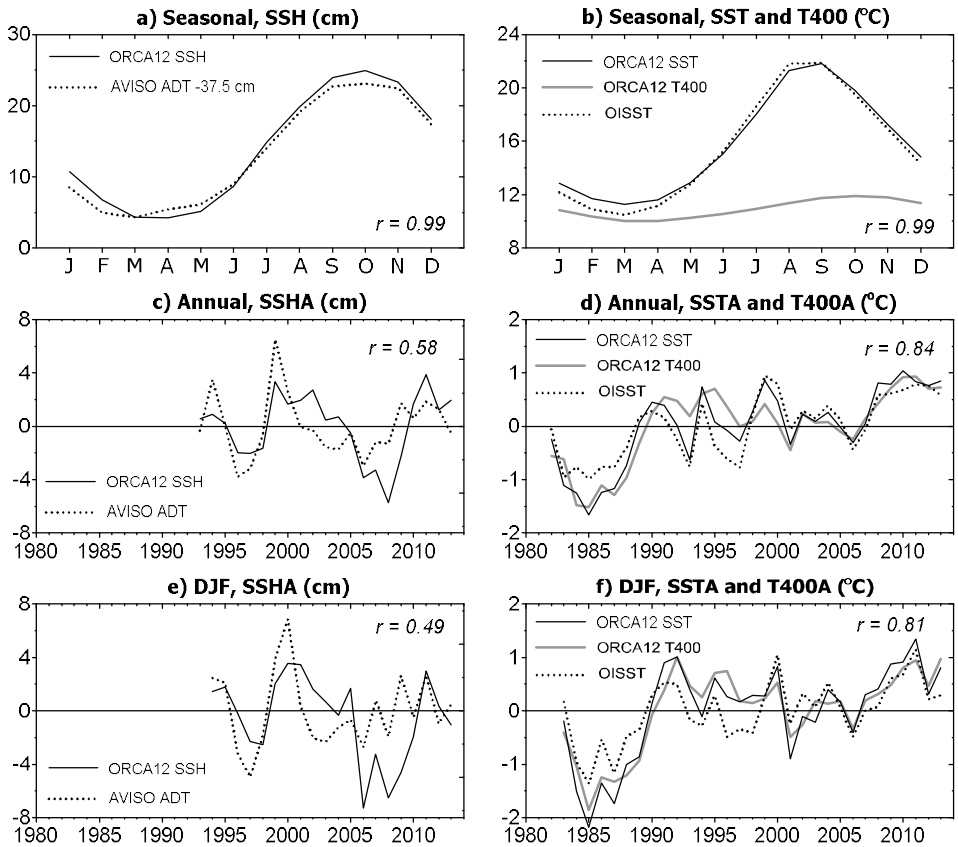

Figure 2.8. Time series of (a, c, e) SSH and (b, d, f) SST averaged over the KOE region shown in Figure 2.7, from ORCA simulation (solid lines) and observations (dotted lines) (AVISO ADT for SSH and OISST for SST). (a-b) Monthly climatologies, (c-d) annual mean anomalies, and (e-f) winter (December-February) mean anomalies.

The interannual variability shown in Figure 2.8c is based on the annually-averaged monthly anomalies that are obtained after removing the monthly climatology. It is noted that the ORCA12 SSH shows a decreasing trend (Figure 2.9), which is not observed in the AVISO ADT (Figure 2.8c), suggesting that the deeper layer of the model below 400 m is far from equilibrium during the analysis period (1981-2013) contrasting to the upper 400 m. In the subsequent analyses, this model drift is removed by detrending the original ORCA12 SSH time series. The linear trend during the analysis period (1981-2013) is removed. The detrended

ORCA12 SSH and AVISO ADT are moderately correlated with each other at 0.58 for annual means (Figure 2.8c) and at 0.49 for winter means (Figure 2.8e), although both are significant at the 99% confidence level, indicating that the interannual SSH variability is reasonably well reproduced in ORCA12. The results can be somewhat different if detrending of linear trend is applied only the period of decreasing SSH (1992-2005). However, this part is no longer covered because the comparison of SSH is not a main story of the thesis. The interannual variability of ORCA12 SST shows a far better agreement with OISST for both annual means (r = 0.84, Figure 2.8d) and winter means (r = 0.81, Figure 2.8f). These results indicate that one can confidently use the ORCA12 outputs for investigating the upper-ocean thermal variability in the western North Pacific. The variability of T400 also agrees well with that of SST for annual (r = 0.81, Figure 2.8d) and winter (r = 0.93, Figure 2.8f) average.

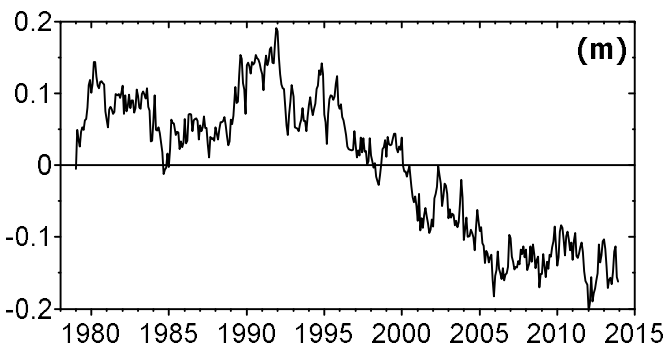

Figure 2.9. Time series of nonseasonal anomalies of monthly SSH averaged in KOE region (150°-165°E, 36°-42°N) without detrending.

2.4. Methods and periods of analyses

2.4.1 Linear correlation

Most of the subsequent analyses are based on the linear correlation coefficients, which are obtained after removing linear trend of each annual time

series. A 95% confidence level is generally used to determine the significance of the correlation coefficients presented in this thesis. The confidence limits of significant correlation are calculated from the two-tailed *t*-test with the effective degree of freedom. The effective degree of freedom is estimated by dividing the data length (N) by the integrated auto-covariance function [*Emery and Thompson*, 1997], unless otherwise stated. According to personal communication with *Dr. Laurent Terray* (terray@cerfacs.fr), the effective degree of freedom is valid when the number of time samples is large (>30 or so). However, the main results of subsequent analyses are robust when N-2 degree of freedom is used.

2.4.2 Linear regressions

The regression coefficients (R) between the single predictor (x) and target (y) are defined as:

$$R(x,y) = S(y) \times r(x,y), \qquad (2.1)$$

which is the product of the standard deviation of the target variable $S(y)$ and the correlation $r(x,y)$ between the predictor and target variables. Because the standard deviation of the predictor is not considered, the regression coefficients indicate that the changes of target variable when the predictor variable is changed by one standard deviation. Although this regression method is a bit different from the classical (and standard) method of the linear regression, this method can simultaneously measure the influence of multiple predictors with different units to the target variable.

2.4.3 F-test

The difference of two given standard deviation (or variance) is tested, whether the difference is significant or not, using F distribution with N-1 degree of freedom and 95% confidence level. The F value is estimated by the ratio of variances of two

samples (= s_1^2/s_2^2). If the F value is not bounded by upper and lower limits of F value with given confidence level and each degree of freedoms of two samples, the Null-hypothesis, which is the sample variances are same, can be neglected. That means the variances (or standard deviations) of two samples are significantly different. Readers who want to know detail processes of F-test can visit the following web site:
http://www.itl.nist.gov/div898/handbook/eda/section3/eda359.htm.

2.4.4 Regime shift detection

Rodionov [2004] suggested a sequential algorithm to determine different climate regimes in terms of the difference of mean value of a certain index during contrasting periods. In Chapter 3, climate regimes will be defined using the regime shift detection method of *Rodionov* [2004]. The algorithm having several sequential steps is described below.

Step 1. Set the cut-off length l of the regimes to be determined for variable X. The parameter l is similar to the cut-off point in low-pass filtering.

Step 2. Determine the difference *diff* between mean values of two subsequent regimes that would be statistically significant according to the Student's t-test:

$$diff = t\sqrt{2\sigma_l^2/l}$$

where t is the value of t-distribution with $2l$ - 2 degrees of freedom at the given probability level p. It is assumed that the variances for both regimes are the same and equal to the average variance σ_l^2 for running l-year intervals in the time series of variable X.

Step 3. Calculate the mean $\bar{x}_{R1}$ of the initial l values of variable X as an estimate for regime *R1* and the levels that should be reached in the subsequent l years to qualify for a shift to regime *R2*, $\bar{x}'_{R2} = \bar{x}_{R1} \pm diff$.

Step 4. For each new value starting with year $i = l + 1$ check whether it is greater than $\bar{x}_{R1} + diff$ or less than $\bar{x}_{R1} - diff$. If it does not exceed the

$\bar{x}_{R1} \pm diff$ range, then it is assumed that the current regime has not changed. In this case, recalculate the average $\bar{x}_{R1}$ to include the new value x_i and *l* - *1* previous values of variable *X* and wait for the next value to come. If the new value x_i exceeds the $\bar{x}_{R1} \pm diff$ range, then this year is considered as a possible start point *j* of the new regime *R2*.

Step 5. After the shift point is established, each new value of x_i, where $i > j$, is used to confirm or reject the null hypothesis of a regime shift at year *j*. If the anomaly $x_i - \bar{x}'_{R2}$ is of the same sign as the one at the time of a regime shift, it would increase the confidence that the shift did occur. The reverse is true if the anomalies have the opposite signs. This change in the confidence of a regime shift at $i = j$ is reflected in the value of the regime shift index (RSI), which represents a cumulative sum of the normalized anomalies:

$$\mathrm{RSI}_{i,j} = \sum_{i=j}^{j+m} \frac{x_i^*}{l\sigma_l}, m = 0,1,\cdots,l-1.$$

Here $x_i^* = x_i - \bar{x}'_{R2}$ if the shift is up, or $x_i^* = \bar{x}'_{R2} - x_i$ if the shift is down. If at any time from $i = j + 1$ to $i = j + l - 1$ the RSI value turns negative, proceed to step 6, otherwise proceed to step 7.

Step 6. The negative value of RSI means that the test for a regime shift at year *j* failed. Assign zero to RSI. Recalculate the average value $\bar{x}_{R1}$ to include the value of x_j and keep testing the values of x_i starting with $i = j + 1$ for their exceedence of the range $\bar{x}_{R1} + diff$ as in step 4.

Step 7. The positive value of RSI means that the regime shift at year *j* is significant at the probability level *p*. Calculate the actual mean value for the new regime $\bar{x}_{R2}$. At this point, it becomes the base one, against which the test will continue further. The search for the next shift to regime *R3* starts from year $i = j + 1$. This step back is necessary to make sure that the timing of the next regime shift is determined correctly even if the actual duration of regime *R2* was less than *l* years. The calculations continue in a loop from step 4 through step 7 until all the available data for variable *X* are processed. If there are several variables, the final RSI is the average of RSIs for each variable.

2.4.5 Analysis periods

Analysis periods depend on the available data sets. Based on observational and reanalysis products, winter of 1965-2012 is selected as a period of primary analyses. In the case that the data set does not cover this period, analysis period is adjusted. Particularly, the OGCM data has a period of 1981-2013 excluding spin-up time, so that the analysis period is set to the period from 1981 to 2013. The winter is generally defined as DJF (December to February). However, when the influence of atmosphere on ocean is considered, JFM (January to March) is also used to represent winter particularly for oceanic variable (SST). Note that in the heat budgeting (Chapter 4), the winter is fixed to DJF for both atmospheric (heat fluxes) and oceanic variables. Convention of the year is that containing January, i.e., winter of 2012 indicates averages from December 2011 to February 2012 (or January 2012 to March 2012), otherwise not stated.

Chapter 3. Near-1990 climatic regime shifts in the western North Pacific

In this chapter, it is investigated that the nonstationary relationship between the EAWM and NPO, two outstanding surface atmospheric circulation patterns affecting the winter SST variability in the western North Pacific as well as the change of their impacts on the SST with a sudden regime shift in late 1980s with observation-based data. Also, regime dependent changes of the atmospheric state and the mechanism for controlling the EAWM and NPO patterns are discussed. Because the winter atmospheric influence on the SST is most evident when the winter atmospheric circulation indices leads SST by a month, DJF (December-February) and JFM (January-March) averages are taken for atmospheric indices and SST, respectively. Most of contents in this chapter was published in a journal paper; see *Pak et al.* [2014].

3.1. Regime-dependent nonstationary relationships among atmospheric indices and ocean

3.1.1 Regime shifts of atmospheric circulation patterns and a change in relationship between EAWM and NPO

a. Major atmospheric patterns influencing upper ocean variability in the North Pacific and East Asia

As discussed in Introduction, the PDO and NPGO-like modes are dominant patterns of the upper ocean thermal variability patterns in the North Pacific. To investigate the atmospheric forcing patterns related to those major upper ocean variability modes, the regression coefficients of wind stress curl (WSC) to the major atmospheric indices are compared with those to the PDO and NPGO indices. Figures 3.1a and 3.1b show the regression map of SST on the PDO and NPGO indices, respectively. Note that the PDO and NPGO maps are averaged for January-March to represent oceanic variability. The PDO and NPGO modes show the well-

known horse-shoe and north-south dipole patterns, respectively. The WSC pattern related to the PDO (Figure 3.1c) shows dipole pattern, which is previously reported by *Ishi and Hanawa* [2005]. This dipole pattern of WSC is well observed from the PNA-regressed WSC (Figure 3.2a), suggesting that PNA and PDO are tightly correlated to each other. The dipole pattern of WSC is the 1st mode variability in the North Pacific [*Ishi and Hanawa*, 2005]. Moreover, the dipole pattern of WSC is observed from the ENSO-regression (Figure 3.2e). On the other hand, the NPGO-regression shows negative WSC centered in the mid-latitude regions (30°-40°N, Figure 3.1d), which is similar with the 2nd mode of WSC [*Ishi and Hanawa*, 2005]. This spatial pattern is very similar with the regression maps of WSC on the WP (Figure 3.2b), EAWM (Figure 3.2c), and NPO (Figure 3.2d).

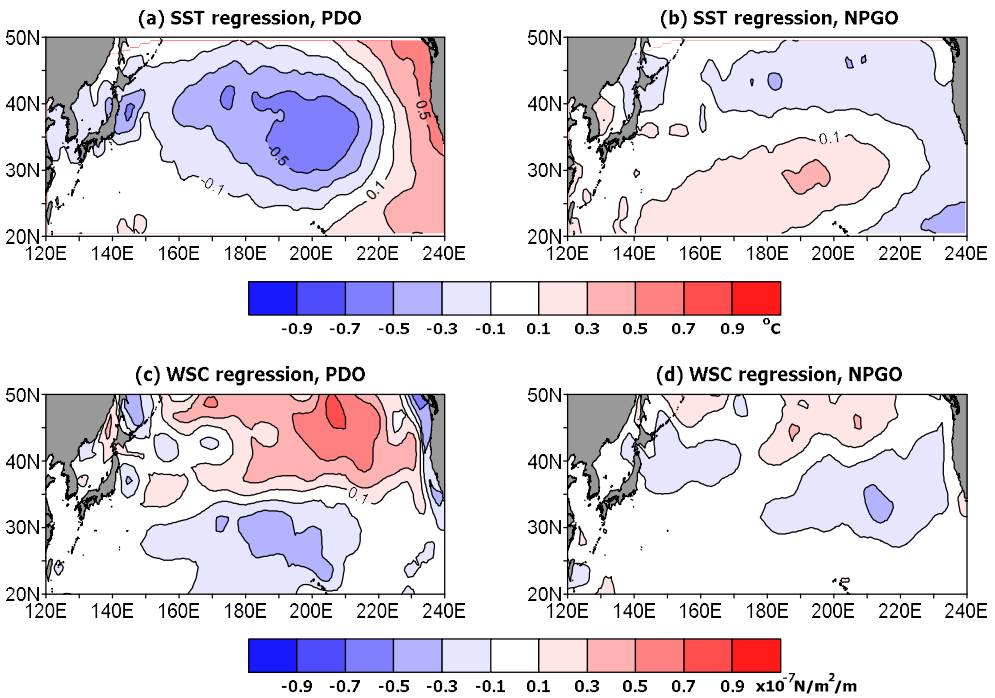

Figure 3.1. Spatial distribution of regression coefficients of (a-b) JFM SST to (a) JFM PDO index and (b) JFM NPGO index and of (c-d) DJF wind stress curl (WSC) to (c) JFM PDO index and (d) JFM NPGO index during 1965-2012.

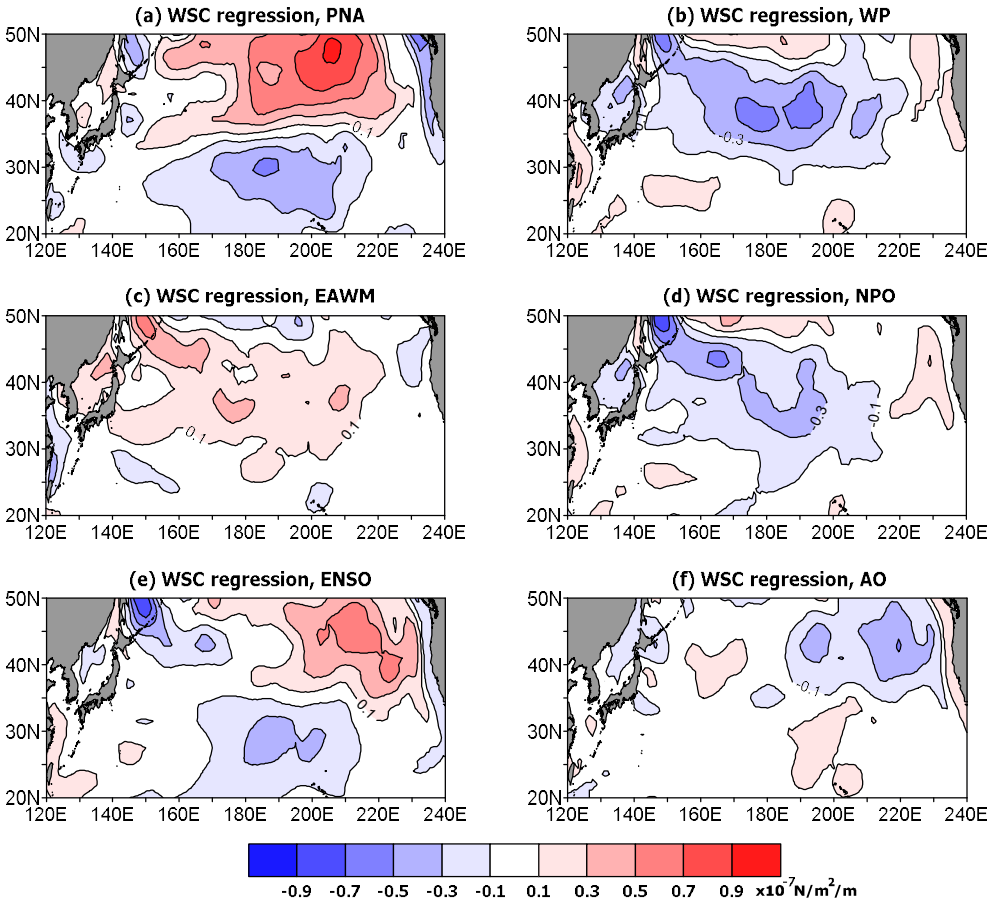

Figure 3.2. Spatial distribution of regression coefficients of DJF wind stress curl (WSC) to (a) PNA index, (b) WP index, (c) EAWM index, (d) NPO index, (e) ENSO index, and (f) AO index during 1965-2012.

b. Regime shifts of atmospheric circulation indices

Regime shifts are defined as rapid reorganizations of system from one relatively stable state to another [*Rodionov and Overland*, 2005]. Currently, a popular interpretation of long-term variability in the climate is based on the concept of regime shifts [*Rodionov*, 2006]. *Rodionov* [2004] suggested an automatic detection method for regime shifts based on sequential t-test analysis as introduced in section 2.4.4. After that, an advanced method additionally using prewhitening procedure to remove red noise components from time series is

developed [*Rodionov*, 2006]. To objectively determine the exact regime shifts that occurred during the past several decades in the North Pacific, it is applied the method of *Rodionov* [2004] using the code from NOAA Bering Sea climate website (http://www.beringclimate.noaa.gov/regimes/). Note that prewhitening procedure [*Rodionov*, 2006] is not considered for convenience. This method uses a sequential data processing technique so that it exhibits a limitation of the solution being less reliable if a regime shift is too close to the end of a time series, as commonly encountered by other regime shift detection methods. For the regime shift determination, the following parameters are used: cutoff length in year (l), probability level (p), and Huber weight (or outlier) in standard deviation (s). In the thesis, $l = 10$, $p = 0.15$, and $s = 1.5$ are selected. Although the regime shift detection is sometimes failed when the parameters changed, the timings (near 1977 and near 1988) are generally robust.

Figure 3.3 shows the results for normalized climate indices discussed here together with the corresponding cumulative sums. Note that the time series of cumulative sums is also normalized to fit the range of the normalized climate indices. The cumulative sum has been known to be very useful for a visual validation of regime shifts [*Tian et al.*, 2008], and it is observed in fact that all detected regime shifts coincide within ±1 yr with the extremes of the cumulative sum. A major regime shift in the four dominant climate indices of the western North Pacific (EAWM, NPO, SH, and WP) occurred between 1987 and 1989. For the sake of simplicity in the subsequent analyses, only the year 1988 is taken as the representative regime shift common to these four indices. The 1988 regime shift detected in Figure 3.3 is consistent with *Wang et al.* [2009]. Furthermore, there is an evidence of the latest regime shift around 2010 for all four indices, although it should be interpreted with caution because of the limited data length after 2010. Accordingly, it is defined two distinct winter climate regimes in the western North Pacific: a strong monsoon regime during 1965–87 and a weak monsoon regime during 1988–2010.

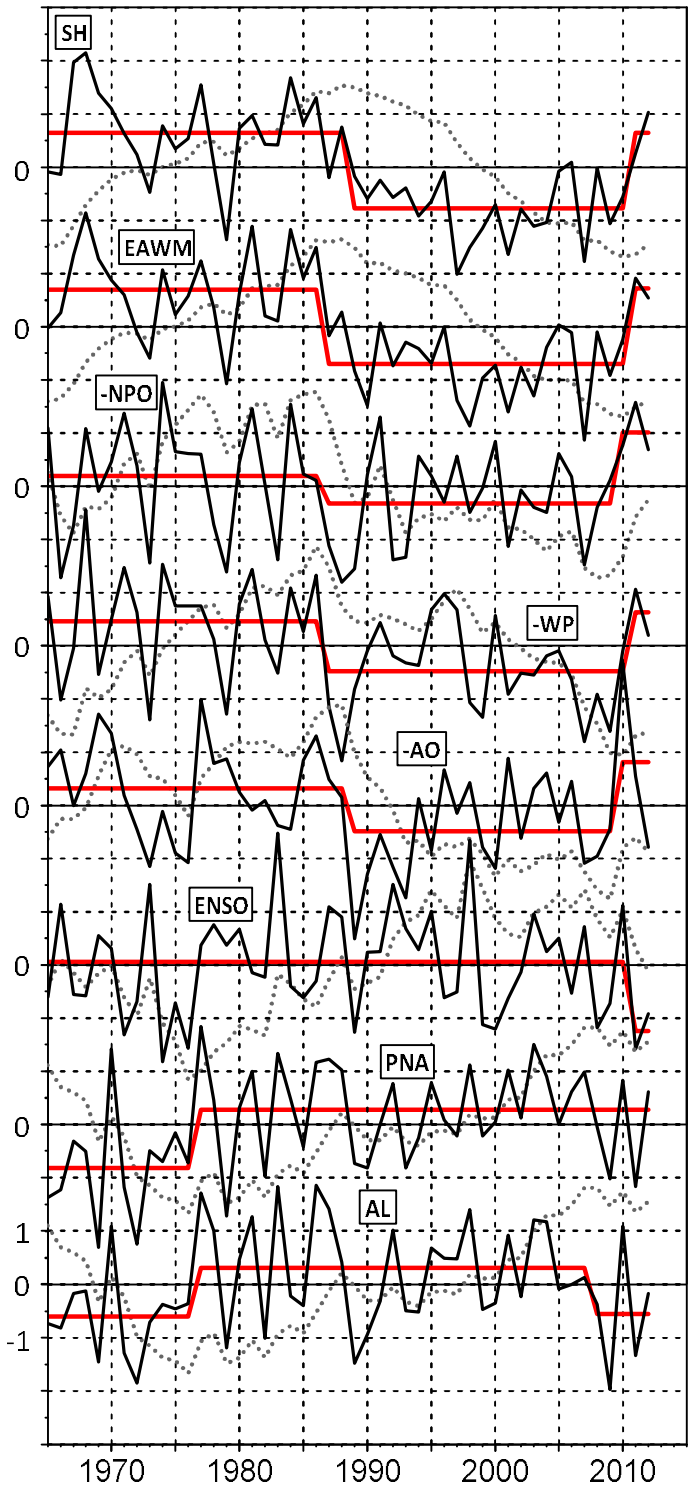

Figure 3.3. Climate regime shift determination (red) from normalized climate indices (black) based on Rodionov (2004), together with normalized cumulative sums (dotted gray).

Supplementary analysis with the dominant teleconnection patterns in the eastern North Pacific such as the AL and the PNA indices reveals the well-known 1976/77 regime shift (see Figure 3.3), consistent with *Hare and Mantua* [2000]. As mentioned in Introduction, the PDO mode experienced a sudden negative to positive shift around 1977. And the intensity of Aleutian low (AL) and the PNA index have significantly correlated with the PDO. Indeed, in the subsection 3.1.1a, it has been shown that the PNA and ENSO related wind stress curl in the North Pacific shows very similar spatial pattern with PDO related wind stress curl fields (Figures 3.1 and 3.2), although no regime shift is detected in the ENSO index with the data period and method. *Hare and Mantua* [2000] and *Yeh et al.* [2011] reported another major regime shift in 1988/89 in the North Pacific SST. It is noted here that the latter regime shift around 1988 is found in the major climate indices in the western North Pacific while that around 1977 is found in the eastern North Pacific. Although *Wang et al.* [2007] showed that the typical periodicity of the NPO changed from 3 yr before 1976 to 5–6 yr afterward, any clear evidence of its regime shift around 1976 was not found (see Figure 3.3). Note that the 1988 regime shift is also observed in the AO index. Finally, there is an evidence of the latest regime shift around 2010 for all indices but one (PNA).

c. Changes of relationships between atmospheric indices

The 11-yr running correlation coefficient between the EAWM and NPO indicates that the two indices were not always well correlated with each other (Figure 3.4), suggesting insignificant correlations particularly before the early 1970s, largely consistent with *Wang et al.* [2007], and in the 1990s. The EAWM–NPO correlation as well as the EAWM intensity recovered gradually since the early 2000s, the latter being also consistent with *Wang and Chen* [2014a]. Similar results are obtained with varying window size between 9 and 15 yr. It is remarkable that the transition from significant to insignificant correlations occurred very close to the 1988 regime shift. As the main focus here is the nonstationary relationship between the EAWM and NPO, two contrasting 15-yr-long epochs are selected before and after the 1988 regime shift, with a significant correlation versus an

insignificant one as the strong monsoon–high correlation (SM–HC) epoch (1973–87) and the weak monsoon–low correlation (WM–LC) epoch (1988–2002). If not explicitly stated otherwise, the regime-dependent comparison described hereafter in Chapter 3 should be understood as using the above two epochs, which will be clarified in the text. Indeed, during the SM–HC epoch, the EAWM index is practically indistinguishable from the NPO index (r = -0.89), while the two indices became nearly independent (r = -0.11) during the WM–LC epoch (Table 2.1). The SH–NPO pair shows similar results, albeit with somewhat weaker correlations compared to the EAWM–NPO pair. The WP is generally better correlated than NPO with both the EAWM and SH.

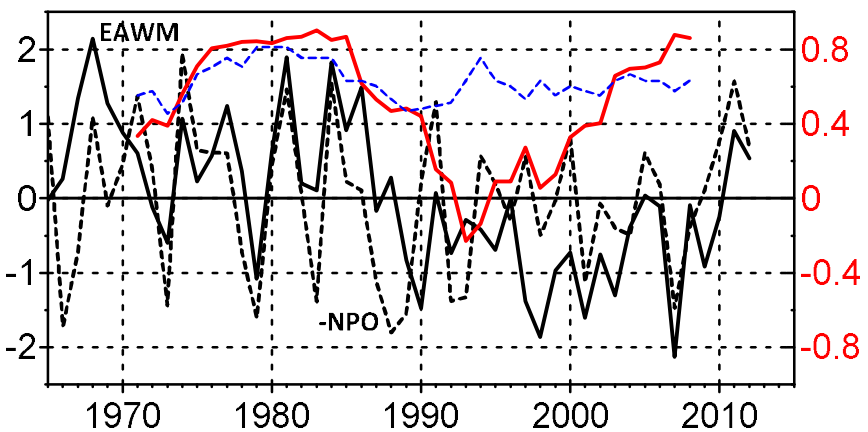

Figure 3.4. 11-yr running correlation coefficient (red) between the EAWM (solid black) and negative NPO (dotted black) indices. The dashed blue line indicates the 95% confidence level for the running correlation coefficients.

Similar analysis with longer period time span from 1900 using Trenberth SLP suggests that the changing of the relationship between EAWM and NPO is not a unique event around 1988. The EAWM–NPO correlation also decreased during late-60s to early-70s and increased after WM-LC period (Figure 3.5a). Note that the size of window in the moving correlation shown in Figure 3.5 is also 11 years and the result is nearly insensitive to the window size. Unfortunately, there are

several empty values of Trenberth SLP in the SH centers before 1960 so it is very difficult to estimate the moving correlation between EAWM and NPO. Same analysis with 20C reanalysis also shows that the moving correlation between EAWM and NPO shows 20-30 years' period variability except before 1910 (Figure 3.5b). 1700-yrs pre-industrial run of coupled climate model (CESM-LE) personally provided by *Prof. Sang-Wook Yeh* (swyeh@hanyang.ac.kr) also show this fluctuation of moving correlation, although the timings of maximum/minimum correlation are different and even sign of the correlation is changed (Figure 3.5c) although the opposite sign correlation is not significant.

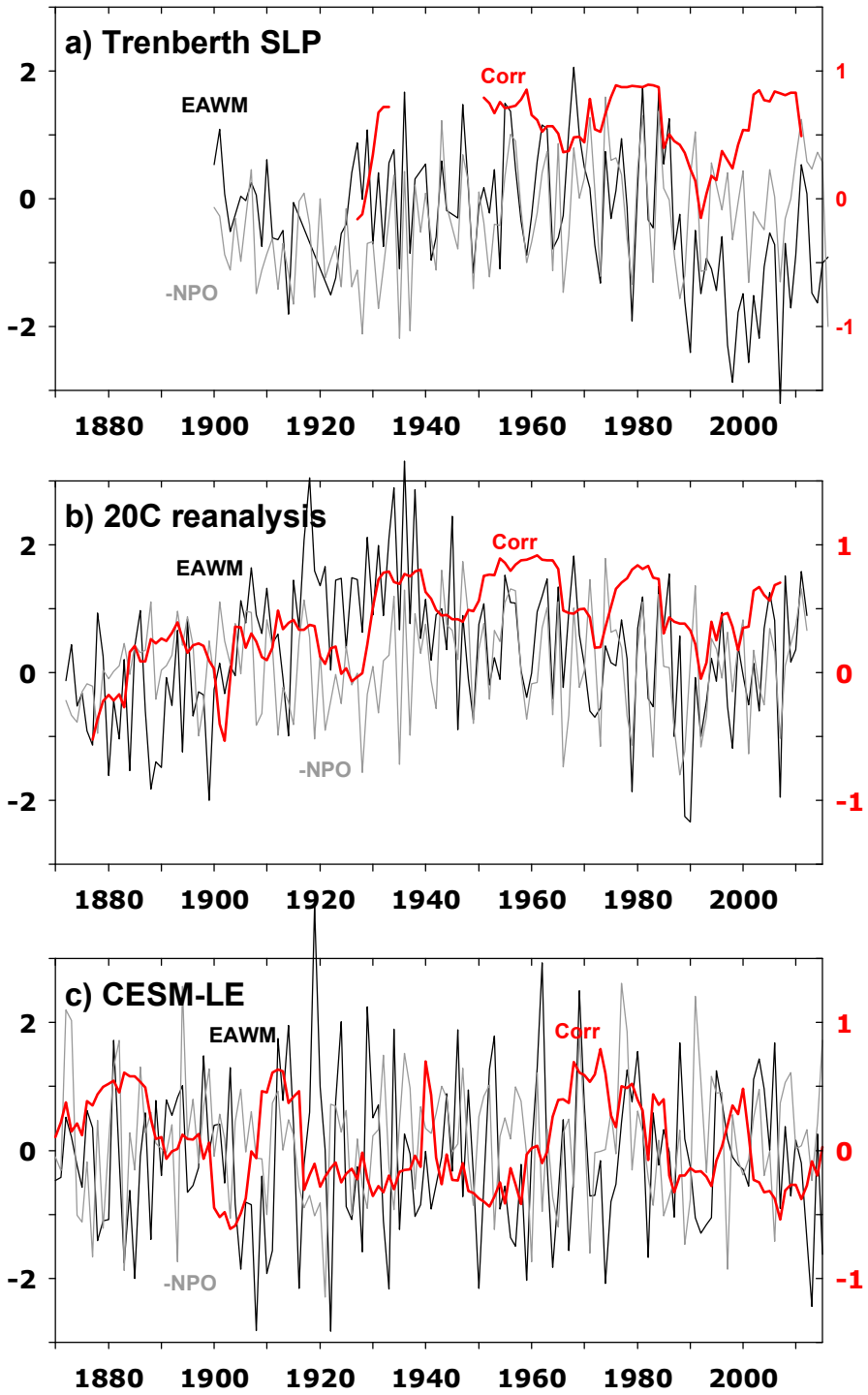

Figure 3.5. 11-yr running correlation coefficient (red) between the EAWM (black) and negative NPO (gray) indices obtained from (a) Trenberth SLP, (b) 20C reanalysis, and (c) coupled model (CESM-LE).

3.1.2 Relationship between SST and atmospheric forcing patterns

a. Long-term relationship between SST, atmospheric forcing patterns and ENSO

To investigate the relationship between the atmospheric forcing patterns and SST in the western North Pacific, the interannual to decadal correlation coefficients between the SST and climate indices are shown selecting different months for the averages (Figures 3.6-3.10). OND, NDJ, DJF, JFM, FMA, and MAM in those figures denote the averaging months used for constructing yearly time series: for example, NDJ means November through January. As described in the caption of Figure 3.6, acronyms in rows (columns) indicate averaging months for SST (atmospheric indices), thus the diagonal panels indicate simultaneous correlations and lower (upper)–triangular panels represent atmosphere to ocean (ocean to atmosphere) influence.

The EAWM–SST correlation maps (Figure 3.6) show that negative correlation between the EAWM and SST when atmosphere leads ocean by few (1–2) months, supporting the cold air outbreak due to the EAWM cools the surface near the Korean Peninsula (strengthened EAWM causes cold SST.). The significant correlation area covers the marginal seas around Korea such as East/Japan Sea, Yellow Sea, and East China Sea and southeast of Japan. Most of the atmosphere to ocean influence (lower–triangular panels) shows similar spatial distribution. On the other hand, SST has insignificant influence to the variability of the EAWM (see upper–triangular panels in Figure 3.6).

The NPO–SST correlation maps (Figure 3.7) also show generally similar spatial distribution with that of EAWM–SST (Figure 3.6). The correlation is significant for the influence of the atmosphere on the ocean with lag of zero to 2 months, with large positive correlation (see “negative” NPO in Figure 3.7) south of Japan including marginal sea regions. Negative correlation area is also found north of 40°N near Kamchatka, consistent with the dipole structure of NPO/NPGO. There are significant correlations for the influence of ocean on the atmosphere, which is consistent with *Hirose et al.* [2009] which shows the influence of the

volume transport through Korea Strait into the JES on the a few-month lagged winter WP pattern.

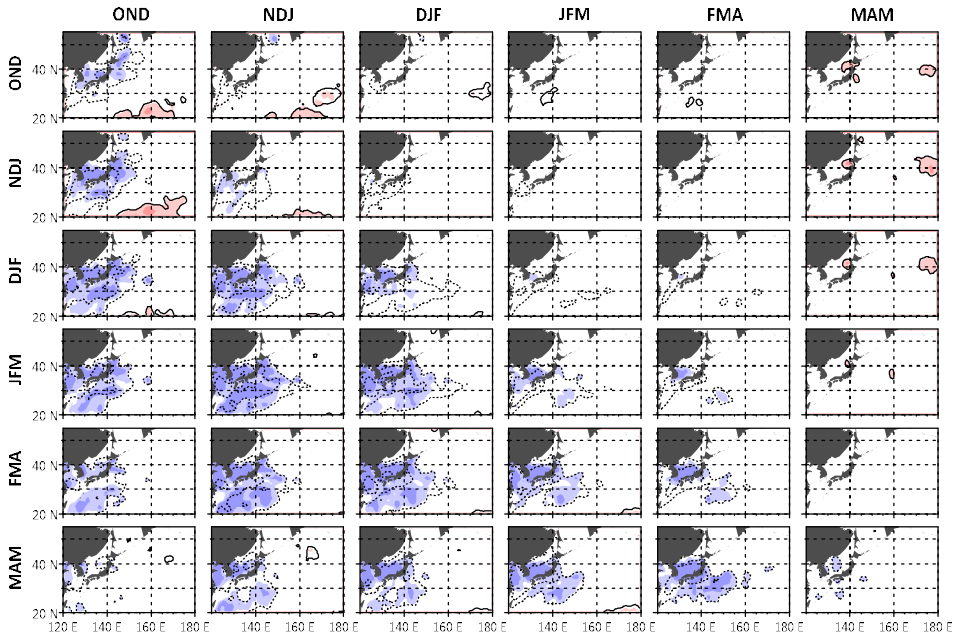

Figure 3.6. Correlation between yearly SST and EAWM averaged for three months. Acronyms in rows (columns) indicate averaging months for SST (EAWM). Contour interval is 0.2 (-0.9, -0.7, -0.5, -0.3, 0.3, 0.5, 0.7, and 0.9) and contours for -0.1 and 0.1 are removed for neat figure. Negative correlation is marked as dotted line. Significant correlation at 95% (99%) confidence level is shaded with light (dense) color.

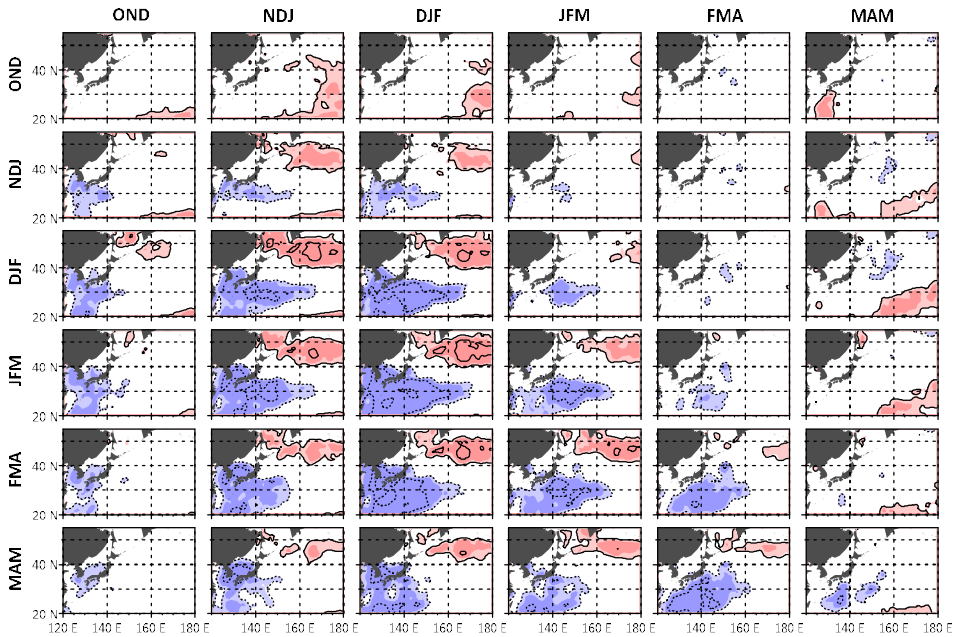

Figure 3.7. Same as Figure 3.6 but negative NPO.

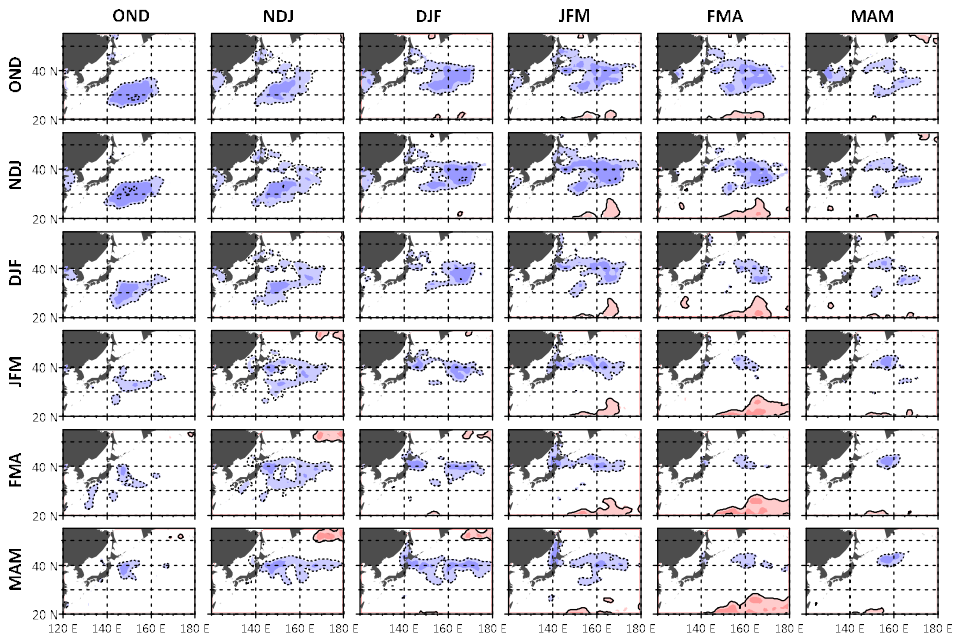

Figure 3.8. Same as Figure 3.6 but AL.

Interestingly, there is always significant negative correlation between the AL (intensity) index and KOE SST regardless of the averaging months from OND to MAM (Figure 3.8). When the SST leads AL index (ocean leads atmosphere), the area of significant correlation is large and generally expands up to 30°N (for example, the map for NDJ SST and JFM AL in Figure 3.8). This negative correlation indicates that the increase of KOE SST leads the weakened AL. It contradicts with *Frankignoul et al.* [2011] who showed the significant influence of the OE shift to the lagged NPO/WP-like SLP (and upper-level geopotential height) changes. Indeed, there is insignificant correlation between the lagged NPO and leading SST in the region where OE flows (~40°N, ocean to atmosphere influence in Figure 3.7). However, the reason for this discrepancy is not clear yet.

While the significant correlation region is confined just along the 40°N for the case of AL leads (atmospheric influence to ocean, lower triangular panels in Figure 3.8). This is consistent with *Frankignoul et al.* [2011] who showed the positive SLP anomalies (weaker AL) can drives a northward shift of the OE, which can cause positive SST anomalies near the front. *Nonaka et al.* [2008] attributed the fast response to basinwide wind stress curl anomalies and barotropic Rossby wave adjustment. AL-related wind stress curl forcing generates some anomalies of SSH, MLD, or ocean temperature in the central North Pacific, which are propagated very fast westward via barotropic Rossby waves.

The influence of the AO on SST (Figure 3.9) is very limited to the marginal seas near Korea, except for the case of MAM SST and FMA/MAM AO, which show extended influence of AO to the open ocean area. The negative correlation area is found in the marginal seas which may be related to the influence of the cold air outbreak from the continents.

The ENSO–SST correlation (Figure 3.10) does not depend on the selection of averaging months for ENSO index. It only depends on the selection of averaging months for SST, suggesting long autocorrelation scale of the ENSO index.

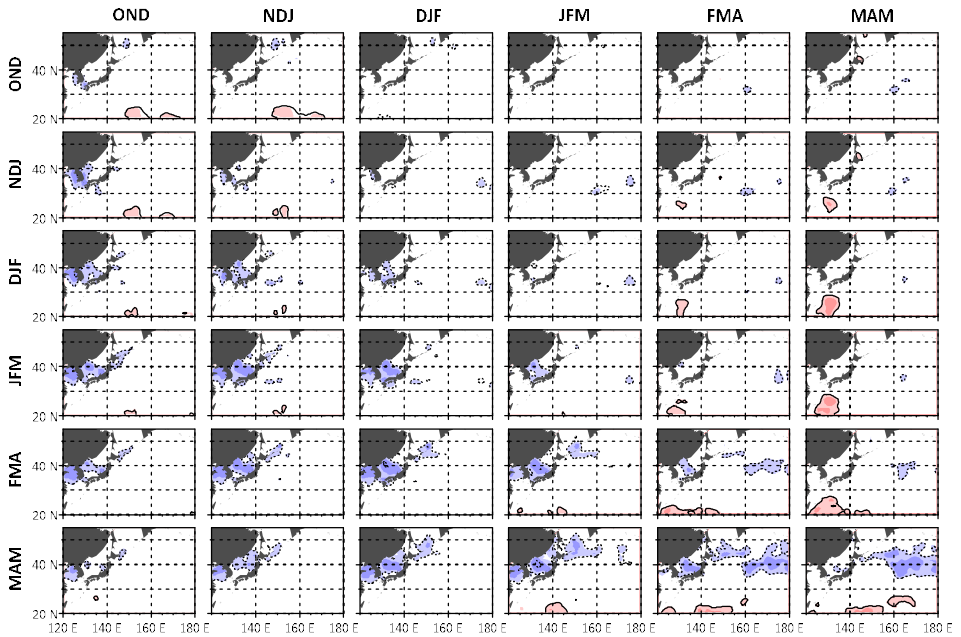

Figure 3.9. Same as Figure 3.6 but negative AO.

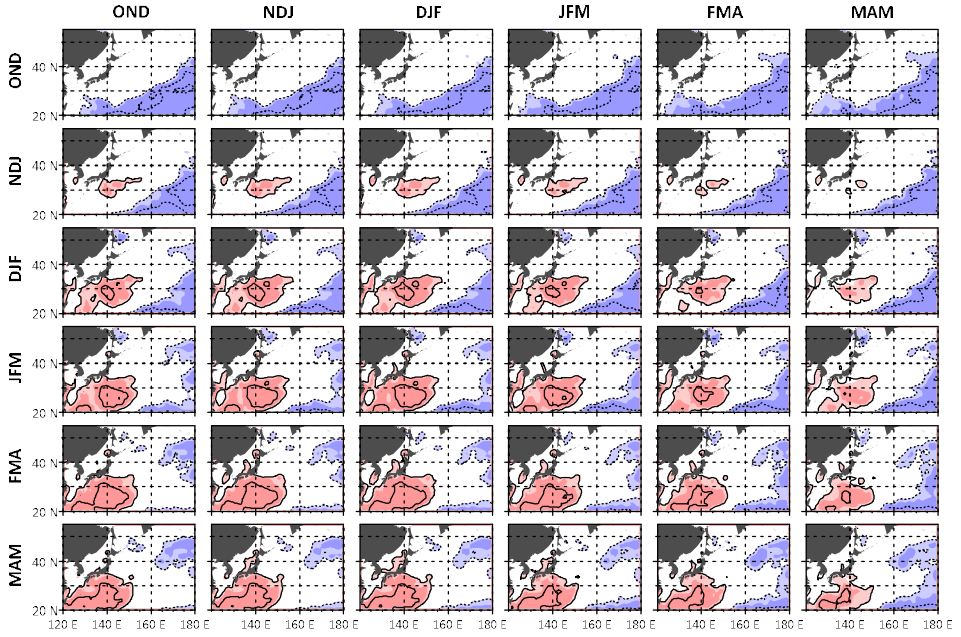

Figure 3.10. Same as Figure 3.6 but ENSO.

Considering lead-lag correlations between the climate indices and SST in the western North Pacific, DJF for atmospheric circulation and JFM for oceanic state (SST) are chosen for investigating the atmospheric influences on the ocean. This combination (DJF-JFM) shows the best correlation for atmosphere to ocean influence (lower triangular panels) in the most climate indices. Therefore, subsequent analyses were done with DJF indices and JFM SST in Chapter 3.

b. Regime−dependent impact of atmospheric forcing on the SST

As shown in section above (3.1.2a), during the entire analysis period (1965–2012), the EAWM and NPO were equally well projected onto the regional SST variability (correlation between JFM SST and DJF index shown in Figures 3.6 and 3.7). However, a close inspection shows a subtle difference; the EAWM is slightly more influential in the East Asian marginal seas, whereas the NPO is a little better projected in the Kuroshio recirculation region and in the subpolar gyre region southeast of Kamchatka.

The SST projection of the EAWM and NPO during the SM–HC epoch (1973–87) reveals nearly the same pattern (Figures 3.11a and 3.11c) but with somewhat overall higher correlations compared to that of the entire period (JFM-DJF pairs in Figures 3.6 and 3.7). The most striking feature during the WM–LC epoch (1988–2002) is that the impact of the EAWM was weakened and shrunk remarkably into a limited area in the East China Sea and southern JES (Figure 3.11b). The impact of the NPO was also much weakened especially in the Kuroshio recirculation region but slightly strengthened in the subpolar gyre region especially north of 40°N (Figures 3.11c and 3.11d), showing a clearer geographical separation from the EAWM impact, consistent with their insignificant correlation during the WM–LC epoch (see Table 2.1). This is also consistent with *Sugimoto and Kako* [2016] who showed that increased (decreased) role of net heat flux on the decadal changes of mixed layer depth anomalies in the recirculation gyre region before (after) 1990.

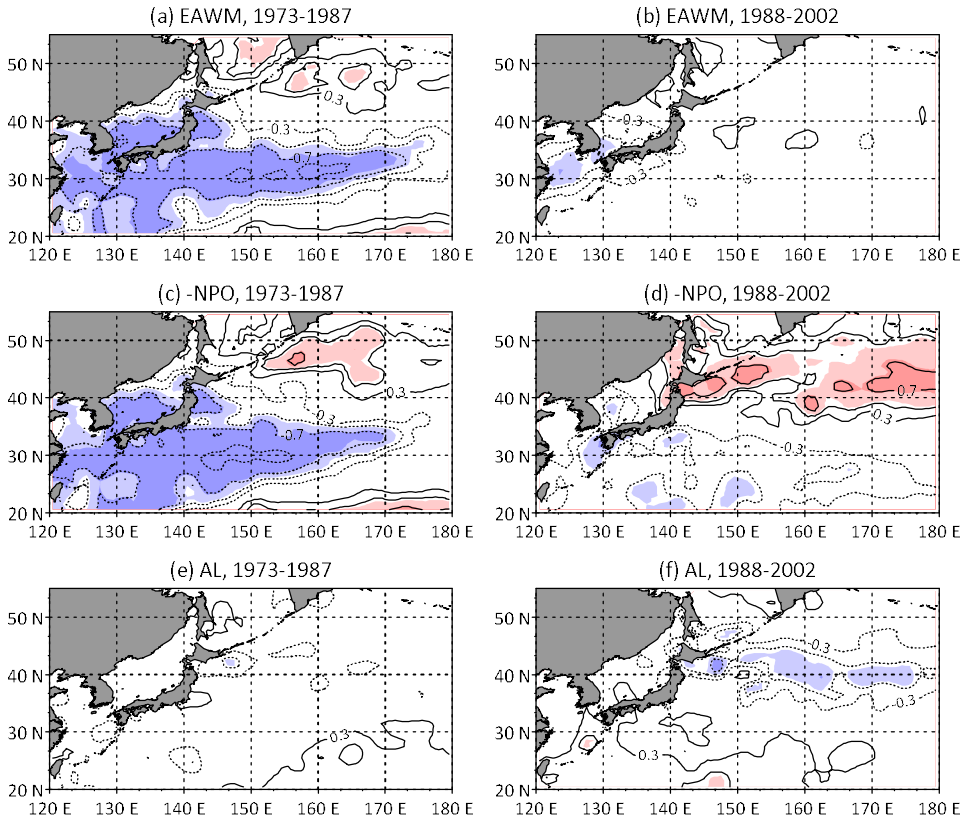

Figure 3.11. Correlation coefficients of JFM SST anomalies with (a-b) the EAWM, (c-d) the negative NPO, and (e-f) the AL for two contrasting periods, with significant correlations at the 95% (99%) confidence level marked with the light (dense) colors. Contour interval is 0.2 and contours 0.1 and -0.1 are removed for neat figure.

Also, an interesting period-dependency is found from the SST–AL correlation maps (Figures 3.11e and 3.11f). During the SM–HC period, the intensity of AL does not affect significantly in the western North Pacific. On the other hand, the influence of AL is observed along the OE after the 1988 regime shift (WM–LC). If the AL strengthened, cold oceanic temperature anomaly will be occurred associated with the positive wind stress curl forcing in the central North Pacific. This temperature anomaly can be propagated westward via Rossby waves. Indeed, *Frankignoul et al.* [2010] and *Nonaka et al.* [2008] attributed the meridional shift of the OE to the rapid barotropic response to the AL-like mode, which will be

discussed in detail later (Chapter 4). Indeed, the negative correlation (strengthened AL – negative temperature anomaly) is found in Figure 3.11f. Therefore, Figures 3.11e and 3.11f may support that a possibility of the epoch-dependency of the dynamics of barotropic Rossby wave for the OE.

In summary, the influences of EAWM and NPO to the winter SST is well observed in the marginal sea regions and south of Kuroshio Extension (KE) during SM-HC period, while NPO and AL impact the upper ocean thermal variability near the OE region during WM-LC period. However, the winter SST variability is not well explained with atmospheric forcing patterns in the KOE region, the mixed water region between KE and OE, during both SM-HC and WM-LC periods. To investigate the main contributor for the upper ocean thermal variability in the KOE region, the heat budget analysis is conducted with modeling data in the Chapter 4.

3.2. Regime-dependent changes of atmospheric states

In this section, the epoch dependent changes of atmospheric forcing patterns itself as well as relationship among them are presented to investigate the reason of the nonstationary relationship between EAWM and NPO, most influencing atmospheric forcing patterns to winter SST variability in the western North Pacific.

3.2.1 Regime-dependent changes of EAWM (SH) and NPO

As the EAWM index is very highly correlated (r = 0.77–0.95) with the SH index [*Park et al.*, 2012] (see also Table 2.1), the regime-dependent influence of the SH (as a proxy of the EAWM) was analyzed in relation to that of the NPO. The SH center is located to the southwest of Baikal Lake, with its easternmost extension over northeastern Siberia reaching as far east as the Bering Strait (Figure 3.12a). The subpolar center of the NPO is located at the northwestern border of the AL system, touching the northeastern ‘‘tail’’ of the SH system, while its subtropical center is found near the Kuroshio recirculation gyre. At the 500 hPa, the SH center

and the subpolar center of the NPO are found respectively upstream and downstream of the well-developed East Asian trough (Figure 3.13a).

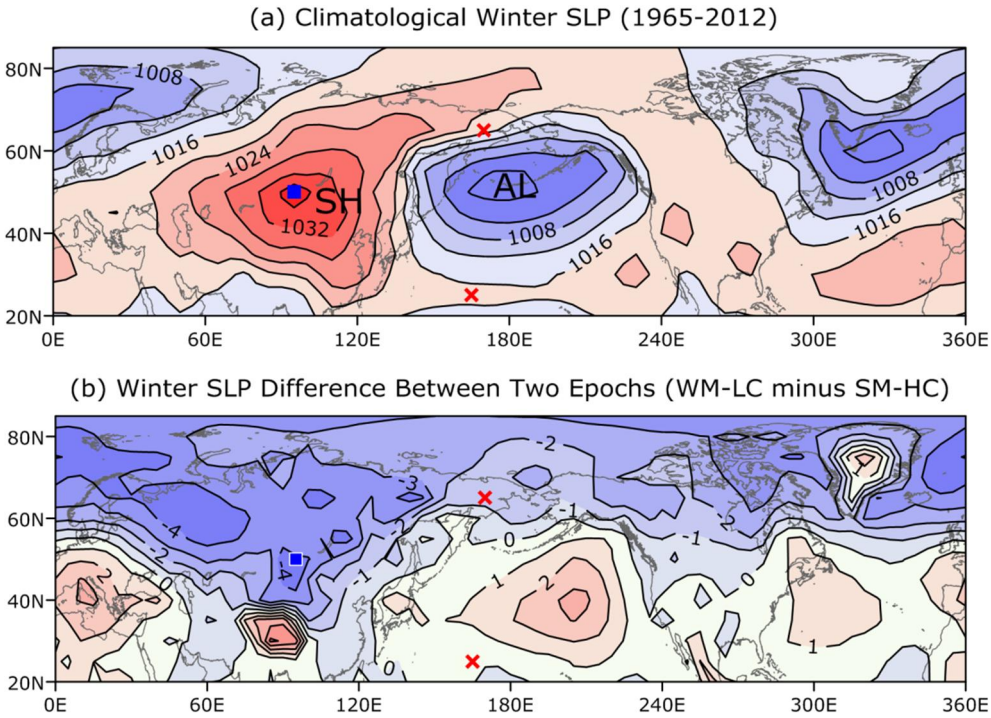

Figure 3.12. (a) Climatological winter mean SLP (in hPa) in the Northern Hemisphere north of 20°N during 1965-2012. The SH center (blue square) and the two centers of the NPO (red crosses) are indicated. (b) Winter SLP difference between two contrasting epochs: WM-LC (1988-2002) minus SM-HC (1973-1987).

During the SM–HC epoch (1973–87), the correlation map of SLP with the SH index (Figure 3.14a) shows that the area with significant correlations (shaded) extended far eastward, revealing a high and same sign (opposite sign) correlation with the subpolar (subtropical) center of the NPO, showing a tight linkage between the two circulation patterns. This tight connection can be verified when correlations are calculated in reference to the NPO index (Figure 3.14c). During the WM–LC epoch (1988–2002), on the contrary, the area with significant correlations with the SH index shrank radically around the SH center, thus disconnected completely from the two centers of the NPO (Figure 3.14b). Similar comments on such a disconnection can be made in reference to the NPO index (Figure 3.14d).

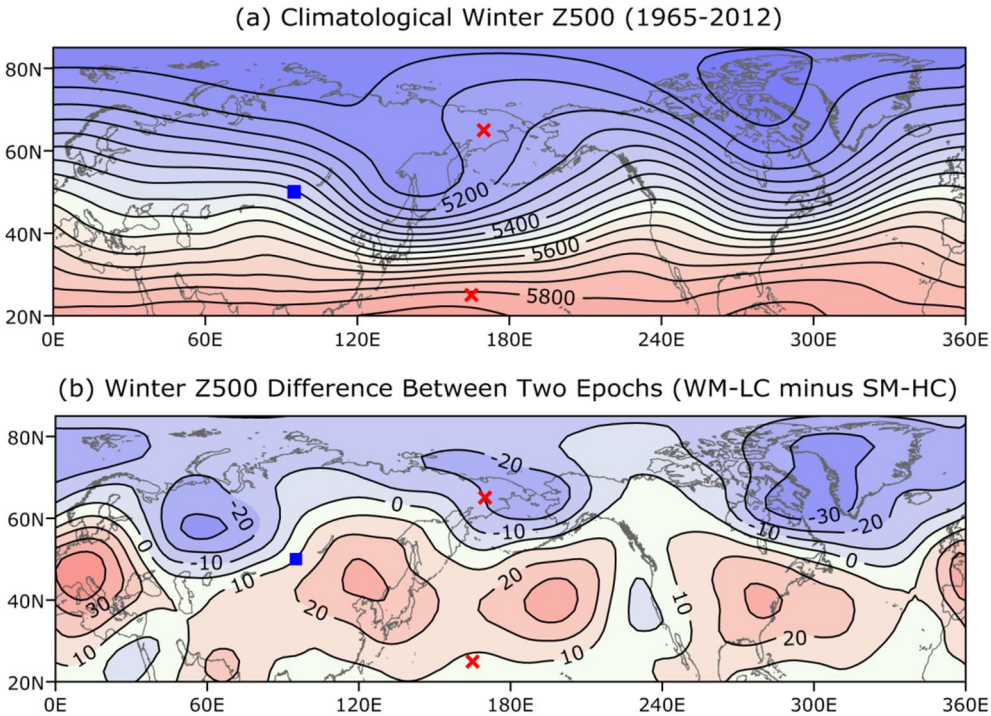

Figure 3.13. (a) Climatological winter mean Z500 (in m) in the Northern Hemisphere north of 20°N during 1965-2012. (b) Winter Z500 difference between two contrasting epochs: WM-LC (1988-2002) minus SM-HC (1973-1987).

Figures 3.12b and 3.13b suggest that the change in the EAWM–NPO relationship between the two epochs is associated with the hemispheric (planetary wave–like) changes in epoch-mean SLP and Z500 anomalies, which are superimposed on the overall opposite changes between the polar and middle latitudes. The latter feature in Figure 3.12b resembles the spatial pattern of SLP anomalies during a positive phase of the AO, which has intensified substantially since the 1988 regime shift [e.g., *Yeh et al.*, 2011 among others]. Most noticeable among the midlatitude changes is the abnormal weakening of SLP over the Eurasian continent, especially around the SH center during the WM–LC epoch, which is paired with a concomitant weakening of the southeastern part of the AL system over the eastern North Pacific [*Yeh et al.*, 2011]. These surface circulation

changes between the two epochs over the Eurasian continent and North Pacific are more clearly visible in the upper-level circulation represented by changes in Z500 (Figure 3.13b), with a pair of northwest–southeast oriented opposite centers of action over Siberia and another pair of north–south oriented opposite centers at about 170°W in the North Pacific. It will be shown later (section 3.2.4) that these are well linked to upper-level blocking features.

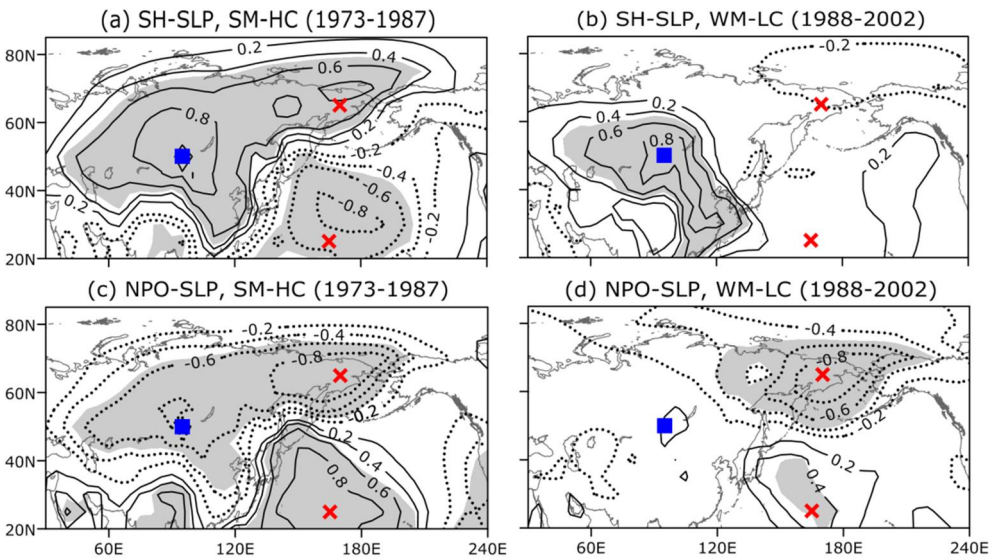

Figure 3.14. (a-b) Correlation maps of SLP anomalies with the SH index for the SM-HC epoch (1973-1987) and the WM-LC epoch (1988-2002), respectively. (c-d) Same as (a-b), but for the NPO index. The areas with significant correlations at the 95% confidence level are shaded.

3.2.2 Evolution of storm track across the regime shift

The spatial distribution of storm-track activity measured by 2–6-day bandpass filtered Z300 variance for the SM–HC and WM–LC periods as well as their difference (WM–LC minus SM–HC) are shown in Figure 3.15. For both periods, zonally elongated storm tracks are developed along ~40°N, with their peaks being located in the central basin close to the date line. Compared to the SM–HC period,

the storm tracks during the WM–LC period were strengthened significantly and extended far eastward into the eastern basin, whereas a noticeable weakening is observed at higher latitudes at the northeastern corner of Siberia (Figure 3.15c).

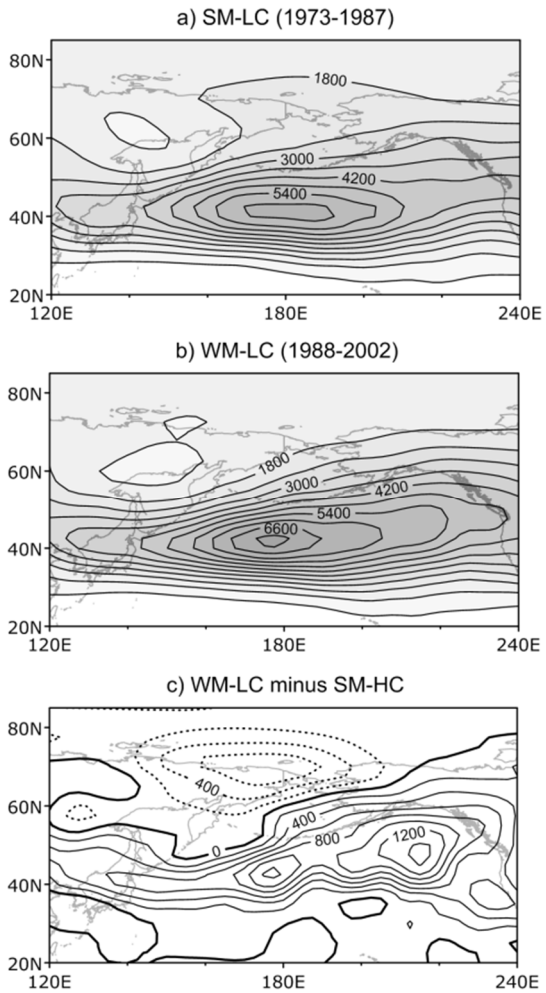

Figure 3.15. Time-mean storm track intensity measured by 2-6 day band-pass filtered Z300 variance for the (a) SM-HC and (b) WM-LC periods. Contour interval is 600 m^2 and the area of intensity over 4800 m^2 is darkly shaded. (c) Difference in intensity between the two periods, with the contour interval of 200 m^2 and negative anomalies being shown by dotted lines.

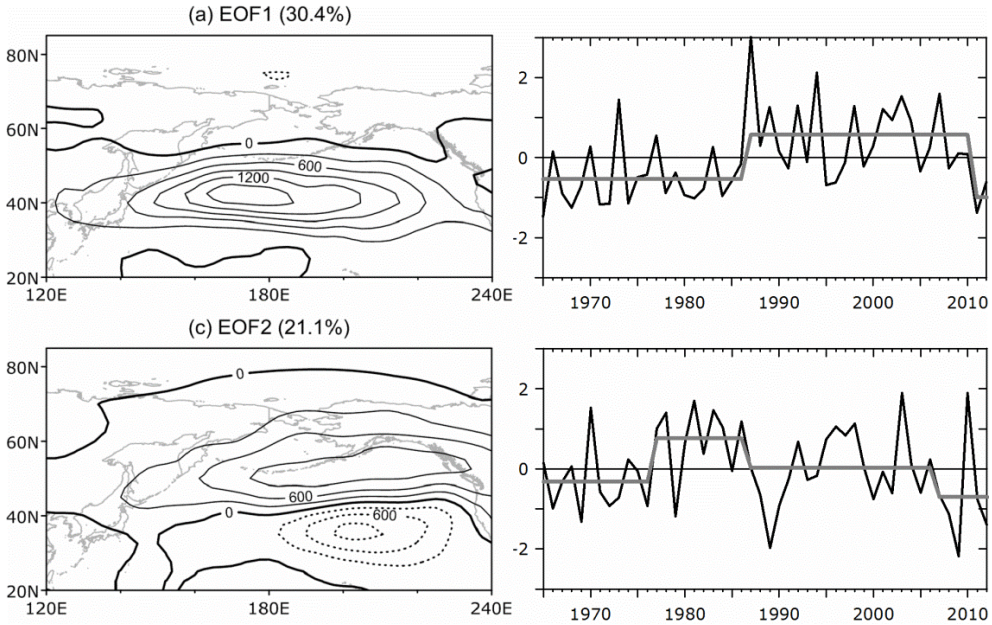

Figure 3.16. Storm track EOF and corresponding PC for the (a-b) first mode and (c-d) second mode. Contour interval is 300 m^2 and negative values are dotted in (a) and (c). Regime shift determination is shown by thick lines in (b) and (d).

Two leading EOFs and corresponding PCs of storm tracks for the entire analysis period (1965–2012) are shown in Figure 3.16. The EOF1 shows a zonally elongated monopole developed along 40°N in the central basin, a feature very similar to the raw storm-track pattern (Figure 3.15), whereas the EOF2 reveals a north–south dipole pattern straddling a nodal line at 40°N, mostly confined within the eastern basin east of the dateline. Interestingly, the PC1 (Figure 3.16b) reveals a clear regime shift around 1987, much the same as the NPO shown in Figure 3.3. On the other hand, the PC2 (Figure 3.16d), which is associated with the AL (or PNA)-like SLP pattern, shows dual regime shifts in 1977 and 1987, although such is somewhat at odd with the unique regime shift of AL and PNA in 1977 seen in Figure 3.3. When the SLP is regressed on the storm-track PC1 separately for the SM–HC and WM–LC (Figures 3.17a and 3.17c), the NPO-like pattern during the latter period shifts eastward by up to 20° in longitude compared to the former period. Also, the northwest–southeast oriented nodal line during the SM–HC

becomes nearly zonal because of its northward shift in the eastern basin during the WM–LC. Note that the SLP regression pattern in SM–HC is very close to the NPO defined by *Wallace and Gutzler* [1981], while the one in the WM–LC is similar to the EOF2 pattern shown by *Linkin and Nigam* [2008] and *Ceballos et al.* [2009]. A similar eastward shift is also observed in the EOF2 of Z500 anomalies in the latter period (cf. Figures 3.17b and 3.17d).

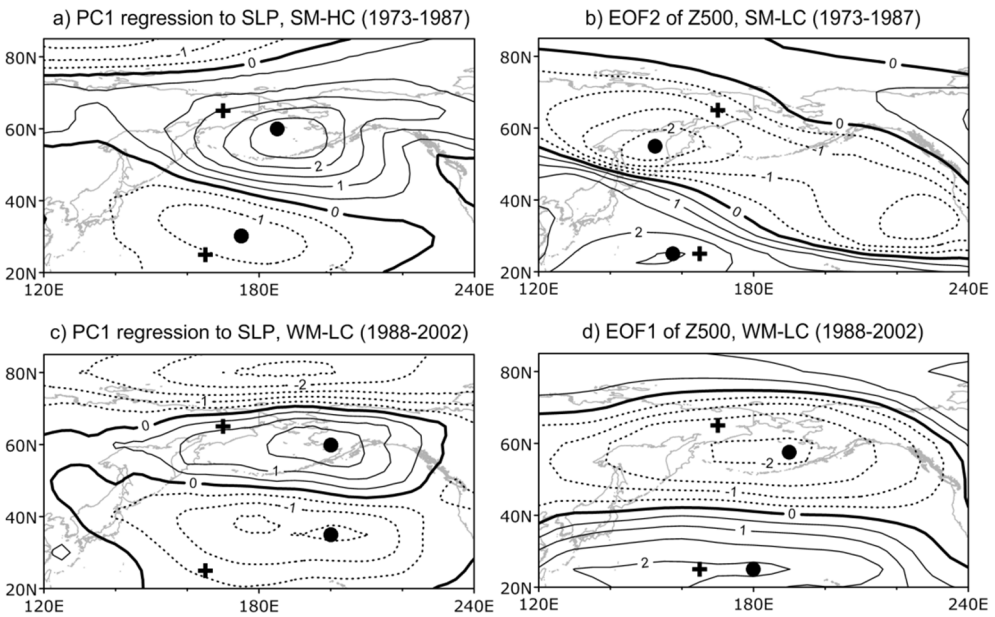

Figure 3.17. (a, c) Regression maps of anomalous winter SLP on the storm track PC1 for the (a) SM-HC and (c) WM-LC periods. (b, d) EOF2 of anomalous winter Z500 for the (b) SM-HC and (d) WM-LC period. Contour interval is 0.5 hPa for (a) and (c) but 5 m for (b) and (d). Crosses represent the two centers of action of NPO according to Wallace and Gutzler (1981), whereas black circles are those from the mapped patterns.

One is tempted to interpret Figure 3.17, which shows stormtrack-related circulation patterns, as the eastward-shifting NPO pattern because of its similar projection onto the latter pattern. However, the NPO as defined in the thesis according to *Wallace and Gutzler* [1981] does not show any eastward shift (see

Figures 3.14c and 3.14d). But, this stationary pattern of NPO may be caused by its definition using two fixed points. On the other hand, *Zhu and Sun* [1999] showed previously that ENSO exerts an important influence on the maintenance and development of the North Pacific winter storm track. This possibility will be tested below and show in effect that the observed eastward shift of intensified storm track and its related tropospheric circulation pattern during the WM–LC is consistent with a significant eastward shift of the ENSO influence toward the eastern basin.

3.2.3 Evolution of tropical influence across the regime shift

To document the regime-dependent tropical–extratropical connection, it is presented in Figure 3.18 that the lag correlations of the winter (DJF)-mean EAWM and NPO indices relative to the lagged 3-month-mean MEI (representing the seasonal ENSO forcing) for two contrasting periods before and after the regime shift. This is done by successively sliding the MEI time series by 1 month over a total lag range of ±2 yr such that a positive (negative) lag indicating the EAWM/NPO (ENSO) leading. During the SM–HC, the most significant correlation is observed at the zero lag for both the EAWM and NPO, although the NPO shows a much tighter connection with ENSO (r = 0.76: significant at more than the 99% level) compared to a moderate EAWM–MEI relationship (r = 0.53: significant at the 95% level but not exceeding the 99% level). The observed rapid decrease in correlation with increasing lag in either positive or negative direction with an insignificant correlation at a few months of lag may attest the simultaneous EAWM–ENSO and NPO–ENSO connections. Furthermore, as the EAWM and NPO are highly correlated during the SM–HC (Figure 3.4), the lag correlation betweeen the EAWM/NPO and ENSO indices (Figure 3.18a) may suggest a possibility of the simultaneous EAWM–ENSO–NPO triple connection in this period.

In great contrast to the triple connection, during the WM–LC period, no significant correlation between the ENSO and EAWM or NPO appears at any lag, except for one exception of a moderate correlation (r = 0.50) with the EAWM at a

lag of -1 yr, which indicates that the preceding winter ENSO affects the contemporaneous EAWM. Note that the case is not the SM–HC, during the correlation between the EAWM and ENSO are marginal (r = 0.45). On the other hand, except for the highest correlation centered at the zero lag in the SM–HC, no significant lagged correlation is observed between the NPO and ENSO for both periods. Though not significant at the 95% level, the strongest correlation (r ~ -0.4) between the NPO and ENSO during the WM–LC occurs when the NPO leads ENSO by about 1 yr, which might support the seasonal footprinting mechanism of *Vimont et al.* [2003]. However, the case is not for the SM–HC, during which the 1-yr lag correlation between the two indices is close to zero, suggesting that the NPO feedback on ENSO is not a robust feature in the analysis. It will be focused below on the simultaneous relationship between ENSO and both the NPO and EAWM.

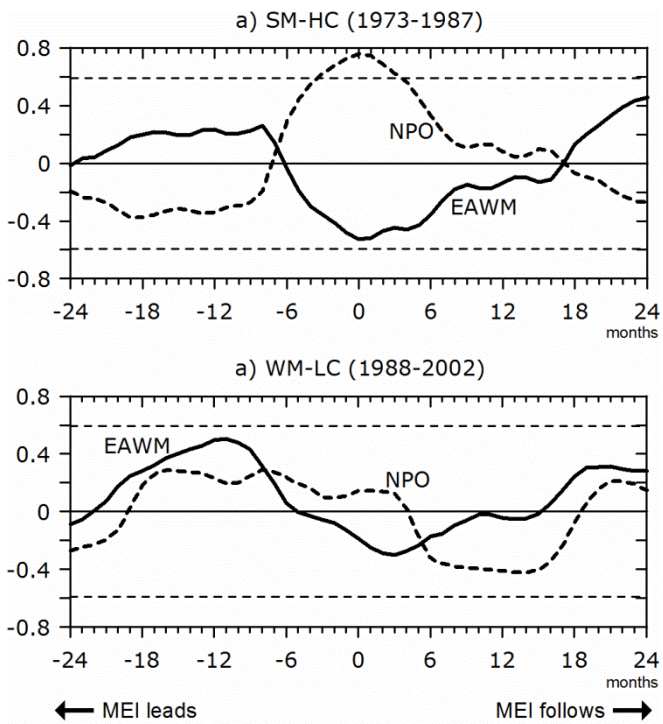

Figure 3.18. Lag correlations of the EAWM index (solid line) and NPO index (thick dotted line) with lagged ENSO index (MEI) for the (a) SM-HC and (b) WM-LC periods. Confidence level at 95% is indicated by horizontal thin dotted lines.

Lag is in month and a negative (positive) lag means that the ENSO leads (lags) the EAWM or NPO.

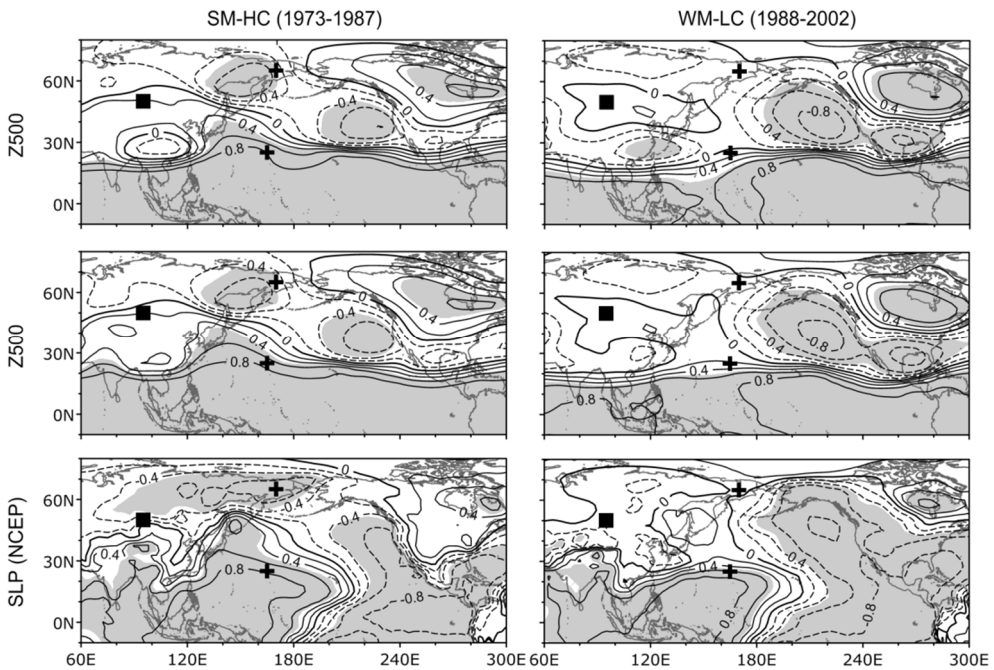

Figure 3.19. Maps of correlation of the ENSO index with anomalous winter (DJF) NCEP (a-b) Z300, (c-d) Z500, and (e-f) SLP for the SM-HC (left) and WM-LC (right) periods. Shading indicates the areas of significant correlation above the 95% level. Note that the SLP data is also supplied from NCEP to cover the tropical regions. Centers of action for the SH and NPO are marked by black squares and crosses, respectively.

Maps of contemporaneous correlation of winter Z300, Z500, and SLP anomaly fields relative to the MEI separately for the SM–HC and WM–LC are shown in Figure 3.19. For these two periods, both common and contrasting features appear. As expected, the most widespread and significant positive correlation with ENSO is found in the tropics south of 20°N regardless of the tropospheric levels and periods, except for the SLP in the eastern tropics, where the sign is reversed, in line with the classical ENSO definition. The most remarkable difference between the two periods is that in the SM–HC the significant tropical influence extends

much farther northward up to 40°N in the western boundary region (including the Kuroshio recirculation region and the JES) compared to its near-zonal poleward limit at ~20°N during the WM–LC. This is accompanied with a maximum negative correlation near the northern NPO center in the former period (Figures 3.19a and 3.19c), which is in great contrast to its absence in the latter period (Figures 3.19b and 3.19d). On the other hand, another negative maximum centered at (40°N, 140°W) in the eastern basin is paired with a positive pole found over northeast Canada, which is a common feature to both periods but with a slight intensification in the latter period. This feature is most evident in the Z300 and Z500 maps and resembles much the PNA teleconnection pattern.

Concerning the SLP maps, it is remarked that in the SM–HC (Figure 3.19e) both the northern and southern NPO centers are well correlated with ENSO, with a significant negative correlation at the northern center extending westward to the SH center. This is consistent with the observed significant triple correlations among the EAWM, NPO, and ENSO during the SM–HC (see Table 2.1). In contrast, this triple connection vanishes in the WM–LC (Figure 3.19f) during which the ENSO influence disappears at both the northern NPO center and the SH center, although a significant but somewhat weakened ENSO influence is still visible at the southern NPO center.

In summary, it suggests a significant simultaneous triple connection among the EAWM, NPO, and ENSO in the western North Pacific during the SM–HC, which vanishes in the WM–LC, during which the ENSO influence is more preferentially projected onto the PNA-like pattern in the eastern basin. Finally, it is interesting to relate Figure 3.19 with Figure 3.17 as both show a clear eastward shift of extratropical circulation patterns in the WM–LC compared to the SM–HC, so that the decadal changes of storm-track-associated patterns (Figure 3.17) could be partly explained by the ENSO pattern (Figure 3.19), although the ENSO index itself does not show any decadal shift around 1988 (Figure 3.3).

3.2.4 Upper-level blockings: control factors of SH/EAWM and NPO/WP

Takaya and Nakamura [2005a] pointed out that intraseasonal amplification of the SH can be caused by upper-level blocking over Siberia west of the climatological upper-level trough over the Far East, called ‘‘wave train’’ (Atlantic origin) type, which occurs in turn by amplification of quasi-stationary Rossby wave train coming from the Euro–Atlantic sector. *Takaya and Nakamura* [2005b] further suggested that the blocking to the east of the trough, called ‘‘Pacific origin’’ type, also affects the SH especially in the northeastern Siberia region. For the commodity of naming according to the representative landmark in the vicinity of the above two blockings, which will be referred as ‘‘Ural blocking’’ and ‘‘Kamchatka blocking” respectively.

A blocking index (BI) is calculated as the normalized projection of monthly Z500 anomaly patterns onto the composite blocking pattern [*Wang et al.*, 2010] as

$$\mathrm{BI} = \frac{\langle \Delta Z_b, \Delta Z_m \rangle}{\langle \Delta Z_b, \Delta Z_b \rangle}, \qquad (3.1)$$

where ΔZ_b is the winter composite of daily Z500 anomaly fields corresponding to the days of blocking events based on *Barriopedro et al.*’s [2006] criteria applied over a selected blocking sector, ΔZ_m is the monthly-mean Z500 anomaly field, and the brackets denote an inner product over a given projection area in each winter. It is defined the Ural (Kamchatka) blocking sector as 40°–80°E (140°E–180°) with a reference latitude of 60°N.

Figures 3.20a and 3.20c represent the composited blocking pattern ΔZ_b during 1965–2012 over the projection area for the Ural blocking (30°–85°N, 30°W–150°E) and Kamchatka blocking (30°–85°N, 70°E–110°W), respectively. The Ural blocking (at 500 hPa) is characterized by a well-defined blocking high over the Ural Mountains, which is associated with a downstream low over the surface high SH center (see also Figures 3.12b and 3.13b), while the Kamchatka blocking reveals a north–south dipole pattern, very similar to that of the WP/NPO [*Wallace and Gutzler*, 1981].

Consistent with *Wang et al.* [2010], the Ural blocking index is highly correlated with the SH index (r = 0.70; Figure 3.20b). As expected, it is also highly correlated with the EAWM index (r = 0.68). *Takaya and Nakamura* [2005a] showed that the SH amplification is achieved through vertical coupling in which

upper-level potential vorticity anomalies associated with the wave train induce anomalous cold advection in the downstream side of a blocking ridge, reinforcing the preexistent cold anticyclonic anomalies at the surface. The Kamchatka blocking is very tightly linked to the NPO (r = -0.82; Figure 3.20d). Furthermore, the Kamchatka blocking can be interpreted as the WP itself because their correlation reaches as much as -0.92, in addition to the very similar dipole pattern mentioned above. During the SM–HC epoch, the Ural and Kamchatka blocking indices were highly correlated (r = 0.76) to each other, while their correlation practically vanished (r = 0.18) during the WM–LC epoch, in good agreement with the results from the SLP data (see Figure 3.14).

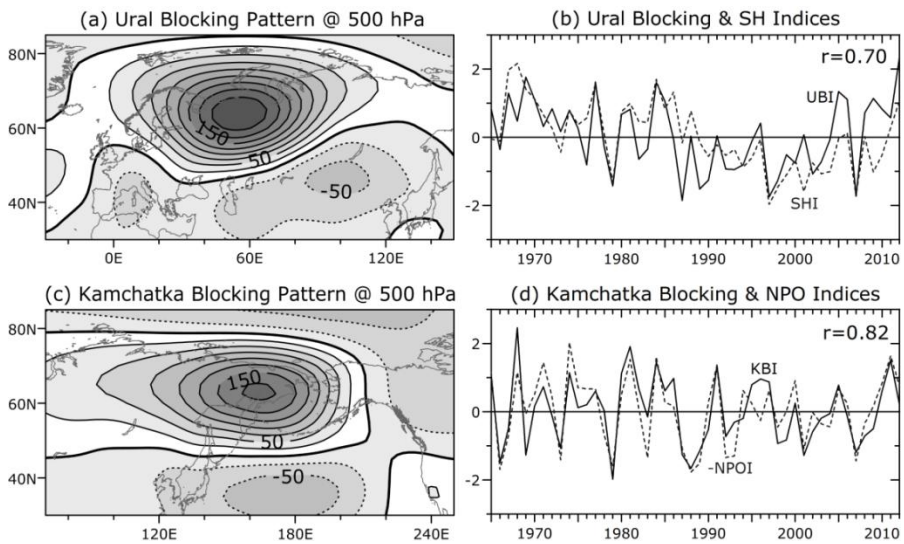

Figure 3.20. Blocking pattern (in m) over the projection area for (a) the Ural blocking and (c) the Kamchatka blocking. Comparison between (b) the Ural blocking index (UBI, solid) and SH index (SHI, dotted) and (d) the Kamchatka blocking index (KBI, solid) and negative NPO index (NPOI, dotted).

3.3. A tentative mechanism for the nonstationarity

3.3.1 Stationary wave flux

The horizontal component of stationary wave activity flux [*Plumb*, 1985] is a useful diagnostic for identifying the source and propagation of anomalous quasi-stationary waves in the middle to upper troposphere [*Karoly et al.*, 1989]. To better understand the regime-dependent tropical–extratropical connection in the western North Pacific in terms of stationary wave activity flux, it is regressed that winter Z500 anomalies on the WP index for the SM–HC and WM–LC and calculated the regime-dependent stationary wave activity flux according to the approach of *Karoly et al.* [1989]. A similar analysis but for the NPO for different periods has been previously discussed by *Wang et al.* [2007]. Figure 3.21 shows the wave activity flux at 500 hPa associated with the WP pattern in the two contrasting periods as well as their difference (SM–HC minus WM–LC). During the SM–HC (Figure 3.21a), the WP-regressed anomalous Z500 field reveals high-latitude negative anomalies that are widely developed over entire northern Eurasia, from west Russia, passing through Siberia, to the Bering Strait. This widespread negative anomaly field contains two centers: one near the Ural blocking center and the other near the Kamchatka blocking center. Associated with the Ural blocking is the wave activity flux coming from Scandinavia, showing a gradual equatorward bending downstream of the blocking, a feature largely consistent with the wave activity flux associated with the amplification of the Siberian high described in *Takaya and Nakamura* [2005a].

On the other hand, in the Kamchatka blocking case the incoming poleward wave activity flux propagates northward across the East China Sea and JES, where the flux intensifies substantially and bends progressively northeastward before arriving at the north ofKamchatka. This represents a remarkable poleward wave activity flux originating from the subtropics. Note that the propagation of Rossby waves depends on the basic state and the region of mean westerlies (easterlies) in the extratropical (tropical) western North Pacific is favorable (unfavorable) for their propagation [*Dawson et al.*, 2011]. Note also that the amplification of wave activity over the JES is consistent with *Yamamoto and Hirose* [2011], who suggested a tight dynamic link between the JES cold SST and the enhancement of the Okhotsk low, although such a link is inconclusive in a more recent work by *Seo et al.* [2014a]. At midlatitudes, there is a wave train–like anomalous Z500 pattern that developed all the way from the central North Pacific to the central North

Atlantic, with associated wave activity propagating dominantly eastward between the two oceans across North America.

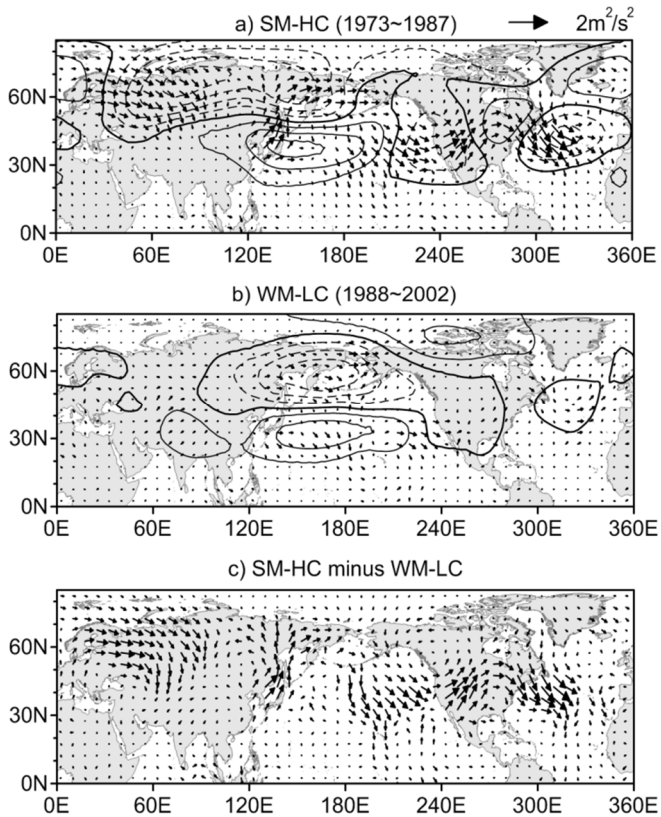

Figure 3.21. Stationary wave activity flux (in $m^2 s^{-2}$; scale is given in the top-right corner) superimposed on the anomalous winter Z500 field regressed on the WP index for the (a) SM-HC and (b) WM-LC periods. (c) Difference in wave activity flux between the two periods.

In contrast, the WP-regressed anomalous Z500 field for the WM–LC (Figure 3.21b) is mostly confined within the North Pacific basin and eastern Siberia, with associated wave activity flux remarkably weakening by a factor of 2 or more compared to the former period. Also, there is no evidence of the poleward propagation of wave activity along the western margin, nor of the eastward propagation of the midlatitude wave train–like feature between the Pacific and Atlantic basins, in stark contrast to the SM–HC epoch. Therefore it is suggested

that the tropical–extratropical teleconnection associated with the WP pattern of anomalous atmospheric circulation can be achieved via the propagation of stationary wave activity along the western margin of the North Pacific, a mechanism valid for the SM–HC but not for the WM–LC period.

3.3.2 Relationship with ENSO

To understand why there is a regime-dependent poleward flux of stationary wave activity in the western margin of the North Pacific it is examined in Figure 3.22 anomalous SLP, surface winds, and surface air temperature regressed on both the EAWM and negative ENSO indices for the SM–HC and WM–LC as well as their difference (SM–HC minus WM–LC). The negative (positive) ENSO index corresponds to the La Niña (El Niño) phase of ENSO and is used here to compare better, with the influence of the EAWM having generally a simultaneous negative correlation with ENSO (Figure 3.18). Although in the extratropics there are interesting features of the NPO-dominant EAWM-related pattern in the western North Pacific during the SM–HC (Figure 3.22a as compared to Figure 3.22b) and the PNA-dominant ENSO related pattern in the eastern basin during the WM–LC (Figure 3.22e as compared to Figure 3.22d), it is focused here on the regime-dependent tropical patterns in surface variables because it is mostly interested in tropical heating sources.

The EAWM- and ENSO (La Niña)-related patterns in the tropics south of 20°N during the SM–HC (Figures 3.22a,d) are very similar, with both showing a widespread surface air cooling associated with anomalous easterlies over the central and eastern tropical Pacific and anomalous westerlies over the eastern tropical Indian Ocean. In addition, both patterns show an isolated tropical warming in the Philippine Sea, which extends toward the subtropical central North Pacific along with anomalous southwesterlies originating from the equator between 130° and 160°E. There is evidence in both patterns of an anomalous cyclonic circulation centered near the Philippines (10°N, 125°E), with cold northerlies in the South China Sea and warm southerlies in the Philippine Sea. The observed high degree of similarity between the EAWM- and La Niña–related tropical patterns during the

SM–HC is consistent with the Pacific–East Asian teleconnection mechanism of *Wang et al.* [2000], who argued that the anomalous Philippine Sea cyclone (anticyclone) links the central tropical Pacific cooling (warming) and strong (weak) EAWM. *Wang et al.* [2000] further mentioned that the anomalous Philippine Sea cyclone is associated with enhanced convective heating and promotes anomalous upward motion, inducing upper-level divergence. In contrast, during the WM–LC, both the Philippine Sea cyclone and associated warming disappear in the EAWM pattern (Figure 3.22b), while the nearly identical or even slightly enhanced warming compared to the SM–HC is observed in the ENSO pattern (Figure 3.22e). This similarity of tropical ENSO pattern for the two periods is consistent with the already-mentioned nonexistence of the 1988 regime shift for ENSO. This information may suggest that the Pacific–East Asian teleconnection mechanism works well for the SM–HC but does not hold for the WM–LC, consistent with the contrasting correlations between the EAWM and ENSO during the two periods (see Table 2.1).

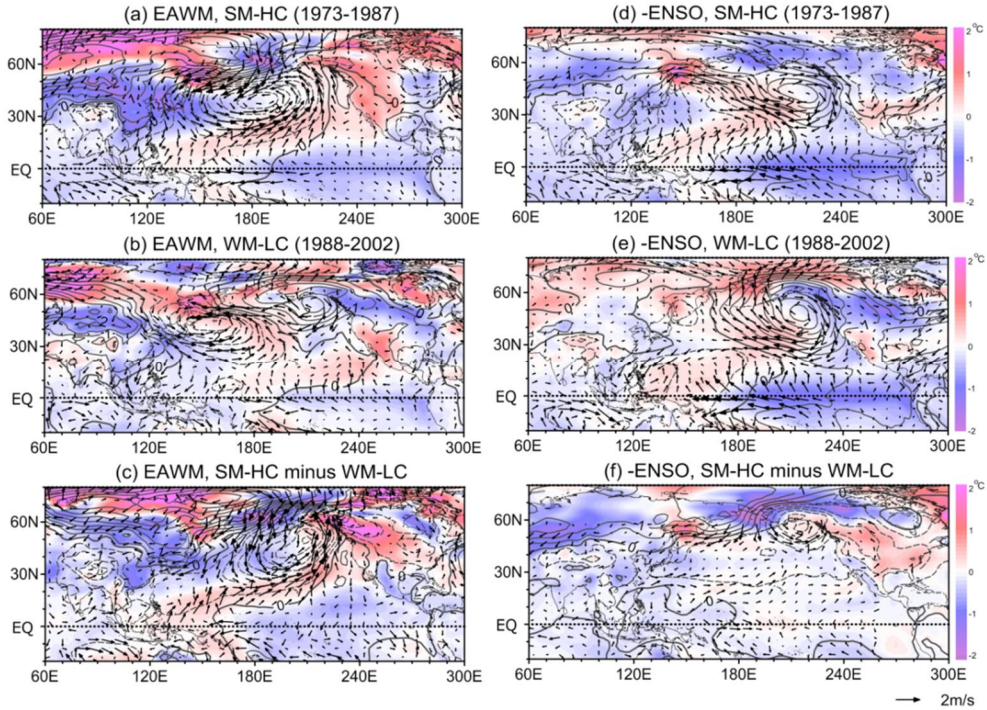

Figure 3.22. Regression of anomalous winter surface air temperature (color shading), SLP (contour), and surface winds (arrow) on the EAWM index during the (a) SM-HC and (b) WM-LC periods and (c) their difference. (d)-(f) As in (a)-(c), but on the negative ENSO index. Contour interval for SLP is 0.5 hPa and the scales for temperature and winds are indicated.

3.3.3 Poleward Rossby wave propagation

Finally, it is examined the regime-dependent propagation of Rossby waves. Surface heating especially in the tropics drives anomalous convection, which releases latent heat, and the surface precipitation rate is a useful parameter to measure the vertically integrated latent heat release [*Dawson et al.*, 2011]. Also, a series of alternating upper-level divergence (associated with convection) and convergence (associated with subsidence) can be generated by a propagating Rossby wave train. However, the surface precipitation rate depends greatly on the weather conditions especially on the presence of cyclones and storms [*Trenberth*, 2011]; thus, the vertical motion (convection/subsidence) inferred from it might be

much biased by extratropical storm-track activity. Therefore, it is instead used the total precipitable water (TPW), which is believed to be less sensitive to stormtrack activity, to infer propagating Rossby waves, assuming that a positive (negative) TPW may correspond to an upper-level divergence (convergence) centered at an anomalous anticyclone (cyclone) in the upper-level circulation field. With this idea in mind, it is shown in Figure 3.23 maps of correlation between the TPW at each data point and three climate indices (EAWM, -NPO, and -ENSO) for the SM–HC (Figures 3.23a,c,e) and WM–LC (Figures 3.23b,d,f). The monthly TPW data are from the NCEP Reanalysis 1. During the SM–HC, there clearly are three well-defined centers of alternating positive–negative–positive TPW anomalies along the western margin of the North Pacific, each located in the vicinity of the Philippines, the Korean Peninsula, and the Okhotsk Sea. The latter places correspond reasonably well to the theoretical Rossby wave train forced by a western Pacific equatorial heating source placed at 120°E in *Jin and Hoskins* [1995, their Figure 16d]. However, it is noted that the tropical–extratropical teleconnection along the western margin is significantly stronger and more widely developed in the EAWM- and NPO-related patterns (Figures 3.23a,c), which reveal nearly the same feature, than in the ENSO pattern (Figure 3.23e). This might be related to a positive combination or near-resonant interaction [*Held et al.*, 2002] between the tropical heating-induced Rossby wave train and the Tibetan orography-induced anomalous cyclone of the East Asian trough, which should yield stationary waves much stronger than those generated by tropical heating alone.

During the WM–LC, the western margin teleconnection weakens considerably in all three patterns (Figures 3.23b,d,f) and there appears to be no complete connection between the tropics and high latitudes, with the interruption occurring in the vicinity of the Korean Peninsula. This interruption is associated with a significant weakening of the East Asian trough during the WM–LC (see Figure 3.13b for a pronounced anomalous Z500 anticyclone centered at 45°N, 125°E), which combines negatively (or destructively) with the tropical heating induced wave train, thus inhibiting the latter from propagating farther northward. The clearest example for this may be the ENSO pattern (Figure 3.23f) showing no evidence of the northward propagation of the Philippine Sea signal despite a slightly enhanced TPW in the Philippine Sea during the WM–LC, which is rather

consistent with a slightly enhanced surface air temperature (Figure 3.22e). In addition, the NPO pattern during the WM–LC (Figure 3.23d) is mostly disconnected from the tropics. On the other hand, there is an eastward shift of the significant Okhotsk signal toward the eastern basin, which is likely related to the eastward shift of the storm-track pattern (Figure 3.17), which is in turn partly explained by the eastward intensified ENSO pattern during the WM–LC (Figure 3.23f), as mentioned previously.

Based on the above analyses, a tentative mechanism for the nonstationary relationship between the EAWM and NPO is proposed as follows: During the SM–HC, the East Asian trough deepens because of the strengthened Tibetan orographic forcing under strong monsoon winds, creating an anomalous upper-level cyclone north of the Korean Peninsula (Figure 3.13b; the sign is to be reversed for the SM–HC anomalies). The latter cyclone is in phase with the Rossby wave train generated by tropical heating in the Philippine Sea (Figures 3.19c and 3.21a), thus reinforcing the latter by a near resonant effect. This intensified tropical–extratropical teleconnection along the western margin, as clearly evidenced by the northward-propagating significant wave activity flux (Figure 3.21), makes a tight triple connection among the EAWM, NPO, and ENSO during the SM–HC. On the other hand, the abrupt decline of the EAWM after the 1988 regime shift induces a concomitant weakening of the East Asian trough, creating a pronounced anomalous anticyclone north of the Korean Peninsula (Figure 3.13b), which is in opposite phase with the Rossby wave train originating from the tropics, thus inhibiting the wave train from propagating farther northward. Therefore, the connection between the EAWM and NPO through the tropical teleconnection along the western margin breaks down in theWM–LC. In addition, the eastward shift of the storm track and the associated circulation pattern in the WM–LC (also associated with the tropical teleconnection) may further unfavor the tight connection between EAWM and NPO. The analysis highlights the pivotal role played by a decadal shift of the East Asian trough, an immediate consequence of the 1988 regime shift of the EAWM. It may be concluded therefore that the primary cause of the nonstationary relationship between the EAWM and NPO is the recent abrupt decline of the EAWM since the late 1980s, if one admits the latter decline as a starting point of discussion, although the latter issue is currently the subject of active research.

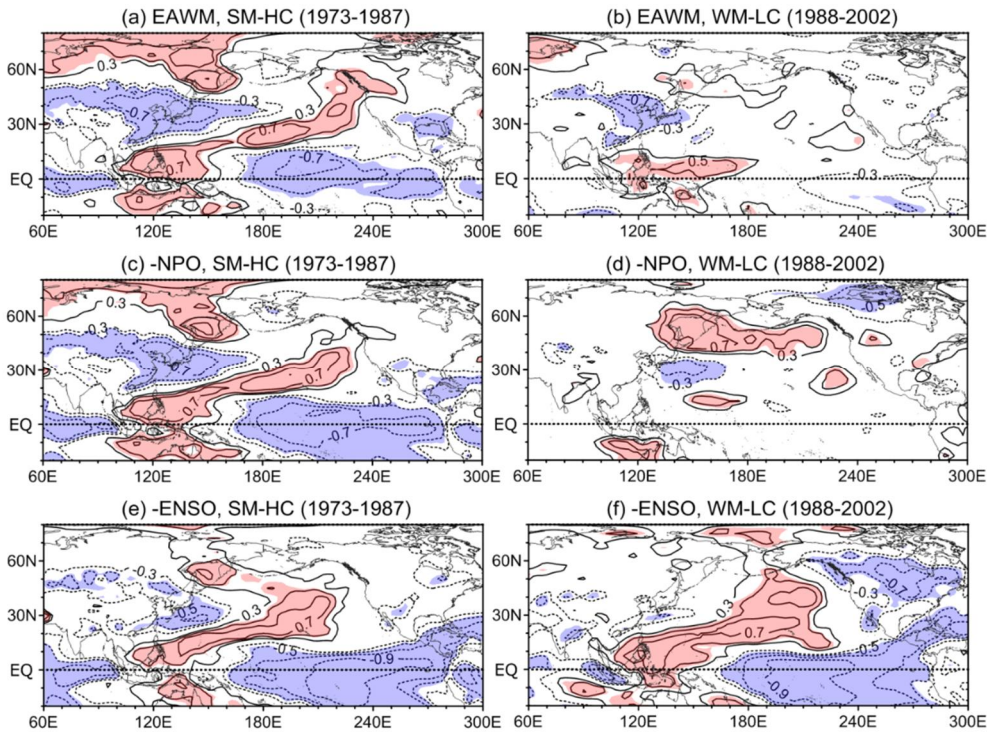

Figure 3.23. Maps of correlation between the total precipitable water and the EAWM index for the (a) SM-HC and (b) WM-LC. (c), (d) As in (a), (b), but for the negative NPO index. (e), (f) As in (a), (b), but for the negative ENSO index. Color shading indicates the areas of significant correlation above the 95% level.

Chapter 4. Epoch-dependent contributions of ocean dynamics to upper-ocean thermal variability

In the previous Chapter 3, the influences of the atmospheric forcing pattern on the SST variability are considered. As shown in *Park et al.* [2012], in the period before 1990 (1970-1989) the EAWM was largely responsible for the SST variability in most of the western North Pacific, whereas ocean dynamics became increasingly important there over the period 1990-2005, in consistent with the sub-section 3.1.2b showing epoch-dependent contribution of EAWM/NPO to the SST in the western North Pacific, although the increased role of the ocean dynamics after 1990 is not detailed.

4.1. Spatio-temporal variability of upper ocean heat contents in the western North Pacific

4.1.1 EOFs and PCs of T400

Two leading EOFs and corresponding PCs of temperature averaged from surface to 400 m (T400) in the western North Pacific are shown in Figure 4.1. Note that the T400 is spatially smoothed using 6°×4° window. Because the window filters eddy-like complicated spatial features and it does not influence area-averaged T400 as shown in section 4.1.2, the spatially smoothed variables are used in the most of subsequent analyses. The EOF1 (Figure 4.1a) explains 54 % of the total variance, with the same sign for the entire domain. The KOE region (square in Figure 4.1) corresponds to the area of the strongest variability, and the PC1 agrees well (r = 0.91) with the KOE T400 time series (Figure 4.1b). The KOE region is located in the center of action of EOF1, indicating that strong upper-ocean thermal variability. The EOF2, which explains 12 % of the total variance, shows a dipole pattern, with opposite signs especially between the KOE region and the Kuroshio recirculation south of the KE front (Figure 4.1c).

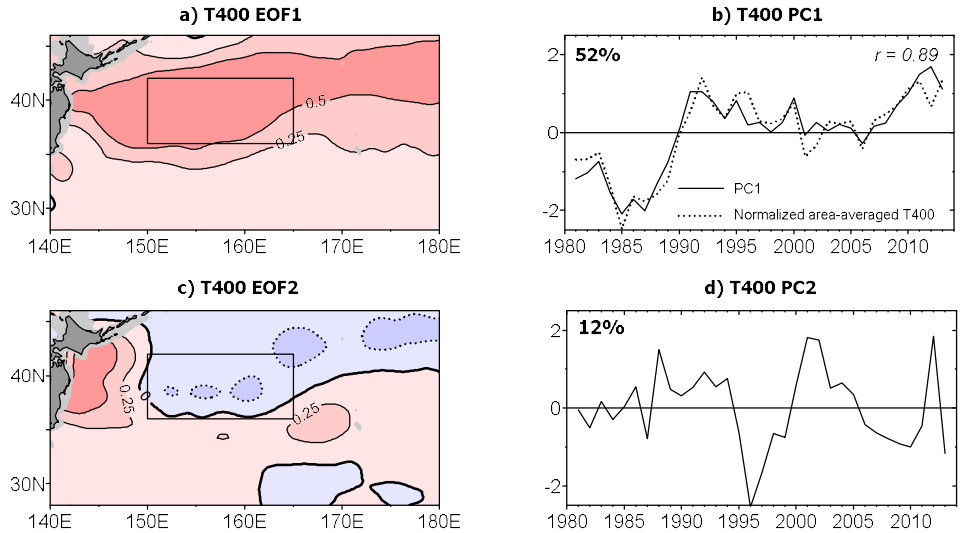

Figure 4.1. (a, c) EOFs and (b, d) corresponding PC time series for two leading modes of winter T400 in the western North Pacific. The PCs are normalized, so that EOFs denote the spatial pattern when the PC is unity.

4.1.2 Removing eddy contribution

Because ORCA12 model is significantly high resolution to permit eddy activities, eddy-contributed temperature anomalies are developed over the entire domain considered here (Figure 4.2). The positive (negative) T400 anomalies are located where anticyclonic (cyclonic) eddies are developed. The temporal mean of spatial correlation for the thirty-three (1981-2013) winter fields between T400 anomaly and SSHA is more than 0.75, which tells us that the thermal wind balance rules those eddy-contributed temperature anomalies. *Sugimoto and Hanawa* [2011] highlighted the importance of the eddy activities, especially those of anticyclonic eddy detached from the KE on the very limited area (142°-150°E, 35°-40°N) in their KOE region. However, eddies are spatially heterogeneous mesoscale features, with alternating positive and negative signs being mostly canceled among them when spatially integrating. Therefore, they do not contribute significantly to the large-scale thermal change of the KOE region. This can be observed in Figure 4.3. The area-averaged time series of T400 and its spatially-lowpass filtered one (T400L) show very similar distribution, while the highpass filtered one obtained by

subtracting T400L from T400 shows almost zero for most of the period. Instead, the eddy obscures westward propagating baroclinic Rossby wave signals [*Sugimoto and Hanawa*, 2009; 2011], so they should be removed, as it is interested in the relatively large-scale oceanic response in the KOE region to the basin-wide atmospheric forcing. Although the large scale atmospheric circulation can be influenced by those eddy-contributed temperature anomalies through the mesoscale air-sea interactions [*Seo et al.*, 2008; *Frenger et al.*, 2013], this is beyond of the present scope.

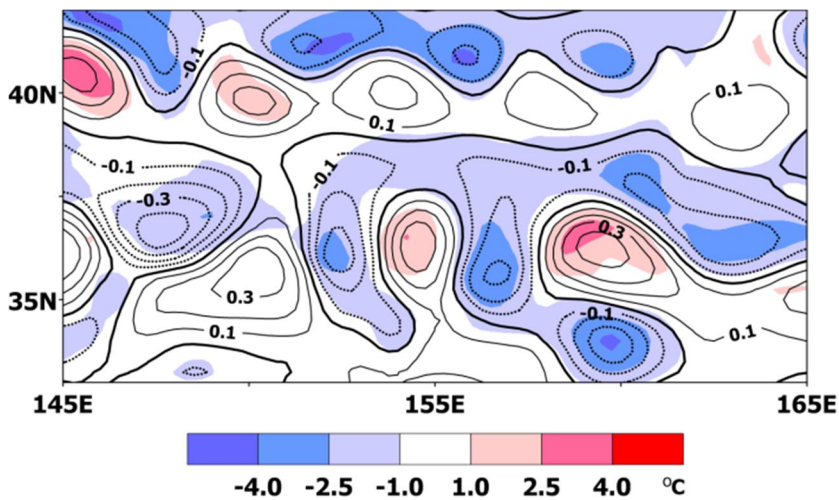

Figure 4.2. T400a (color, anomaly subtracting total period mean) and SSHA (contour, high pass filtered one using 6°×4° filter) for winter (DJF) 1984. Showing warm/cold eddy contribution to the temperature anomaly.

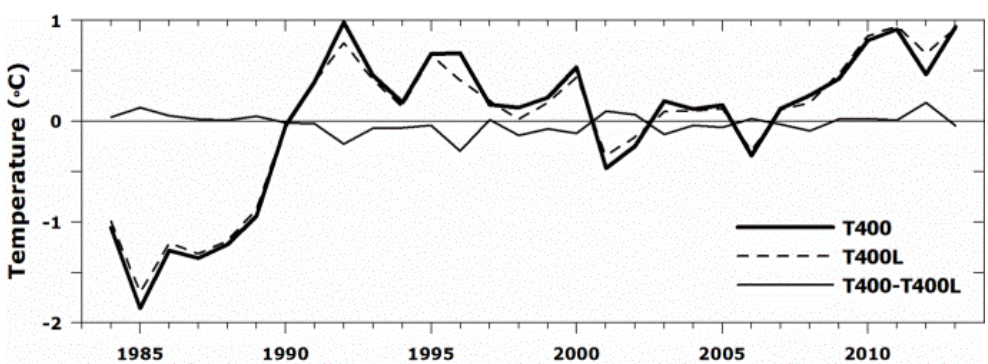

Figure 4.3. Area-averaged (36°-42°N, 150°-165°E) winter T400 (before filtering), T400L (after lowpass filter), and difference between T400 and T400L.

To separate eddy contribution quantitatively, it is first decomposed the ADV into the large scale term and small scale term as in *Huang et al.* [2010]. When the temperature (T) and velocity (u) terms are decomposed as low-frequency variability term ($\bar{T}$ and $\bar{u}$) and high-frequency term (T' and u'), decomposition of the ADV term can be written as:

$$-u\frac{\partial T}{\partial x} = -\bar{u}\frac{\partial \bar{T}}{\partial x} - \left(\bar{u}\frac{\partial T\prime}{\partial x} + u'\frac{\partial \bar{T}}{\partial x} + u'\frac{\partial T\prime}{\partial x}\right) \qquad (4.1).$$

The first term in the right-hand-side represents the low-frequency heat advection (LADV) and the sum of rest three terms is the high-frequency heat advection (SADV). Note that (4.1) shows the decomposition of the zonal heat advection only, but LADV, SADV, and other decomposed components of heat advection below consider also meridional heat advection components.

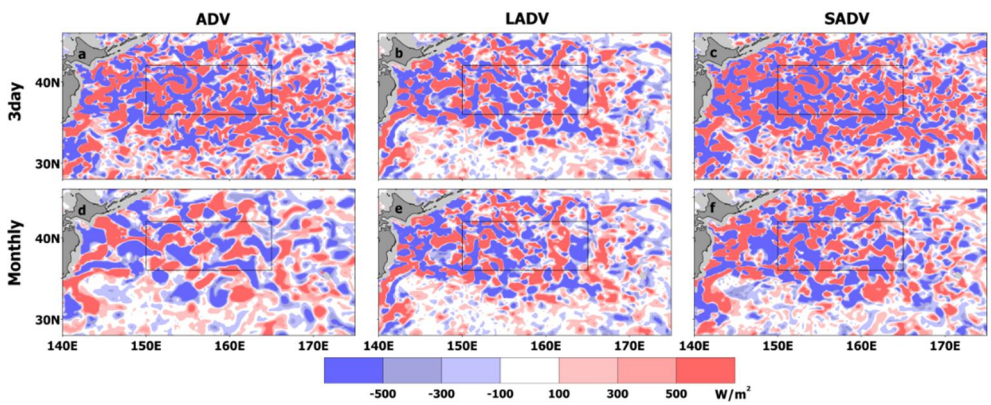

Figure 4.4. (a, d) Total ADV, (b, e) LADV, and (c, f) SADV for (a-c) 3day averaged snapshot and (d-f) monthly averaged calculated from 3day averaged fields.

Figure 4.4 shows the heat advection calculated from the 3-day averaged data, LADV, and the difference between them so that SADV of the 3-day averaged on 14-16 January 1997 (upper panels) and of the monthly averaged on January 1997

(lower panels). The monthly averaged LADV (Figure 4.4), which should only contain the large scale heat advection parts, has even smaller scale pattern than that of total ADV (Figure 4.4), although LADV shows relatively larger spatial scale patterns for the 3-day averaged field, indicating that LADV still has much eddy-like small scale features. So, spatially filter to T400 is applied to obtain non-eddy temperature components removing less than mesoscale variability by using 6° x 4° spatial filter in the previous section. Note that the total variance of the spatially filtered T400L in the large domain (140°-180°E, 28°-46°N) of KOE region is 0.318 $°C^2$, while that of non-filtered T400 is 1.150 $°C^2$ indicating more than 70% of the total variance of the temperature in the KOE region is filtered out when removing mesoscale features. The total variance is calculated by spatially averaging of temporal variance at each grid point. Therefore, the eddy component influences little to the mean heat content in the KOE region, while it affects greatly spatial complexity. So, most of the subsequent analyses only consider large-scale parts of the heat budgets and SST after applying spatial filters of which window size is 6°×4°. This spatial size is to suppress eddy fields in the western North Pacific region, so SST and heat advection budget is greatly changed but air-sea heat flux is not much influenced by this window filter, which indicates that heat flux has larger spatial scales. Note that area-averaged values of the SST and heat advection in the KOE region (150°-165°E, 36°-42°N) are not much influenced by this window. Because it is very difficult to extract and analyze the eddy and mean field value of heat budgets (SADV and LADV), this will be briefly investigated with KOE area-averaged value in later section.

4.2. Heat budget in the upper 400 m of the western North Pacific

To investigate the cause for the upper 400 m thermal variability of the western North Pacific, the heat budget is diagnosed with ORCA12 data.

4.2.1 Heat budget equation for upper ocean

a. Heat content as an indicator of ocean state

SST is one of popular indicators to describe thermal state of the ocean because it is readily available, and it is also necessary to compute an instantaneous estimation of the bulk flux algorithm [*Kelly and Dong*, 2004]. However, the upper ocean heat content is a better climate predictor than SST for the ocean-to-atmosphere feedback [*Yulaeva et al.*, 2001; *Kelly and Dong*, 2004; *Kelly et al.*, 2010], in which the air-sea heat flux is a key parameter. While the evolution of the vertically integrated heat content is directly related to the air-sea heat flux (ignoring lateral processes), mixed layer temperature (MLT) variations depend on changes in the mixed layer depth, in addition to the surface heat flux [*Dawe and Thompson*, 2007]. In contrast to a quick adjustment in the MLT budget, the heat content budget still shows significant drift in the 4 years after the PDO shift, especially in the KOE region, thus is more appropriate for investigating climate-scale ocean-atmosphere interactions. Moreover, when considering fixed depth heat content in budgeting, it is not necessary to consider the entrainment velocity and the temperature just below of MLD, which are two key parameters to determine heat budget due to entrainment, which is sensitive to the selection of those key parameters [*Stevenson and Niiler*, 1983; *Vivier et al.*, 2002].

b. Heat budget equation for upper-ocean heat content

The governing equation for potential temperature T in the ocean neglecting horizontal diffusion is,

$$\frac{\partial T}{\partial t} = \frac{1}{\rho c_p}\frac{dq}{dz} - \boldsymbol{u}\cdot\nabla T - w\frac{\partial T}{\partial z} + \frac{\partial}{\partial z}\left(\kappa\frac{\partial T}{\partial z}\right), \qquad (4.2)$$

where $\boldsymbol{u}$ (u, v) and w are the horizontal and vertical velocities, respectively, κ is the vertical eddy diffusivity, and q is the radiative heating. The specific heat at constant pressure c_p is set in the model to a fixed value as 4000 J kg^{-1} °C^{-1}. The potential density ρ is considered as a constant (=1035 kg m^{-3}) in subsequent analyses as it changes by less than 2% for the range of T and salinity in the KOE region,

although the model uses the nonlinear equation of state.

Integrating (4.2) from a fixed depth (h = *400 m*), a depth deeper than the winter mixed layer, to the surface yields

$$\frac{\partial}{\partial t}\int_{-h}^{0} T\,dz = \frac{Q_{rad}}{\rho c_p} - \int_{-h}^{0} \boldsymbol{u}\cdot\nabla T\,dz - \int_{-h}^{0} w\frac{\partial T}{\partial z}dz + \int_{-h}^{0}\frac{\partial}{\partial z}\left(\kappa\frac{\partial T}{\partial z}\right)dz, \quad (4.3)$$

where Q_{rad} is the radiative heat flux at the surface and the penetration of the short wave radiation below h is neglected. The 400 m depth for h has been chosen because it is sufficiently deep to cover the deepest winter mixed layers (100–200 m) and at the same time corresponds to the representative thermocline depth in the KOE region. In addition, it is well below the penetration depth of the short-wave radiation [*Hosoda et al.*, 2015]. Dividing by h and incorporating the surface turbulent flux $\left(\kappa\frac{\partial T}{\partial z}\right)_{z=0}$ from the last term of the right-hand-side (rhs) of (4.3) to the net surface heat flux, a tendency equation is obtained for the vertically averaged temperature of the upper 400 m water column, denoted by T400:

$$\frac{\partial T400}{\partial t} = \frac{Q_{net}}{\rho c_p h} - \frac{1}{h}\int_{-h}^{0} \boldsymbol{u}\cdot\nabla T\,dz - \frac{1}{h}\int_{-h}^{0} w\frac{\partial T}{\partial z}dz - \frac{1}{h}\left(\kappa\frac{\partial T}{\partial z}\right)_{z=-h}, \quad (4.4)$$

where Q_{net} is the net surface heat flux, sum of the surface radiative (Q_{rad}) and turbulent fluxes ($Q_{tur} = \rho c_p\left(\kappa\frac{\partial T}{\partial z}\right)_{z=0}$). The final form of the heat budget equation is expressed in flux form in unit of W m^{-2} by multiplying $\rho c_p h$,

$$\frac{\partial (HC)}{\partial t} \equiv \mathrm{HSR} = Q_{net} - \rho c_p \int_{-h}^{0} \boldsymbol{u}\cdot\nabla T\,dz - \rho c_p \int_{-h}^{0} w\frac{\partial T}{\partial z}dz, \quad (4.5)$$

where HC (=$\rho c_p h T400$) is the upper 400 m heat content, and by further neglecting the small vertical diffusion term at 400 m, $-\frac{1}{h}\left(\kappa\frac{\partial T}{\partial z}\right)_{z=-h}$. This equation (4.5) states that the heat storage rate (HSR) or the temporal variation of HC is the sum of the net surface heat flux Q_{net} and integrated horizontal heat advection HADV (second rhs term) and vertical heat advection VADV (third rhs term). Here, the total heat advection ADV (= HADV + VADV) is calculated from the TVD scheme, the same scheme used in the model, with the model's 3-dimensional temperature

and velocity fields. VADV is also separately calculated by one-dimensional centered scheme. HADV is then calculated by subtracting VADV from ADV. A positive (negative) Q_{net} means oceanic heat gain (release). Since only 3-day averaged fields of ORCA12 are available, the contributions of HADV and VADV with time scales shorter than 3 days are unresolved. These unresolved high-frequency heat advections together with horizontal and vertical diffusion terms are considered as a residual. All the heat budget terms are monthly averaged after calculating them with 3-day fields. It is noted that neglecting residual term affects little the major conclusion because the difference between HSR and the sum of Q_{net} and ADV is insignificant, as shown later. There is, however, one exception to this in August 2004 when there appears an abnormal feature in HADV due to the presence of erroneous horizontal velocities in the model outputs for unknown reasons. These erroneous data in August 2004 have been discarded when analyzing seasonal heat budget, interannual summertime (June-August) variability, and annual-mean HADV. However, it affects little interannual wintertime (December–February) variability that is the major interest.

To investigate the contribution of Ekman heat transport to the total horizontal heat advection, the zonal (H_x) and meridional (H_y) Ekman heat transports (EADV = $H_x + H_y$) are estimated in unit of W m^{-2} as

$$H_x = c_p \frac{\tau_y}{f} \frac{\partial T_m}{\partial x} \ , \ H_y = -c_p \frac{\tau_x}{f} \frac{\partial T_m}{\partial y} \ , \qquad (4.6)$$

where (τ_x, τ_y) is wind stress and f is the Coriolis parameter. Assuming that the horizontal heat advection (HADV) is sum of the Ekman heat advection (EADV) and geostrophic heat advection (GADV), the GADV is obtained by subtracting EADV from the HADV, i.e., GADV = HADV - EADV.

c. Difficulties to consider the mixed layer temperature budget

To consider the heat budget of mixed layer temperature (MLT), which is almost identical to the SST, the integrating depth h is now time-varying and shallower than 400 m. Because h is time-varying, the depth-integrated form of left-

hand-side of (4.2) should be written as:

$$\int_{-h}^{0} \frac{\partial T}{\partial t} dz = \frac{\partial}{\partial t} \int_{-h}^{0} T dz - T_{-h} \frac{\partial h}{\partial t} = \frac{\partial}{\partial t} (h T_m) - T_{-h} \frac{\partial h}{\partial t}$$

$$= h \frac{\partial T_m}{\partial t} + (T_m - T_{-h}) \frac{\partial h}{\partial t}, \quad (4.7)$$

where $T_m = \frac{1}{h} \int_{-h}^{0} T dz$ is MLT and T_{-h} is the temperature at z = -h. This indicates that the MLT tendency ($\frac{\partial T_m}{\partial t}$) is affected by the temporal change of MLD ($\frac{\partial h}{\partial t}$). *Kim et al.* [2006] suggested a rigorous approach to consider the heat budget due to MLD change in the z-level coordinate system. The entrainment term is calculated by the difference between the previous time step MLD temperature and mean temperature over a layer of present time step MLD (Figure 4.5). The entrainment and detrainment terms obtained by this method can be written as:

$$\alpha \frac{h_2}{h_1 - \alpha h_2} (T_1 - T_2) / \Delta t \,, \quad (4.8)$$

where T_1 and h_1 are previous time step MLT and MLD, respectively. h_2, which is always positive, is a difference of the MLD between the previous and present time steps. T_2 is vertical mean temperature in the previous time step over layer h_2. Δt is length of time step (3 days in this case). And α is a coefficient defined as

$$\alpha \equiv \begin{cases} -1 \text{ when water is entrained} \\ 0 \quad \text{when no change in depth} \\ 1 \quad \text{when water is detrained} \end{cases}.$$

By using continuity equation $\nabla \cdot \mathbf{u} + \frac{\partial w}{\partial z} = 0$, it can be shown that

$$\int_{-h}^{0}(\mathbf{u}\cdot\nabla T + w\frac{\partial T}{\partial z})dz = \int_{-h}^{0}\nabla\cdot(\mathbf{u}T)dz + \int_{-h}^{0}\frac{\partial(wT)}{\partial z}dz$$

$$= \nabla\cdot\int_{-h}^{0}(\mathbf{u}T)dz - T_{-h}\mathbf{u}_{-h}\cdot\nabla h - T_{-h}\,w_{-h} \qquad (4.9).$$

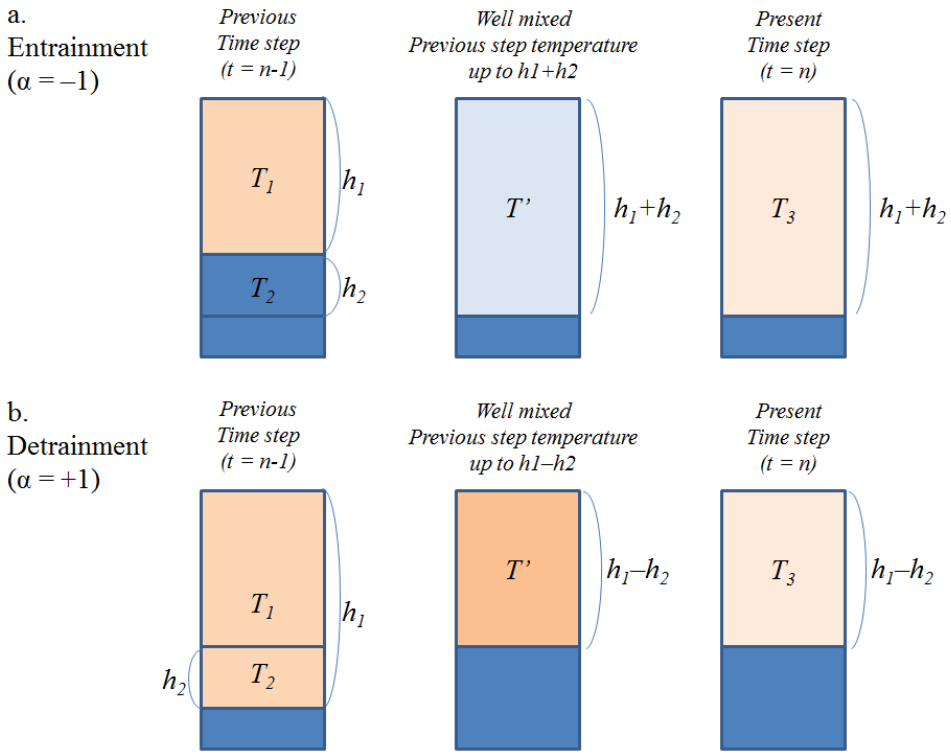

Figure 4.5. Schematics of calculation for (a) entrainment and (b) detrainment. T' is the temperature when the temperature profile of previous time step is well mixed up to present time step MLD. T_3 is the MLD temperature of present time step. See text for other variables.

It is also considered that temperature and horizontal velocity in the mixed layer as composed of their depth average (T_m, $\mathbf{u}_m$) and deviations (T', $\mathbf{u}_m'$), such as:

$$T = T_m + T' \text{ , with } T_m = \frac{1}{h}\int_{-h}^{0} T dz$$

$$\mathbf{u} = \mathbf{u_m} + \mathbf{u'_m} \text{ , with } \mathbf{u}_m = \frac{1}{h}\int_{-h}^{0} \mathbf{u} dz \quad (4.10).$$

Then, (4.9) can be written as:

$$\boldsymbol{\nabla} \cdot \int_{-h}^{0} (\mathbf{u_m} T_m) dz + \boldsymbol{\nabla} \cdot \int_{-h}^{0} (\mathbf{u}'T') dz - T_{-h}\mathbf{u}_{-h} \cdot \boldsymbol{\nabla} h - T_{-h} w_{-h}$$

$$= \boldsymbol{\nabla} \cdot (h\mathbf{u_m} T_m) + \boldsymbol{\nabla} \cdot \int_{-h}^{0} (\mathbf{u}'T') dz - T_{-h}\mathbf{u}_{-h} \cdot \boldsymbol{\nabla} h - T_{-h} w_{-h}$$

$$= T_m \boldsymbol{\nabla} \cdot (h\mathbf{u_m}) + h\mathbf{u_m} \cdot \boldsymbol{\nabla} T_m + \boldsymbol{\nabla} \cdot \int_{-h}^{0} (\mathbf{u}'T') dz - T_{-h}\mathbf{u}_{-h} \cdot \boldsymbol{\nabla} h - T_{-h} w_{-h} \quad (4.11).$$

By making use of (4.10) and continuity, the first term of (4.11) becomes:

$$T_m \boldsymbol{\nabla} \cdot (h\mathbf{u_m}) = T_m \boldsymbol{\nabla} \cdot \int_{-h}^{0} \mathbf{u} dz = T_m \int_{-h}^{0} \boldsymbol{\nabla} \cdot \mathbf{u} dz + T_m \mathbf{u}_{-h} \cdot \boldsymbol{\nabla} h$$

$$= -T_m \int_{-h}^{0} \frac{\partial w}{\partial z} dz + T_m \mathbf{u}_{-h} \cdot \boldsymbol{\nabla} h = T_m w_{-h} + T_m \mathbf{u}_{-h} \cdot \boldsymbol{\nabla} h \quad (4.12).$$

where it is assumed that the vertical velocity is zero at the surface.

Inserting (4.12) into (4.11), it is obtained that the following expression for the vertically integrated advection term within the mixed layer:

$$\int_{-h}^{0} \left(\mathbf{u} \cdot \boldsymbol{\nabla} T + w \frac{\partial T}{\partial z}\right) dz =$$
$$h\mathbf{u_m} \cdot \boldsymbol{\nabla} T_m + \boldsymbol{\nabla} \cdot \int_{-h}^{0} (\mathbf{u}'T') dz + (T_m - T_{-h})\mathbf{u}_{-h} \cdot \boldsymbol{\nabla} h + (T_m - T_{-h}) w_{-h} \quad (4.13).$$

Also considering penetration of shortwave radiation below the mixed layer, the final form of the MLT budget equation, which is obtained by integrating (4.2) using (4.9) and (4.13) with time-varying h, becomes that,

$$\frac{\partial T_m}{\partial t} =$$
$$\frac{Q_{net} - Q_z}{\rho h C_p} - \mathbf{u_m} \cdot \boldsymbol{\nabla} T_m - \frac{1}{h}\boldsymbol{\nabla} \cdot \left(\int_{-h}^{0} \mathbf{u}'T' dz\right) - \frac{1}{h}(T_m - T_{-h}) w_e - \frac{1}{h}\left(k_z \frac{\partial T}{\partial z}\right)_{z=-h} \quad (4.14)$$

where only the horizontal turbulent diffusion term is neglected. Different with 400 m case, the vertical diffusion term should be remained. This 'large' vertical diffusion can play an important role to transfer surface heat below the subsurface [*Hosoda et al.*, 2015]. w_e represents the entrainment velocity obtained by:

$$w_e = \frac{\partial h}{\partial t} + \mathbf{v}_{-h} \cdot \nabla h + w_{-h} \quad (4.15).$$

The term of time-varying MLD component of entrainment velocity ($\frac{\partial h}{\partial t}$) can be replaced with the method of *Kim et al.* [2006] shown in (4.8). Note that the time-varying MLD contribution of MLD heat budget (-0.1 ˚C/s in winter, -0.3 ˚C/s in summer) is almost half of the contribution of vertical diffusion (-0.1 ˚C/s in winter, -0.7 ˚C/s in summer). In the z-coordinate model data such as ORCA12, it is difficult to consider the second term which is the advection of MLD.

4.2.2 Mean and seasonal variation

a. Time averaged spatial distribution

Spatial distribution of record-length (1981–2013) mean heat budget terms averaged on a grid of 0.25°×0.25° is examined (Figure 4.6). The long-term mean annual HSR (Figure 4.6a) is nearly zero throughout the domain, indicating that the net surface heat flux (Q_{net}, Figure 4.6b) and the total heat advection ADV (HADV + VADV; Figure 4.6c) exactly counterbalance each other with a maximum magnitude of about ±200 W m^{-2} along the Kuroshio and KE. If ADV is divided into HADV and VADV, the two terms have similar magnitudes but opposite signs along the quasi-stationary meanders of KE (Figure 4.7). The energetic VADV along the KE appears to be due to vertical motions associated with the Kuroshio meander [*Sainz-Trapaga and Sugimoto*, 2000]. Although the contribution of VADV is not negligible in the energetic Kuroshio and KE region where nonlinear dynamics is expected to be important, ADV outside of these highly energetic regions is dominated primarily by HADV especially in the KOE region (compare different

panels in Figure 4.7). As the main focus is in the KOE region and in order to concentrate on the comparative analysis between two dominant forcing factors, Q_{net}-related atmospheric forcing and ADV-associated ocean dynamics, Q_{net} is mainly compared with ADV itself rather than splitting ADV into HADV and VADV.

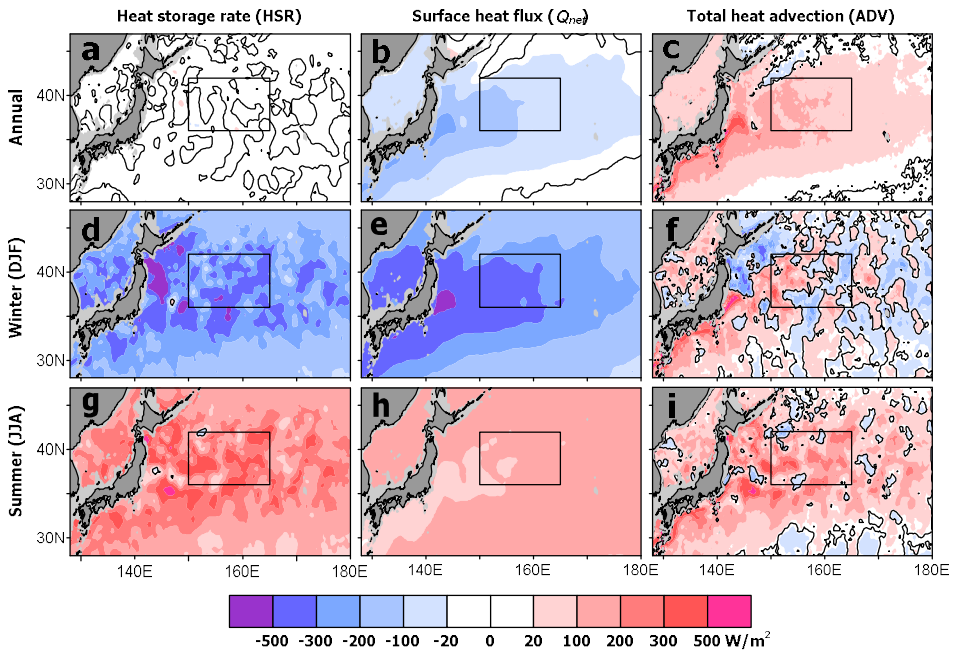

Figure 4.6. Spatial distribution of (a, d, g) heat storage rate (HSR), (b, e, h) net surface heat flux (Q_{net}), and (c, f, i) heat advection (ADV). (a–c) Annual mean, (d–f) winter mean, and (g–i) summer (June to August) mean.

The winter (December–February), when the Q_{net} release to the atmosphere is most vigorous, HSR is negative throughout the study area (Figure 4.6d), indicating that heat is systematically released from the ocean to the atmosphere with the greatest magnitude lying between 33°N and 42°N, a band comprising the KE, OE, and KOE region (KE–OE band hereafter). The overall large-scale pattern of HSR resembles Q_{net} (Figure 4.6e), while its small scale features are mostly due to ADV (Figure 4.6f). Negative ADV found along the east coast of Japan north of 35°N in winter (Figure 4.6f) is not observed during summer (June–August) when ADV

contributes positively to the heat budget in most parts of the domain (Figure 4.6i). The seasonal variation of ADV in the northeastern coastal region of Japan is mainly due to HADV (Figures 4.7d and 4.7g), because the seasonality of VADV is not apparent (Figures 4.7b, 4.7e, and 4.7h). This suggests that the negative ADV in the northeastern coast of Japan in winter (Figure 4.7f) is due to the cold water advection from the Oyashio, in agreement with *Tatebe and Yasuda* [2005]. It is interesting to note that the spatial distribution of the summertime Q_{net} (Figure 4.6h) nicely depicts the geographical location occupied by the Kuroshio/KE system, revealing a band of slightly lower Q_{net} compared to surrounding areas. This may indicate that warm Kuroshio waters tend to damp Q_{net} presumably due to enhanced upward turbulent fluxes caused by comparatively higher SST than surroundings, thus partly compensating dominant downward radiative heat fluxes.

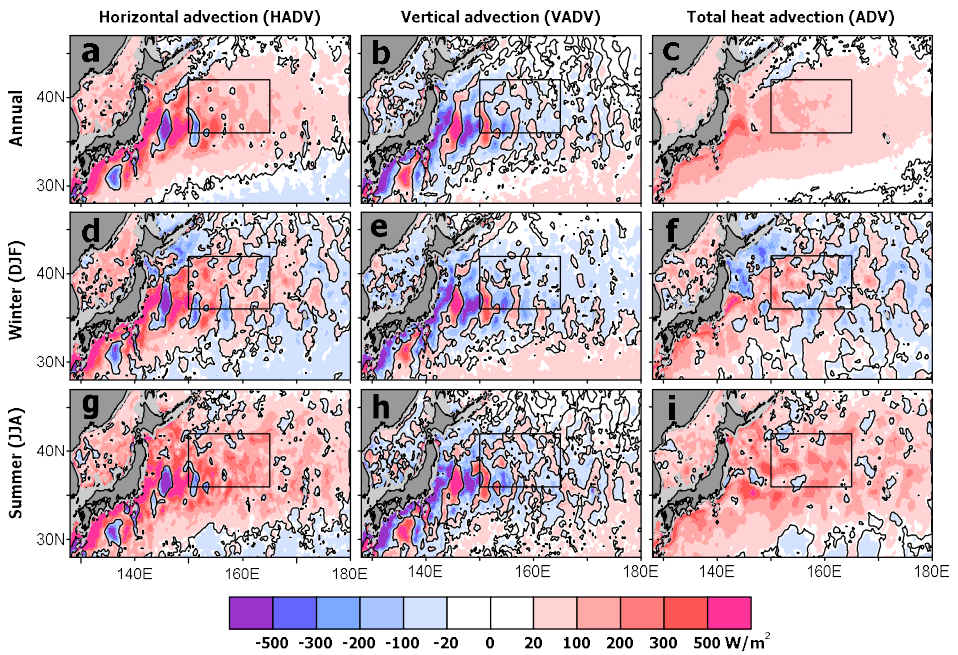

Figure 4.7. Spatial distribution of (a, d, g) horizontal (HADV) and (b, e, h) vertical (VADV) heat advection terms as well as (c, f, i) their sum (ADV). (a-c) Annual mean, (d-f) winter mean, and (g-i) summer mean.

b. Monthly climatologies

As Q_{net} varies over far larger spatial scales compared to ADV containing substantial meso scale variability (see Figure 4.6), all the heat budget components in subsequent analyses are spatially smoothed with a window size of 6°×4°, designed to suppress the mesoscale eddies, mean diameter of which is about 160 km (maximum diameter about 280 km) [*Cheng et al.*, 2014], unless otherwise stated. In Figure 4.8 the seasonal variations of the heat budget terms are displayed in time-latitude plots, where the monthly terms are zonally averaged between 150°E and 165°E over the longitudinal range of the KOE region. The seasonal cycle of all heat budget terms is most pronounced in the KE–OE band as in *Vivier et al.* [2002], although their study only covers regions south of 38°N. The seasonal cycle of HSR (Figure 4.8a) closely resembles the Q_{net} cycle, with nearly the same magnitude in winter (Figure 4.8b) because of the negligible contribution from ADV (Figure 4.8c). However, the contribution from ADV becomes increasingly important in summer, with its magnitude being comparable to or even exceeding Q_{net} (Figure 4.8c). In the KE–OE band (33°–42°N), HADV with positive heat transport forms a major contributor to ADV (Figure 4.8d). In contrast, VADV shows generally negative heat transport regardless of seasons except in September to November, and mostly counterbalances HADV during the cold season (January–March) (Figure 4.8e). The residual RES, which is the difference between the HSR and sum of ADV and Q_{net}, shows a minor influence with magnitude of only ±10 W m^{-2} at most (Figure 4.8f), indicating that the heat budget equation (4.4) is well closed by Q_{net} and ADV.

The area-averaged Q_{net} in the KOE region is strongly negative in cool seasons (October–March) with a peak close to -340 W m^{-2} in January, while it is positive during warmer seasons (May–September) with a peak at about 120 W m^{-2} in July, yielding a net heat loss of 90 W m^{-2} to the atmosphere on an annual average (Figure 4.8g). The latter value is comparable with those documented in previous works [*Qiu and Kelly*, 1993; *Moisan and Niiler*, 1998]. This net heat loss by Q_{net} is largely compensated by ADV, which is dominated by HADV. Note that lots of the seasonal variability of HADV is explained by EADV (Ekman heat transport),

where the contribution of GADV (geostrophic heat advection) is relatively small (Figure 4.9a). The area-averaged ADV in the KOE region contributes positively to HSR throughout the year with a maximum of about 150 W m^{-2} in September, but it is close to zero during the winter season. A plausible explanation for this minor contribution of wintertime ADV may be attributed to the enhanced cold advection by the southward flowing Oyashio and local Ekman transport, largely counterbalancing warm advection by the Kuroshio system. Indeed, considerable portion of seasonal variability of ADV is explained by the Ekman heat transport (Figure 4.9). Consequently, HSR, which is nearly equal to the sum of Q_{net} and ADV, shows strong seasonal variability, with its sign changing from negative to positive in April and from positive to negative in October, yielding a minimum T400 in April and a maximum T400 in October as shown in Figure 2.6b.

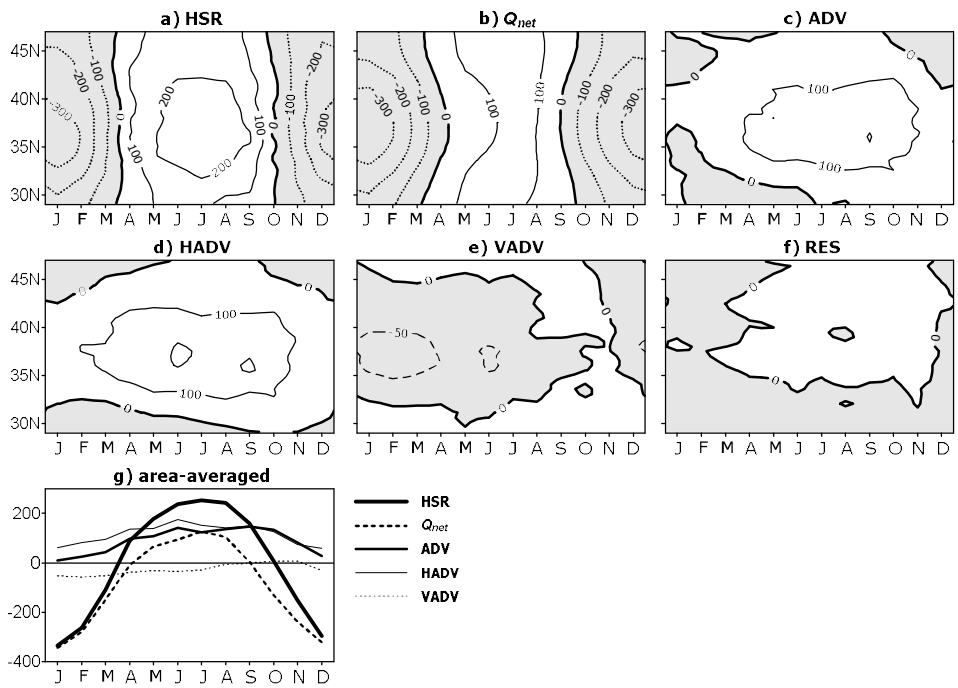

Figure 4.8. Zonal mean (150°-165°E) seasonal climatologies of (a) heat storage rate (HSR), (b) net heat surface flux (Q_{net}), (c) total heat advection (ADV), (d) horizontal heat advection (HADV), (e) vertical heat advection (VADV), and (f) residual (RES) over the western North Pacific between 28°N and 46°N. Model

outputs have previously been spatially smoothed with a 6°×4° window. Contour interval is 100 W m^{-2} and supplementary contour of -50 W m^{-2} is added in (e). Negative values are shaded. (g) Spatially-averaged monthly climatologies of heat budget components (in W m^{-2}) in the KOE region (150°–165°E, 36°–42°N).

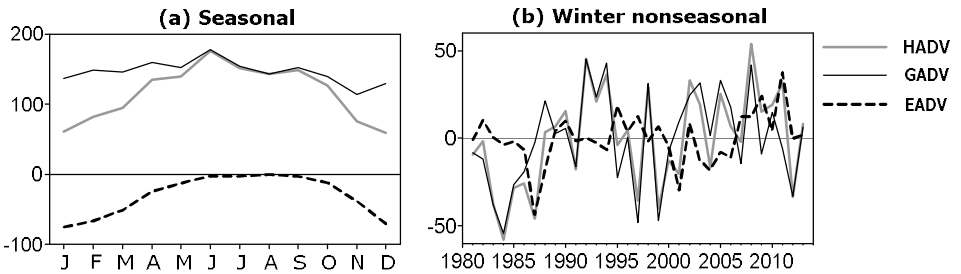

Figure 4.9. (a) Seasonal and (b) winter nonseasonal anomalies of horizontal heat advection (HADV, gray line), Geostrophic heat advection (GADV, black solid), and Ekman heat transport (EADV, dashed line). Unit is W m^{-2}.

4.2.3 Winter heat budget in the KOE region for two contrasting epochs

a. Nonseasonal variability of heat budget terms

Although main focus here is to investigate interannual-to-decadal variability of the winter upper-ocean temperature (heat content), the heat budget in terms of annual anomalies is first discussed since the decadal SST variability is influenced by the evolution of HSR during the entire year [*Tomita et al.*, 2002]. Annual mean non-seasonal anomalies of heat budget terms are obtained by removing their monthly climatology and averaging from January of the present year to the following January. Latitude-year maps of zonally averaged (150°–165°E) anomalies of heat budget terms are shown in Figure 4.10. Each term is computed from spatially smoothed (window size of 6°×4°) fields and the erroneous data of year 2004 are discarded for the reason previously mentioned. Non-seasonal anomalies of Q_{net} and ADV in the KOE region before 1990 are comparable in

magnitude, especially between 38°N and 44°N within and slightly north of the KOE region. However, ADV anomalies afterward are much larger compared to Q_{net} anomalies and well correlated with HSR anomalies (Figures 4.10a–c). Q_{net} anomalies north of 36°N corresponding to the model KE shows an opposite tendency of temporal variability compared to those south of 36°N. This is one of the reasons why the KOE region is limited to the north of 36°N excluding the Kuroshio recirculation region south of 36°N. The ADV variability is dominated by HADV (Figure 4.10d), whereas VADV (Figure 4.10e) shows significantly weaker variability at all latitudes considered, with mostly an opposite sign to HADV. Note that the Ekman heat transport has insignificant contribution to the HADV in the interannual to decadal time scale in this region (Figure 4.9b), consistent with *Kwon and Deser* [2007]. The residual RES (Figure 4.10f) is negligible compared to HSR and ADV especially in the KOE region, indicating that the heat budget balance equation (4.4) is reasonably well closed for non-seasonal variations.

Time series of area-averaged annual and winter anomalies of HSR, Q_{net}, and ADV in the KOE region show that the interannual variability of HSR can be mostly explained by ADV during the entire study period (Figures 4.11a and 4.11b), consistent with previous studies [*Vivier et al.*, 2002; *Kwon and Deser*, 2007]. Compared to the ADV variability, Q_{net} shows a significant decreasing trend, which makes the interdecadal change prominent rather than interannual variations. In fact, the Q_{net} variation is characterized by large positive anomalies (+35 W m^{-2}) during the 1980s and weakly negative anomalies (-10 W m^{-2}) until 2008. This interdecadal difference (45 W m^{-2}) dominates over the relatively weaker interannual signals (17 W m^{-2} in standard deviation). Since 2008, Q_{net} decreases continuously until the end of the analysis period, indicative of enhanced oceanic heat transfer to the atmosphere in recent years. When Q_{net} has large positive anomalies at the end of the 1980s, the relationship between HSR and ADV is noticeably weaker especially in the winter during the 1980s, as compared to that after 1991 when the two heat budget terms are tightly correlated (Figures 4.11a and 4.11b).

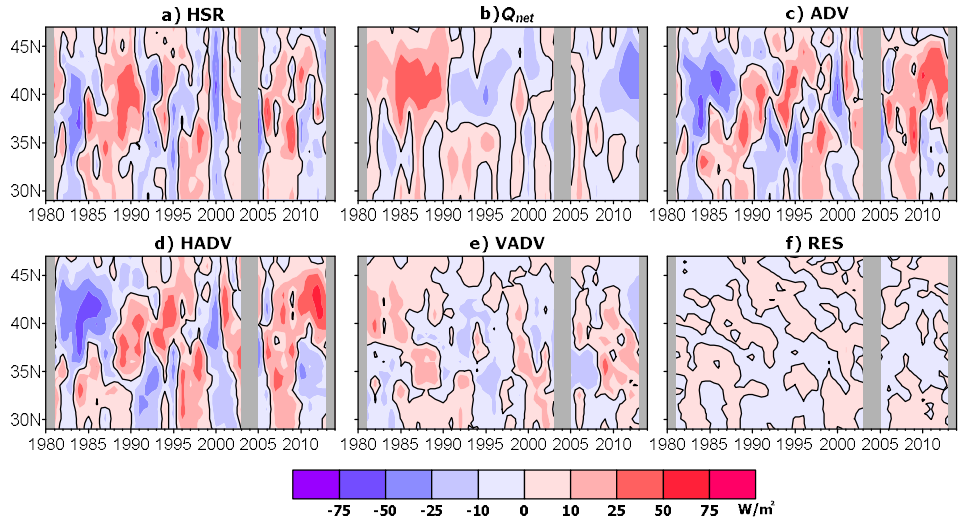

Figure 4.10. Zonal mean (150°–165°E) annual anomalies of (a) heat storage rate (HSR), (b) net surface heat flux (Q_{net}), (c) total heat advection (ADV), (d) horizontal heat advection (HADV), (e) vertical heat advection (VADV), and (f) residual (RES) over the western North Pacific between 28°N and 46°N.

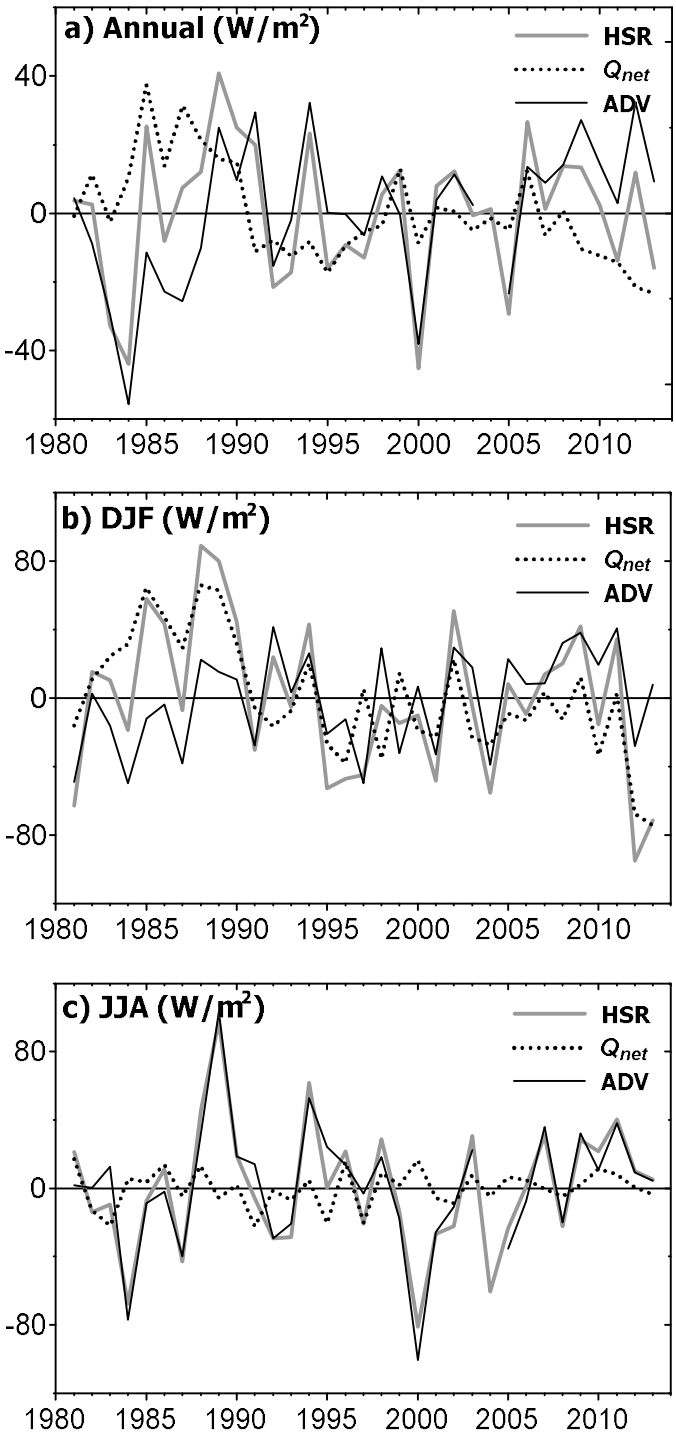

Figure 4.11. KOE region-averaged anomalies of HSR (thick solid lines), Q_{net} (dotted lines), and ADV (thin solid lines). (a) Annual mean, (b) winter (DJF) mean, and (c) summer (JJA) mean.

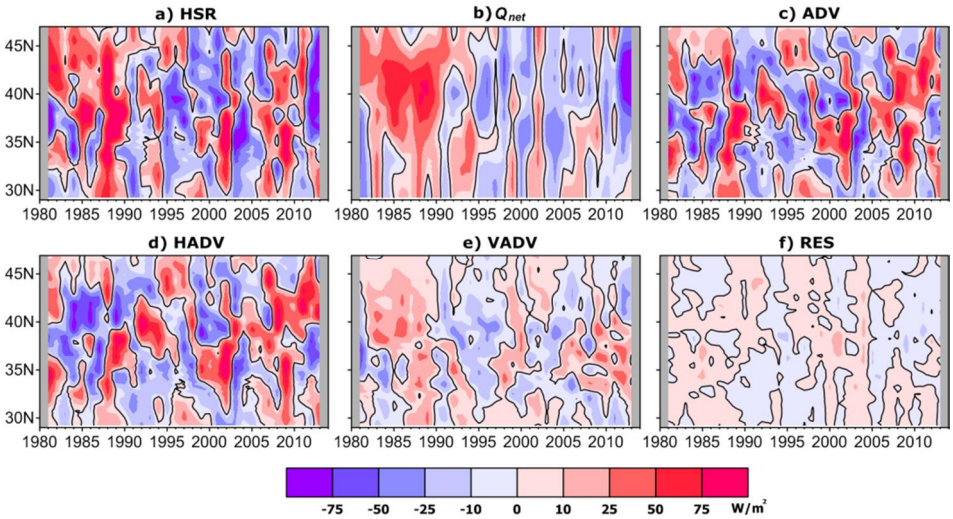

Figure 4.12. Same with Figure 4.10, but winter anomalies.

Figure 4.12 shows latitude-year maps of zonally averaged winter anomalies of heat budget terms. The variability of each budget term is much stronger than that of annual anomalies (Figure 4.10). This is consistent with *Mochizuki and Kida* [2006] who showed that the seasonal temperature tendency which is mainly controlled by Ekman heat advection is enhanced (decayed) during winter (summer). Interannual distribution of winter Q_{net} (Figure 4.12b) is very similar with that of annual anomalies (Figure 4.10b). However, the winter and annual averaged ADV shows somewhat different temporal and spatial variability (Figure 4.10c and Figure 4.12c), indicating that it is difficult to understand the temperature variability in the KOE region only with the winter ADV anomalies.

b. Epoch-dependent contrasting variability of the heat budget terms

Based on the observation above of different contributions of Q_{net} and ADV to HSR variations, the analysis period had been divided into three contrasting epochs: 1981–1990, 1991–2008, and 2008–2013. 9-yr moving standard deviations of Q_{net} and ADV (Figure 4.13) shows consistent result with those three periods. Before

early-1990s and after 2008, standard deviation of KOE Q_{net} is higher than that of ADV. On the other hand, the KOE Q_{net} variability becomes weaker than that of ADV. The temporal variability of ADV is not much sensitive to the epochs. The first two periods, which are considered here as the two contrasting epochs, correspond to two different climate regimes described in *Park et al.* [2012], *Pak et al.* [2014], and Chapter 3 in the thesis, although the regime shift from the SM-HC (1973-1987) to the WM-LC (1988-2002) occurs 3 years earlier than the shift described here (1990/91). This epoch-dependent difference in the relative contribution of forcing factors is observed only in winter and annual mean anomalies (Figures 4.11a and 4.11b), while summer anomalies show the predominance of ADV over the entire analysis period (Figure 4.11c). This indicates that the epoch-dependent contrasting variability is most apparent in the winter season when the air-sea turbulent heat flux is most vigorous and the surface mixed layer is deepest. Note that similar interannual to decadal variability of the KOE Q_{net} is also observed from other data sets such as OAFlux [*Yu et al.*, 2008] and NCEP reanalysis 1 [*Kalnay et al.*, 1996] (Figure 4.14).

The temporal standard deviations of Q_{net} and ADV in the KOE region are 48.0 W m^{-2} and 27.7 W m^{-2}, respectively, during E1 period (1981–1990) suggesting that relatively stronger influence of Q_{net} to HSR compared to that of ADV. On the other hand, during E2 period (1991–2008), the standard deviations of KOE Q_{net} and ADV are 19.4 W m^{-2} and 27.4 W m^{-2}, respectively. Similar result is obtained from the spatial distribution of the temporal standard deviation of both Q_{net} and ADV (Figure 4.15). Although ADV is most variable in the KE-OE band, its variability is nearly insensitive to the epochs (Figures 4.15c and 4.15d), consistent with Figure 4.3. However, the Q_{net} variability greatly depends on the epoch (Figures 4.15a and 4.15b). This change of standard deviations of two heat budget terms is consistent with the observation mentioned above. The relationship between HSR and Q_{net} is stronger during E1 period while HSR and ADV are tightly correlated to each other during E2 period. Detail discussion of the epoch-dependent contribution of each heat budget term will be given in section 4.3.3.

These ORCA12 model-derived results are consistent with *Park et al.* [2012] which evidenced from observational data the importance of ocean dynamics in determining the winter KOE SST and its increasingly important role during the

weak EAWM period (1990–2005) compared to the strong EAWM period (1970–1989). Chapter 3 in this thesis and *Pak et al.* [2014] show a regime-dependent nonstationary impact of the atmospheric circulation represented by the EAWM and NPO on the winter SST in the western North Pacific. They showed that during the strong EAWM regime (1973–1987), which matches well with the E1 period, both atmospheric indices are well correlated with the late winter SST in the western North Pacific with a lag of one month, while the correlation significantly decreases during the weak EAWM regime (1988–2002), a period also close to the E2 period. However, a closer look at the KOE region reveals that the winter KOE SST variability is not sufficiently explained by EAWM and NPO indices (see Figure 3.10) in both strong and weak EAWM epochs.

Although the contribution to HSR of both ADV and Q_{net} changes with the epochs, the monsoon intensity cannot be directly ascribed to the main contributor to the SST variability (HSR), at least in the KOE region. The winter Q_{net} anomalies show positive values in the E1 period (Figure 4.11b) indicating counter-intuitively less wintertime heat loss to atmosphere during the strong EAWM period. Further discussion is given in later section (4.3.2).

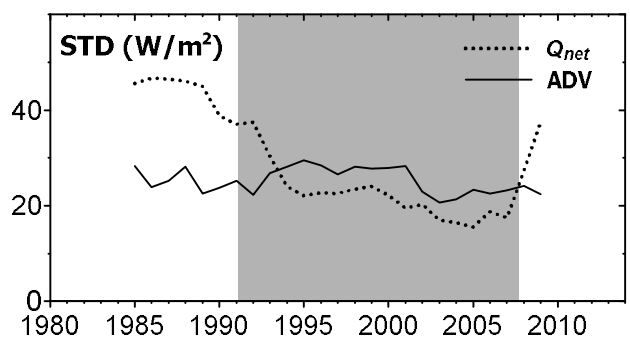

Figure 4.13. 9-yr moving temporal standard deviation of DJF Q_{net} (dotted) and ADV (solid) in the KOE region. Time axis corresponds to the center of the moving window (the value at 1990 indicates standard deviation during 1986-1994). The gray area corresponds to the E2 period (1991 to 2008) when the variability of Q_{net} is smaller than that of ADV.

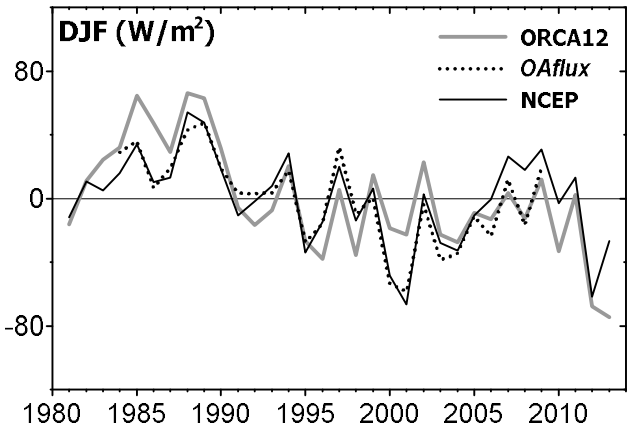

Figure 4.14. Temporal evolution of DJF Q_{net} in the KOE region from various datasets; ORCA12 (gray), OAflux (dotted), and NCEP reanalysis 1 (solid black).

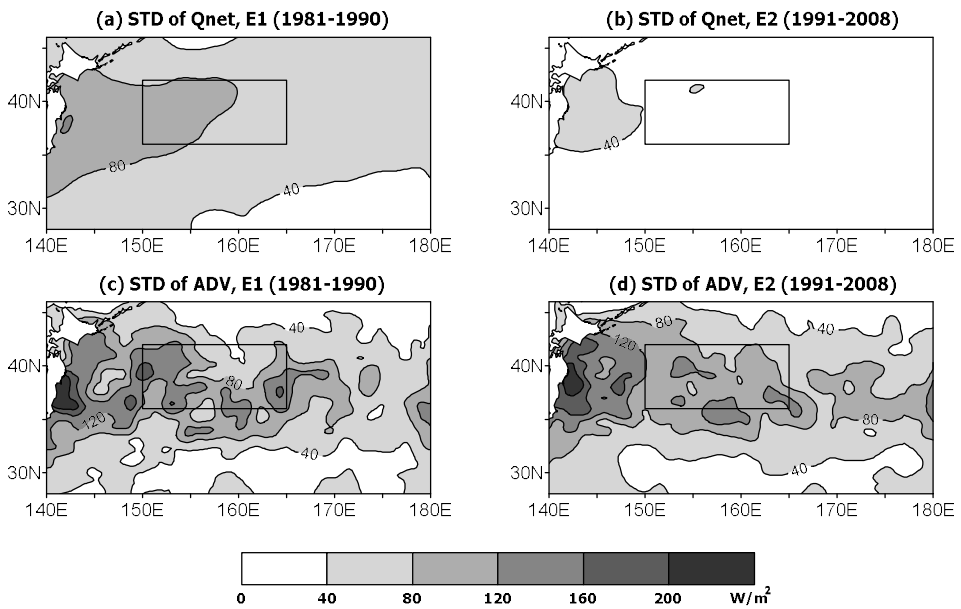

Figure 4.15. Spatial distribution of temporal standard deviation of (a-b) Q_{net} and (c-d) ADV during (a, c) E1 period and (b, d) E2 period. Unit is W m^{-2}.

The above features can also be quantified using the skill score [*Murphy*, 1988], a metrics originally used in weather forecasting to measure the improvement obtained by a particular forecast model compared to a reference forecast, which is usually a climatology. The skill score (*ss*) between the predictor (*x*) and predictand (target, *y*) is defined as:

$$ss(x,y) = 1 - \frac{MSD(x,y)}{MSD(\bar{y},y)} \quad (4.16),$$

where MSD is the mean square difference between the two parameters and the overbar denotes a temporal mean. *Murphy* [1988] also decomposed the skill score into three terms as follows:

$$ss(x,y) = r^2(x,y) - \left[r(x,y) - \frac{S(x)}{S(y)}\right]^2 - \left[\frac{\bar{x}-\bar{y}}{S(y)}\right]^2 \quad (4.17),$$

where *r* indicates the correlation coefficient between predictor and predictand, and *S* is the standard deviation. The three terms on the rhs of equation (4.17) are denoted A, B, and C, respectively. The term A is the squared correlation coefficient from non-detrended time series, while B is related to the slope (*a*) of the regression line between predictor and predictand ($y = ax + b$). Finally, C represents the difference between the mean predictor and predictand. So, the skill score is upper-bounded by term A which has a maximum value of 1, while terms B and C act as penalties which contribute to decrease *ss*, theoretically down to minus infinity.

Table 4.1 shows the skill score, between predictand (HSR) and predictors (Q_{net} and ADV) in winter for the different epochs, as well as the detail of terms A, B, and C. The record-length correlation between the HSR and ADV is rather smaller (r^2 = 0.39) than that between HSR and Q_{net} (r^2 = 0.65), in contrast to previous studies [Viviet et al., 2002; Kwon et al. 2007] showing horizontal heat advection is important for the interannual to decadal variability of heat storage rate. Due to the difference between correlation (A) and slope penalty (B), *ss* between Q_{net} and HSR is better (0.41) than that between ADV and HSR (-0.51). Note that the squared correlation is not much different if detrended. During E1 period, the squared

correlation of Q_{net} and ADV with HSR are almost same (r^2 = 0.80) and the slope penalty of them are also similar (-0.83 and -0.80, respectively). However, ADV has more mean value penalty (C) as expected from Figure 4.11b, so that Q_{net} shows better skill score compared to ADV during E1 period, consistent with the above observation that Q_{net} has more contribution to the HSR due to the temporal variability is higher than that of ADV. On the other hand, during E2 period, the skill score of ADV is higher (and even it is positive) than that of Q_{net} due to higher correlation coefficient (A) and smaller slope penalty (B). This is also consistent with the above observation that ADV has more contribution to HSR during this period. In short, the skill score also suggests that the epoch-dependent influence to the HSR of the atmospheric forcing (represented by heat flux, Q_{net}) and ocean dynamics (represented by heat advection, ADV), also consistent with *Pak et al.* [2014] who showed a nonstationary impact of the atmospheric circulation represented by EAWM and NPO to the winter SST. They showed that during the strong EAWM regime (1973-1987) matching well with the E1 period (1981-1990), both atmospheric indices are well correlated to the SST with a lag of a month in the western North Pacific (not exactly KOE region), indicating stronger influence of the atmospheric circulation to the ocean temperature, while their correlation is decreased after weak EAWM regime (1988-2002), a period matching with E2 period (1991-2008).

Table 4.1. Skill scores as well as the detail decomposed terms (A, B, and C) for winter mean heat budget components during different periods in the KOE box (150°-165°E, 36°-42°N). The predictand is fixed to the HSR and the predictors are Q and ADV. Term A is the squared correlation coefficient, B is the slope penalty, and C is mean difference penalty. See text for details.

	Skill		A		B		C	
	Q_{net}	ADV	Q_{net}	ADV	Q_{net}	ADV	Q_{net}	ADV
1981-1990 (E1)	-0.20	-2.18	0.80	0.80	-0.83	-0.80	-0.17	-2.18
1991-2008 (E2)	-1.16	0.50	0.34	0.72	-1.49	-0.09	-0.01	-0.13
1981-2013 (All)	0.41	-0.51	0.65	0.39	-0.24	-0.90	0.00	0.00

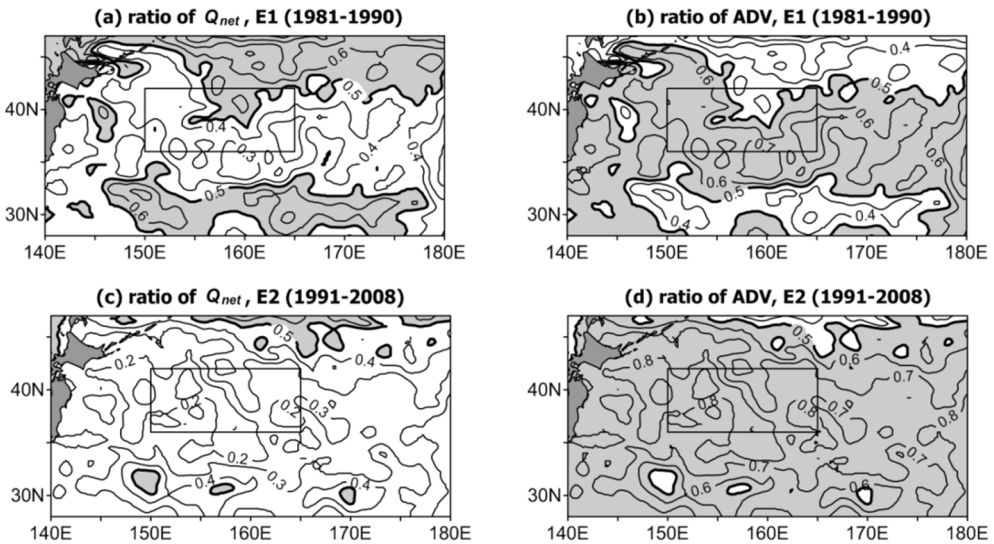

Figure 4.16. Relative contribution ratios of (a, c) Q_{net}, $a/a+b$, and (b, d) ADV, $b/a+b$, to the KOE winter HSR based on the regression HSR = aQ_{net} + bADV, under the condition of $a + b = 1$. See the text for more details. (a-b) E1 period (1984-1990) and (c-d) E2 period (1991-2008). Areas with the ratios exceeding 0.5 are shaded.

The spatial distribution of multivariate linear regression coefficients of Q_{net} and ADV onto winter HSR for two contrasting periods of E1 (1984–1990) and E2 (1991–2008), shown in Figure 4.16, also suggests the changes of contribution. The multivariate regression analysis [e.g., *Emery and Thomson*, 1997] can be modeled in this case as $Z = aX + bY + \varepsilon$, where Z, X, and Y represents symbolically the normalized anomalies of HSR, Q_{net}, and ADV at each grid point, respectively, following *Park et al.* [2012]. The regression coefficients, a and b, which can be determined by minimizing the square error ε^2 with a least square approach, represent the relative contribution of Q_{net} and ADV to HSR, respectively. Note that the regression coefficients are obtained under the constraint of $a + b = 1$ [*Park et al.*, 2012], so that the coefficient value of 0.5 is the criterion above which one of the two heat budget terms (Q_{net} and ADV) is considered as the dominant contributor to HSR.

Consistent with previous results [*Kwon and Deser*, 2007; *Park et al.*, 2012], the contribution of ADV is dominant in the KE–OE band (33°–42°N) regardless of the epochs. Indeed, the dominance of ADV is more pronounced and wide spread over the whole study area during E2 (Figure 4.16d), while during E1, the area of weaker but still dominant ADV considerably shrinks and is confined within the KE–OE band (Figure 4.16b). In contrast, Q_{net} during E1 is dominant in regions north and south of the KE–OE band (Figure 4.16a). During E2, however, Q_{net} becomes a minor contributor over the study area (Figure 4.16c). The area-averaged contribution ratio between Q_{net} and ADV in the KOE region is approximately 4:6 (see inserted boxes of Figure 4.16) during the E1 period, while it becomes 2:8 during the E2 period. Note that the result is not consistent with above results using time series of area averaged Q_{net} and ADV. The difference may come from the relatively (spatially) small-scale ADV compared to Q_{net}, although both Q_{net} and ADV are applied the spatial window filters. Because the KOE region is much larger than the window size, the time series of area-averaged Q_{net} and ADV has been much more smoothed, so that the variability of ADV is much suppressed and ADV has similar or less impact on the HSR in the above analyses based on the area-averaged time series. However, in the regression map, ADV is not filtered much as in KOE average, so ADV can dominate regardless of the epochs. So the approximate ratio of Q_{net} and ADV may dependent on the size of spatial filter. However, this scale difference is not affect the main results that the influence of Q_{net} (ADV) is relatively higher than that during E1 (E2) period.

4.3. Possible mechanisms for interannual to decadal variability in winter KOE temperature

The above results indicate that the upper-ocean thermal anomalies in the KOE region are damped by a negative feedback of air-sea heat flux. Here, the possible mechanisms for generating interannual to decadal thermal variabilities in the KOE region are investigated in association with ocean dynamics and their causes.

4.3.1 Upper ocean thermal variability due to the meridional shift of oceanic fronts

a. Oceanic fronts and KOE T400 variability

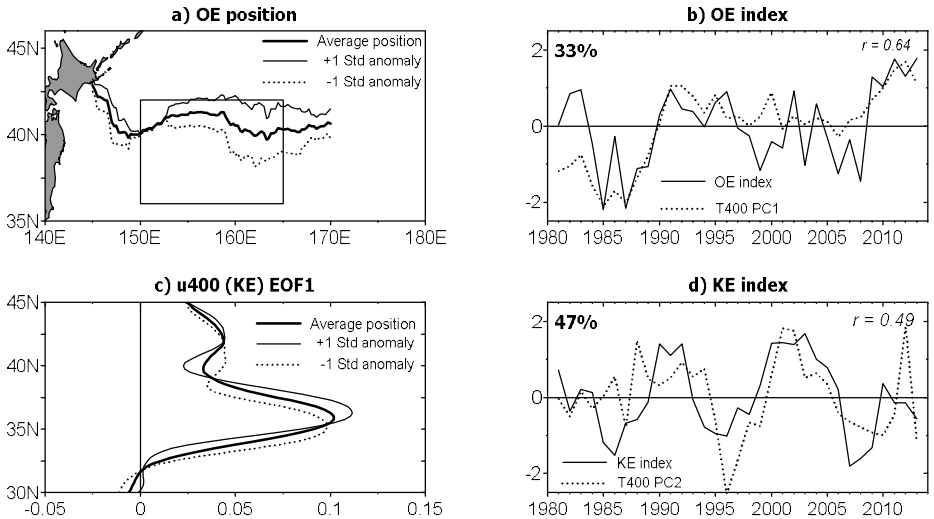

Figure 4.17. First EOFs (left panels) and corresponding PC time series (right panels) of (a–b) the latitudes of maximum meridional SST gradient representing the OE and (c–d) the zonal mean (145°–170°E) zonal velocity averaged from the surface to the 400 m (u400) representing the KE. The mean position of OE is shown with a thick solid line in (a) together with their ±1 standard deviations with thin solid and dotted lines. The T400 PC1 from Figure 4.1b (dotted line) is overlaid in (b). The mean position of KE is shown with thick solid line in (c) together with their ±1 standard deviations with thin solid and dotted lines. The T400 PC2 from Figure 4.1d (dotted line) is overlaid in (d).

The meridional shifts of the OE and KE are investigated in association with the T400 variability shown in Figure 4.1, since it has been suggested that the OE and KE variations have an important role in the interannual-to-decadal SST variability in the KOE region [*Taguchi et al*., 2007; *Nonaka et al*., 2008]. The OE index is defined following *Frankignoul et al.* [2011] as the PC1 of the latitudes of maximum meridional gradient of winter SST for the longitudes between 145°E and 170°E. The EOF1 explains 33 % of the total variance and shows a meridional shift

up to 2° in latitude especially to the east of 152°E (Figure 4.17a). The overall position of the model-derived OE front (thick line) matches well the observations-derived OE front of *Frankignoul et al.* [2011]. The OE index derived here is well correlated (r = 0.64) with the PC1 of T400 (Figure 4.17b), which is also true with the area averaged T400 in the KOE region (r = 0.62), suggesting that the KOE region thermal variability (and EOF1 of T400 over the western North Pacific) is primarily associated with the meridional shift of the OE front. This significantly high positive correlation between the OE index and KOE T400 means that warm (cold) anomalies tend to appear when the OE shifts northward (southward), in agreement with *Frankignoul et al.* [2011].

To investigate the influence of the KE on the KOE thermal variability, an EOF analysis was performed on the zonal-mean zonal velocity averaged from the surface to the 400 m (u400 hereafter) over the entire latitudes of the study area, following a similar approach as *Taguchi et al.* [2007]. The EOF1 of u400 (Figure 4.17c) explains 47 % of the total variance and the average position of the maximum u400 is located at 36°N, with a plus and minus one standard deviation locating at about 1° north and south of the mean latitude. As the EOF1 of u400 represents the meridional shift of the KE, the corresponding PC1 (Figure 4.17d) is defined as the KE index. In addition to this meridional shift, the KE index is also associated with a strength change in u400, with a northward (southward) shift corresponding to a strengthening (weakening) of the KE jet. This is consistent with results of *Qiu and Chen* [2005] based on observational data, but differs from *Taguchi et al.* [2007] who claimed, based on results from an eddy-resolving OGCM, the existence of two independent EOF modes of the KE variability: a meridional mode versus a strength mode. The KE index is insignificantly correlated (r = 0.35) with the T400 PC1, but it is relatively well correlated (r = 0.49) with the T400 PC2 (Figure 4.17d), suggesting that the second mode temperature variability in the western North Pacific is associated with the meridional shift of KE. Therefore, meridional shift of KE is insignificantly related with the KOE T400, which is well related to T400 PC1.

The WP and PNA are the two major winter atmospheric circulation patterns in the North Pacific [*Wallace and Gutzler*, 1981]. The sea level pressure expressions of these mid-tropospheric stationary circulation patterns are the NPO and AL

(Aleutian low intensity, see Chapters 2 and 3), respectively. According to *Pak et al.* [2014], the PNA and AL are well correlated to each other (r = 0.92) regardless of epochs, and so as in the relationship between WP and NPO (r = 0.80).

The linkage between atmospheric circulation patterns and wind stress curl in the North Pacific has been documented. *Ishi and Hanawa* [2005] showed that the correlation maps of wind stress curl in the North Pacific with PNA and AL indices are similar and resemble the spatial pattern of the 1st mode variability of wind stress curl. They also showed the linkage between 2nd mode of wind stress curl and WP. The regression map of wind stress curl anomaly to PC2 of SLP in the North Pacific [*Ceballos et al.*, 2009], one of the definitions of the NPO index [*Linkin and Nigam*, 2008], shows a dipole pattern similar to the spatial pattern of 2nd mode variability of wind stress curl. These studies suggest that the major atmospheric climate indices defined with upper-level atmosphere circulations, WP and PNA, represent the surface wind stress curl forcing in the North Pacific.

The OE index is significantly correlated with both the WP and PNA indices but with different lags between zero and 4 years (Table 4.2). At zero lag, it is significantly correlated with the WP (r = -0.41) but not with the PNA (r = -0.20). Maximum (and significant) correlation between PNA and OE index is found when PNA leads OE by 2 months (M2 in Table 4.2). This is consistent with the results of *Nonaka et al.* [2008] and *Frankignoul et al.* [2011], which attributed the meridional shift of the OE to the rapid barotropic response to the AL mode, surface expression of the PNA. In addition to the significant correlation with the WP and PNA at nearly zero-year lag, the OE index reveals a significantly lagged response to both the WP (r = 0.51 at lag 3 yr and r = 0.38 at lag 4yr) and PNA (r = -0.37 at lag 2 yr), which can be explained by the slow response to wind stress curl anomalies and baroclinic Rossby wave adjustment [*Nonaka et al.*, 2008; *Frankignoul et al.*, 2011]. On the other hand, the KE index has no significant correlations with both the WP and PNA indices at any lag (Table 4.2).

Table 4.2. Lag correlations between the two oceanic fronts (OE and KE) and lagged atmospheric circulation patterns (WP and PNA). The non-zero lag indicates the number of years lead by the atmospheric forcing. The lags M1 and M2 indicate the lag in month (M1 indicates NDJ average for WP and PNA, 1 month leading compared to DJF OEI and KEI). Significant correlations at the 95% confidence level are marked in boldface.

Indices	OE index		KE index	
Lag	WP	PNA	WP	PNA
0	**-0.41**	-0.20	-0.14	0.12
M1	-0.20	-0.35	-0.13	0.22
M2	-0.00	**-0.42**	-0.03	0.15
1	-0.18	-0.30	0.10	-0.13
2	-0.03	**-0.37**	0.30	-0.08
3	**0.51**	-0.12	0.23	0.06
4	**0.38**	-0.20	0.12	0.11

b. Oceanic fronts and T400 in the western North Pacific

The relationship between meridional shifts of oceanic fronts and T400 in the western North Pacific is investigated (Figure 4.18). As expected from the 1st EOF of T400 and OE index, which is well correlated with PC1 of T400, the correlation between OE index and T400 north of 35°N generally shows significant correlation (Figure 4.18a), especially more than 0.5 along 40°N close to the latitudinal position of OE. The meridional shift of OE explains somewhat portions of the winter T400 variability north of KE. On the other hand, the significant correlation between KE index and T400 is only located along the KE (Figure 4.18b). This is consistent with *Sugimoto and Hanawa* [2011] who showed that the meridional shift of KE cannot explain the interannual to decadal variability of the SST in the KOE region, where is similar but shifted westward (close to land) compared to the region in this thesis. Note that *Sugimoto and Hanawa* [2011] showed that the SST variability in the KOE region (close to land) is rather better explained by eddy activity detached from the KE. In short, OE index should be considered if the region north of KE is focused, while KE index is more important for the region just along the KE.

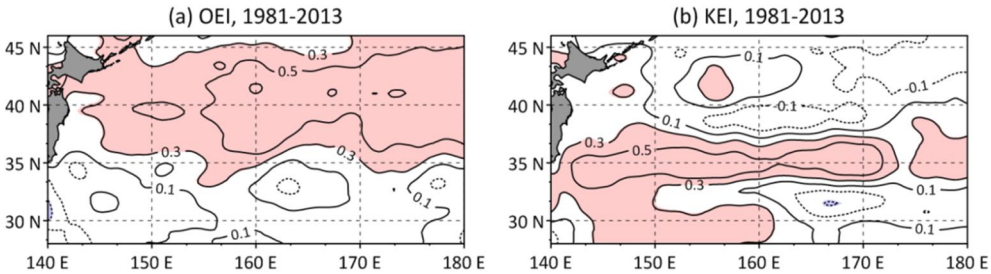

Figure 4.18. Spatial distribution of correlation coefficients of T400 with (a) OE index and (b) KE index. Significant correlation at 95% confidence level is shaded.

c. Oceanic fronts and Sverdrup stream function

The EOF analysis of the two-metrics representing the OE and KE variations shows that the internannual to decadal upper-layer winter thermal variability in the KOE region is mainly controlled by the meridional shift of the OE front and secondly by that of the KE front. As the meridional shifts of the OE and KE are expected to be associated with the wind-driven inter-gyre boundary shifts [e.g., *Sugimoto and Hanawa*, 2009], the Sverdrup stream function (SSF) is computed to identify the inter-gyre boundary having zero SSF and to establish its relationship with the OE and KE indices. The SSF φ is calculated by integrating the wind stress curl from the east coast (x_E) of the North Pacific as:

$$\varphi = \frac{1}{\beta \rho_0} \int_{x_E}^{x} (\hat{k} \cdot \nabla \times \frac{\boldsymbol{\tau}}{f}) dx \qquad (4.20)$$

where β is the meridional gradient of the Coriolis parameter f, ρ_0 is a reference sea-water density set to 1035 kg m^{-3}, $\boldsymbol{\tau}$ is the wind stress vector. The ERA-interim $\boldsymbol{\tau}$ data (used in ORCA12) is used to obtain the winter-mean SSF fields in the North Pacific.

Figures 4.19a and 4.19b show the EOF1 and PC1 of the SSF zero line from 145°E to 170°E (SSF-zero index hereafter), which explains 98% of the total variance. It represents the meridional shift of the winter inter-gyre boundary of Sverdrup transport stream function in the western North Pacific. The average position of the winter SSF-zero index is found at 37.5°N, which is located about 3

to 4 degrees south of the OE front (compare Figures 4.11a and 4.19a) but is rather much closer to the KE front (36°N). Although there is no simultaneous relationship between them, the SSF-zero index and OE index become significantly correlated with each other (r = 0.45) if the SSF-zero index leads the OE index by 3 years. A similar 3-yr lagged correlation (r = 0.52) is observed between the T400 PC1 (Figure 4.19b) and the SSF-zero index. This 3-year lag is consistent with the canonical time scale of the first baroclinic Rossby wave propagating from the central North Pacific to the KOE region [*Qiu*, 2003; *Nonaka et al.*, 2008; *Park et al.*, 2012]. Also, the SSF-zero index has the best correlation (r = 0.41) with the KE index when the SSF-zero index leads by 2 years, but insignificant correlation (r = 0.31) is found at lag 3 yr. However, no significant correlation is observed between the SSF-zero index and T400 PC2 for any lag between zero and 4 years. This is somewhat intriguing in view of a significant lagged correlation between the SSF-zero index and the KE index as well as between the KE index and the T400 PC2, as already mentioned. In conclusion, there appears a moderate lagged correlation of the OE and KE to the SSF-zero index, explaining mostly less than 20% of their total variance. More fundamental atmospheric forcing indices seem necessary to better describe the KOE thermal variability.

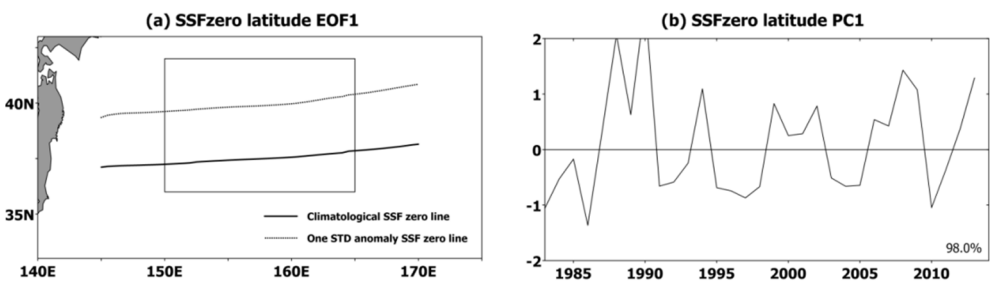

Figure 4.19. The first EOFs (left panel) and corresponding PC time series (right panel) of the latitude of the zero Sverdrup stream function (SSF-zero). Mean position of SSF-zero is shown with thick solid lines in (a) together with its standard deviations with dotted line. The standard deviations correspond to the positions when PC is +1 for the record-length winter period in the ORCA12.

d. Atmospheric forcing and T400 in the western North Pacific

While the OE and KE are significantly correlated with T400, they explain a limited fraction of the total T400 variance: the OE (KE) explains only 46% (34%) of T400 PC1 (PC2) which explains 54% (12%) of the total variance of T400, so that only 25% (4%) of the total variance of T400 is explained by OE (KE). In addition, their (OE and KE) correlations with the WP and PNA at any single lag do not exceed 0.51, a moderate correlation at best. Therefore, it is investigated hereafter the correlation analysis directly between T400 and WP or PNA with multiple lags, and try to extract a multiple lagged relationship to better depict the KOE thermal variability based on main atmospheric circulation patterns in the North Pacific. It is shown in Figure 4.20 regression maps of T400 in the western North Pacific. Significant correlations between T400 and WP (PNA) are found at lags 0 and 4 (1 and 2) years in the KOE region. These results emphasize remote as well as local influence of the atmospheric circulation to the KOE thermal variability. The negative regression coefficients with the WP at zero lag, which indicate the local forcing of the atmosphere, suggest a significant direct influence of the WP to the KOE T400 variability. This is consistent with *Pak et al.* [2014] who showed a significant negative correlation between the SST and NPO that is the sea level pressure expression of the WP, in the north of the KE front regardless of the epoch. This local forcing may influence the KOE upper-ocean thermal variability via changes in wind speed and Ekman transport. The remote influence of the WP to the KOE T400 is apparent when it leads by 3-4 years (Figures 4.20d and 4.20e). Opposite to the local influence, the correlation is now positive for the remote WP forcing, in agreement with *Ceballos et al.* [2009] who showed 2-3 years leading correlation of the NPGO index with KOE SSH. On the other hand, *Frankignoul et al.* [2011] claimed a month-leading Aleutian low-like forcing pattern for the meridional shift of the OE, and *Nonaka et al.* [2008] attributed this fast response of OE to barotropic Rossby wave adjustment, as already mentioned. This suggests that the simultaneous correlation/regression between the KOE thermal variability and atmospheric circulation indices (Figures 4.20a and 4.20b) also reflects a barotropic Rossby wave influence.

The PNA exerts a significant influence on the KOE T400 when it leads by 1–-3 years (Figures 4.20g-i), with always a negative correlation suggesting that a strengthened Aleutian low (negative PNA) is related to the positive KOE T400 anomaly. This is consistent with *Qiu* [2003] who showed that the linear baroclinic Rossby wave carries positive (negative) SSH anomalies into the KOE region with a lag of several years, caused by the PDO-related negative (positive) wind stress curl anomalies in the central basin of North Pacific. Consequently, it is verified here that the winter temperature variation in the KOE region is a multiple function of different atmospheric circulation patterns and lags. Taking this fact into consideration, the KOE T400 variations are regressed using the six most significant lagged indices (WP0, WP3, WP4, PNA1, PNA2, PNA3, where the numeric stands for the leading of the indices in year). The regressed temperature Z is obtained from the following multivariate regression equation:

$$Z = a_1X_1 + a_2X_2 + a_3X_3 + a_4X_4 + a_5X_5 + a_6X_6, \qquad (8)$$

where a_N (N=1,…,6) denote regression coefficients, and X_N indicate the lagged indices (WP0, WP3, WP4, PNA1, PNA2, PNA3). The resultant regressed temperature is well correlated (r = 0.70) with T400, explaining almost 50% of the total variance, which is greater than double of that from the regression with any single index and lag (for example, a maximum of 20% (r = 0.45) of the total variance is explained by PNA2 alone). However, the regression result is quite sensitive to the selection of indices and periods. Modeling with atmospheric indices to forecast the KOE T400 is the next step of this research.

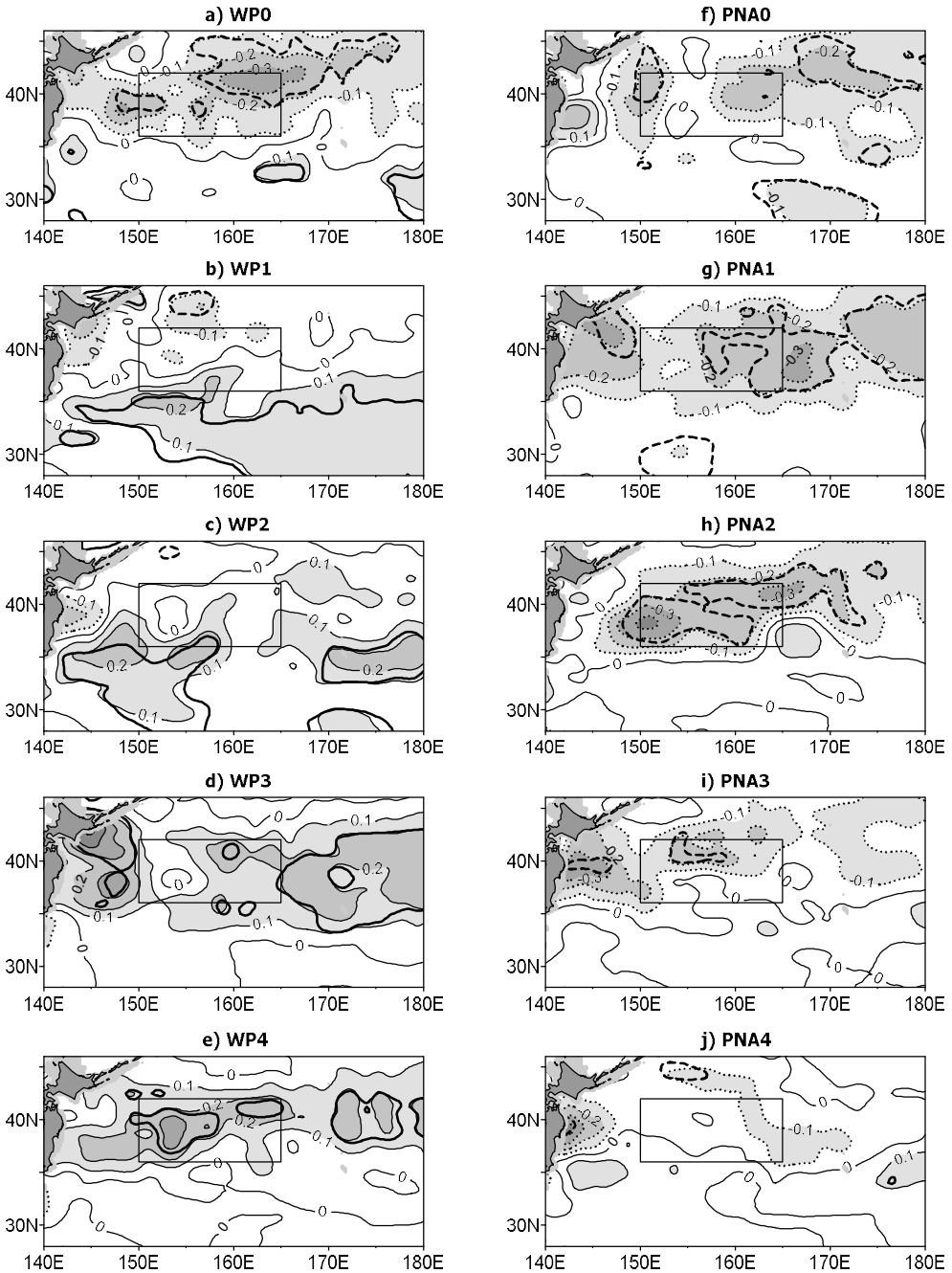

Figure 4.20. Spatial distribution of lagged regression coefficients of T400 onto the leading atmospheric circulation indices, (a–e) WP and (f–j) PNA, with a lag between zero and 4 years. The numeric after the name of indices (WP and PNA) indicates the lag in year. The areas with significant correlations at the 95% confidence level are shown with thick lines.

4.3.2 Relationship between winter Q_{net} and KOE temperature: ocean–to–atmosphere feedback

a. Predictors for net surface heat flux

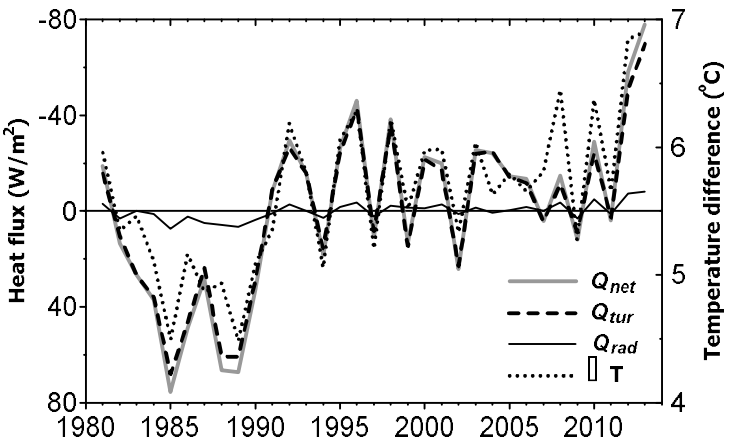

Figure 4.21. Annual time series of area-mean winter (DJF) air-sea temperature difference (ΔT, dotted line) and surface heat flux components over the KOE region. The net surface heat flux (Q_{net}), turbulent heat fluxes (Q_{tur}), and radiative heat fluxes (Q_{rad}) are shown with thick solid, dashed, and thin solid lines, respectively.

The previous subsection showed the ocean dynamics, represented by ADV in this thesis, is important in determining the upper-ocean thermal variability (also SST variability) in the KOE region. Since the SST forcing on the overlying atmosphere exerted by strong ocean dynamics is known to be prevalent in the KOE region, SST is expected to be a dominant factor in causing the Q_{net} variability in the KOE region. The interannual to decadal variability of Q_{net} in the KOE region is mainly due to the surface turbulent heat fluxes (Q_{tur}) with a negligible contribution from the net radiative fluxes (Figure 4.21).

Following *Tomita et al.* [2003], the linearized anomalous latent (Q'_{lat}) and sensible (Q'_{sen}) turbulent heat fluxes can be written in terms of wind speed (W), SST (T_s), surface air temperature (T_a), and humidity at the sea surface (q_s) and at 10 m aloft (q_a), such as:

$$Q'_{lat} = \rho_a L C_L\{q'_s\overline{W} - q'_a\overline{W} + W'(\overline{q_s} - \overline{q_a})\} = \rho_a L C_L(\Delta q'\overline{W} + W'\overline{\Delta q}), \quad (4.21)$$

$$Q'_{sen} = \rho_a c_p C_S\{T'_s\overline{W} - T'_a\overline{W} + W'(\overline{T_s} - \overline{T_a})\} = \rho_a c_p C_S(\Delta T'\overline{W} + W'\overline{\Delta T}), \quad (4.22)$$

where ρ_a is the air density, c_p is the specific heat of air at constant pressure, L is the latent heat of vaporization of water, and C_L and C_S are bulk transfer coefficients for latent heat and sensible heat, respectively; overbars and primes indicate the climatological mean and anomalies, respectively, and $\Delta q' \equiv q'_s - q'_a$, $\overline{\Delta q} \equiv \overline{q_s} - \overline{q_a}$, $\Delta T' \equiv T'_s - T'_a$, $\overline{\Delta T} \equiv \overline{T_s} - \overline{T_a}$.

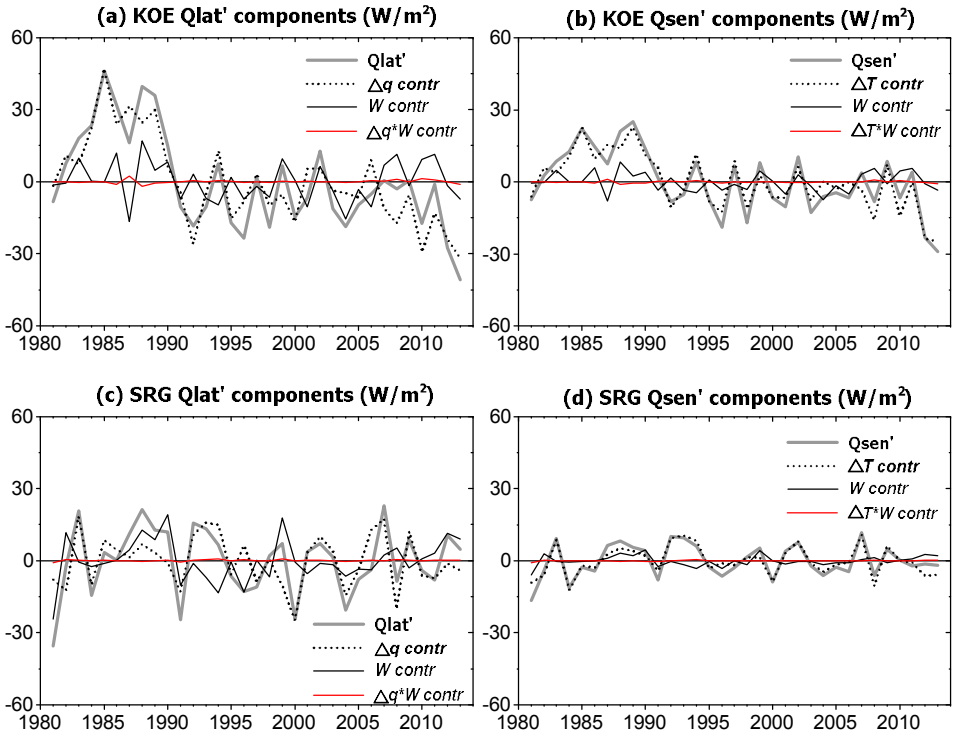

Figure 4.22. Time series of area-averaged DJF anomalous (a, c) latent and (b, d) sensible heat fluxes in the (a-b) KOE and (c-d) SRG regions with thick gray lines, superposed with the turbulent heat flux components of linear contribution of *Δq'* (or *ΔT'*, dotted line), linear contribution of *W'* (black solid line), and nonlinear influence (*W'Δq'* or *W'ΔT'*, red line).

Calculation of nonlinear terms such as $\Delta q'W'$ and $\Delta T'W'$ using model SST and ERA interim data indicates their negligible contribution to latent and sensible heat fluxes (Figures 4.22a and 4.22b). Therefore, only the linear influences of ΔT, Δq, and W, which explain most of Q'_{lat} and Q'_{lat} are considered in (4.21) and (4.22). In order to compare the relative importance among different parameters having different measuring units, the turbulent heat flux terms are regressed on each normalized predicting parameters (Table 4.3). Table 4.3 therefore shows the change in turbulent heat flux in W m^{-2} per one standard deviation change of each parameter. Note that the regression result is not much sensitive to detrending (See Table 4.4 for results from detrended time series), although the magnitude of regression coefficients is somewhat decreased. The decrease of regression coefficients is caused by decreased temporal variability of turbulent heat fluxes. This means that the relationship between turbulent heat fluxes and predictors is not much changed.

Table 4.3 Regression coefficients between winter heat flux components and winter meteorological variables. Qtur: turbulent heat fluxes, Qnet: net heat flux, Ta: air temperature, SST: sea surface temperature (or mixed layer temperature), ΔT: SST minus Ta, qa: specific humidity of atmosphere, qs: specific humidity of sea surface, Δq: qs minus qa, W: wind speed. The regression coefficients having a significant correlation at the 95% confidence level are marked in boldface. The standard deviation of each heat flux component is given (in W m^{-2}) just below the component name. The sign convention is such that if the sign is minus, for example, the upward turbulent fluxes increase when ΔT negatively increases.

	T_a	SST	ΔT	q_a	q_s	Δq	W
Latent (20.23)	-2.97	**-15.05**	**-17.86**	-2.39	**-14.85**	**-17.91**	**-8.56**
Sensible (13.01)	2.26	**-6.87**	**-12.17**	2.33	**-6.65**	**-10.10**	**-5.56**
Q_{tur} (32.74)	-0.71	**-21.92**	**-30.03**	-0.06	**-21.50**	**-28.02**	**-14.12**
Q_{net} (36.00)	-0.12	**-23.95**	**-33.54**	0.70	**-23.48**	**-31.07**	**-14.58**

Table 4.3 clearly shows that the ocean-atmosphere temperature difference ($\Delta T = T_s - T_a$) is the most important predictor for non-seasonal variations of Q_{tur} and

therefore Q_{net} (Figure 4.21). Although the bulk formula for the latent heat flux does not explicitly contain ΔT, ΔT is most strongly correlated with Q_{tur} due to SST influence on specific humidity at the sea surface. Indeed, ΔT and Δq are very well correlated to each other (r = 0.81). Δq and W, which form two key parameters for determining the latent heat flux, are also important, but with smaller regression coefficients compared to that of ΔT in the Q_{tur} and Q_{net} regressions (Table 4.3). Indeed, the correlation coefficient of non-seasonal winter Q_{tur} with ΔT is -0.87 for the entire period, while those with Δq and W are -0.77 and -0.49, respectively. This predominant relationship between ΔT and Q_{tur} is also observed for both E1 (r = -0.78) and E2 (r = -0.81) periods.

Table 4.4 Same as Table 4.3 but for detrended time series.

	T_a	SST	ΔT	q_a	q_s	Δq	W
Latent (16.12)	-0.48	**-9.69**	**-13.14**	-0.79	**-9.53**	**-13.09**	**-7.78**
Sensible (10.99)	3.77	-3.40	**-10.00**	3.26	-3.22	**-7.33**	**-5.13**
Q_{tur} (26.53)	3.28	**13.09**	**-23.13**	2.47	**-12.76**	**-20.42**	**-12.91**
Q_{net} (29.08)	3.93	**-12.89**	**-23.72**	3.20	**-12.54**	**-20.71**	**-12.07**

b. Decadal changes

Positive Q_{net} anomalies are observed during the E1 (a strong monsoon period) in the KOE region (Table 4.5), indicating lesser oceanic heat loss to the atmosphere compared to that during the E2 (a weak monsoon period). Also, the mean wind speed is slightly higher during the E2 (Table 4.5), consistent with *Park et al.* [2012] which showed the recent strengthening tendency of wind speed in the KOE region since 1990 [*Park et al.*, 2012, their Figure 5b]. Indeed, the wind speed increased during the E2 for the most area of the domain including the KOE region (Figure 4.23b), indicating a minor influence of the EAWM. Moreover, the difference of wind speed for composite 5 strong and weak monsoon years obtained from EAWM index shown in Chapters 2 and 3 (Figure 4.24, weak monsoon minus strong monsoon) also shows that the wind speed is rather stronger for weak monsoon. Only the area within the marginal seas and south of KE follows the monsoon system. Consistent with these results, the SST variations in the KOE region are only moderately influenced by the monsoon intensity even during the strong monsoon period (1970–1989) according to *Park et al.* [2012, see their Figure 6]. Moreover, Table 4.3 suggests that the Q_{tur} variability in the KOE region is preferentially determined by ΔT, rather than by wind speed, for which the abrupt SST rise as much as 1.16°C from E1 to E2, compared to a modest increase of 0.46°C in T_a (Table 4.5), plays a decisive role in producing a remarkable difference in heat loss to the atmosphere (47.4 W m^{-2}) between the two periods. In addition, an increase in the wind speed by 0.27 m s^{-1} also contributes to the increase in oceanic heat loss during the E2. Figures 4.23a and 4.23c show that the epoch change of Q_{tur} is mostly determined by the change in ΔT except for the southern recirculation gyre (SRG, 145°–160°E, 30°–34°N) where both Q_{tur} and ΔT are decreased after 1990, suggestive of the stronger influence of the wind speed change. Indeed, the increased oceanic heat loss during the E2 in the SRG region as compared to that during the E1 can be primarily explained by an increase in wind speed (by +0.21 m s^{-1}), because ΔT is decreased by -0.10 °C thus contributing to a positive trend of Q_{tur}. It is also interesting to note that both T_a and SST increased during the E2 compared to E1 regardless of the regions. However, the comparatively larger increase in SST (T_a) results in the increase (decrease) of ΔT in

the KOE (SRG) region (see Table 4.5). This attests that the interannual to decadal variability of winter Q_{net} in the KOE region after the 1990 regime shift (E2) is governed mostly by ocean dynamics (SST change), while that in the SRG by the atmosphere (wind speed change).

Table 4.5 Epoch means of winter (DJF) variables averaged over the KOE region (150°-165°E, 36°-42°N) and the SRG region (145°-160°E, 30°-34°N) obtained from spatially non-filtered data. Note that the values for subperiods (E1 and E2) are anomalies relative to the mean value over the total period (All), while the values for the total period include epoch-mean values.

Region	Period	W ($m\ s^{-1}$)	T_a (°C)	SST (°C)	ΔT (°C)	Q_{tur} ($W\ m^{-2}$)
KOE	1984-1990 (E1)	-0.16	-0.35	-0.90	-0.55	+35.58
	1991-2008 (E2)	+0.11	+0.11	+0.26	+0.15	-11.82
	1984-2013 (All)	10.71	7.46	13.10	5.65	-326.19
SRG	1984-1990 (E1)	-0.11	-0.21	-0.16	+0.05	+2.42
	1991-2008 (E2)	+0.10	+0.09	+0.04	-0.05	-1.98
	1984-2013 (All)	9.51	15.54	19.25	3.71	-276.48

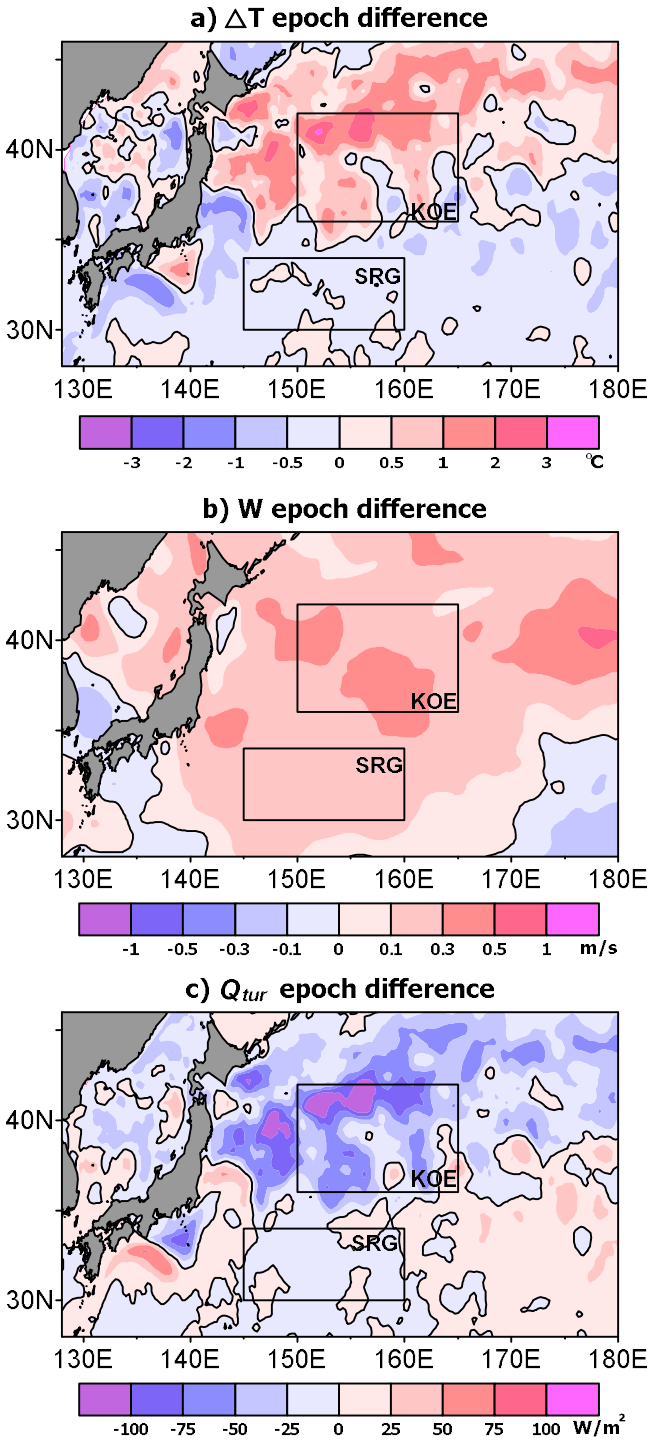

Figure 4.23. Spatial distribution of the epoch difference (1991-2008 minus 1981-1990) of (a) air-sea temperature difference (ΔT, $T_s - T_a$ in °C), (b) wind speed (W in m s^{-1}), and (c) turbulent heat flux (Q_{tur} in W m^{-2}) obtained from 0.25°×0.25° gridded values.

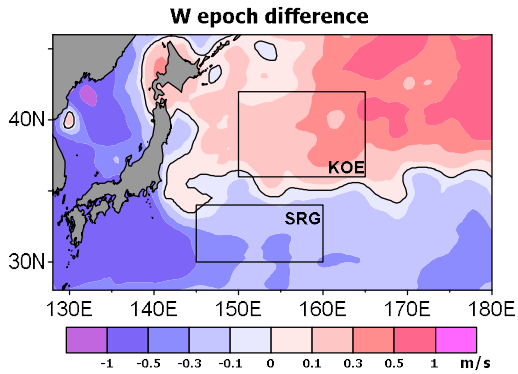

Figure 4.24. Spatial distribution of the composite difference (weak monsoon: 1997, 1990, 2001, 1998, 2007 minus strong monsoon: 1981, 1984, 1986, 1985, 2011) of wind speed obtained from 0.25°×0.25° gridded values.

c. Difference between KOE and SRG regions

The above subsections show that the interannual to decadal variability of the turbulent heat flux in the KOE is mostly explained by SST, which plays a decisive role to the ΔT variability. Also, the magnitude of temporal variability of KOE Q_{net} (Q_{tur}) shows decadal change (Figure 4.13), which is a cause of the epoch-dependency of HSR main contributor. To investigate the robustness of the results observed in the KOE region, the heat budget analysis in the SRG region is also conducted.

The wind speed agrees well with the winter monsoon intensity (Figure 4.24) and the SST is well explained by EAWM and NPO indices during SM-HC period (1973-1987) although the correlation between SST and atmospheric indices significantly decreases during the WM-LC period (1988-2002) in the SRG region (see Chapter 3). The winter heat budget (Figure 4.25a) and the standard deviations of Q_{net} and ADV (Figure 4.25b) in the SRG region suggest that Q_{net} generally plays a more important role to determine the winter HSR variability from 1984 to 2004. Since 2005, the temporal variability of ADV has suddenly increased. This is in contrast to the observation presented in Chapter 3. This discrepancy is still unrevealed, which should be investigated in the future. The regression coefficients of turbulent heat fluxes on the bulk formula variables shown in Table 4.6 suggest

that the atmospheric temperature or specific is a critical predictor for the heat flux, different with decadal variability, where the wind speed plays major role for the heat flux (Figure 4.23).

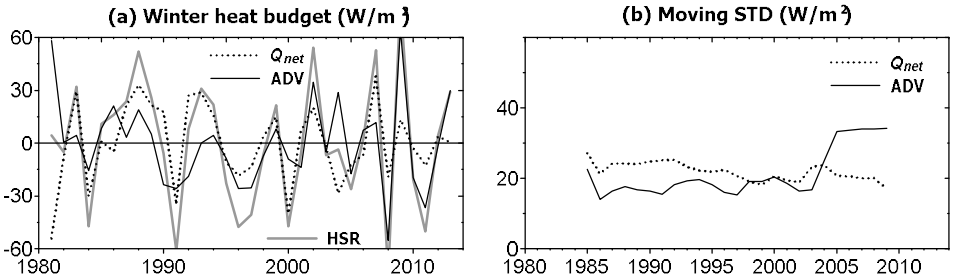

Figure 4.25. (a) Winter SRG region-averaged anomalies of HSR (thick solid lines), Q_{net} (dotted lines), and ADV (thin solid lines). (b) 9-yr moving temporal standard deviation of DJF Q_{net} (dotted) and ADV (solid) in the SRG region.

Table 4.6 Same as Table 4.3 but for SRG region.

	T_a	SST	ΔT	q_a	q_s	Δq	W
Latent (14.02)	7.73	1.35	-10.58	8.14	1.06	-9.97	-7.39
Sensible (6.85)	5.17	1.63	-6.28	4.84	1.51	-4.70	-2.49
Q_{tur} (20.46)	12.91	2.98	-16.86	12.98	2.56	-14.67	-9.88
Q_{net} (22.51)	14.16	2.55	-19.28	13.94	2.09	-16.68	-10.04

d. Negative feedback

The nature of the ocean-atmosphere interactions can also be diagnosed using the local correlation between Q_{net} and SST [*Wu et al.*, 2006; *Wu and Kirtman*, 2007; *Wu and Kinter III*, 2010; *Park et al.*, 2012]. A systematic negative correlation between Q_{net} and SST or T400 for cool seasons from November to May is found (Figure 4.26). The strongest negative correlation occurs when both SST and T400

lead Q_{net} by a few months centered at 2 months, indicating a negative feedback of the ocean-atmosphere interactions. Positive (negative) ocean temperature anomalies induce upward (downward) turbulent heat flux anomalies due to an increase (decrease) in temperature difference between the sea surface and overlying atmosphere, which in turn results in a negative (positive) temperature tendency according to equation (4.4), acting to dampen the upper-ocean temperature increase. The results are consistent with the coupled climate model results of *Kwon and Deser* [2007]. It is worth stressing that the maximum correlation coefficients of Q_{net} with T400 (r = -0.81 for NDJ T400 and FMA Q_{net}) is significantly higher than those with SST (r = -0.72 for DJF SST and FMA Q_{net}), supporting that the upper-ocean heat content is a better predictor than SST for the ocean-atmosphere interactions [*Deser et al.*, 2003; *Dawe and Thompson*, 2007; *Kelly et al.*, 2010]. Due to the long autocorrelation time scale of T400, the area of significant correlation between Q_{net} and T400 is elongated along the y-axis (Figure 4.26).

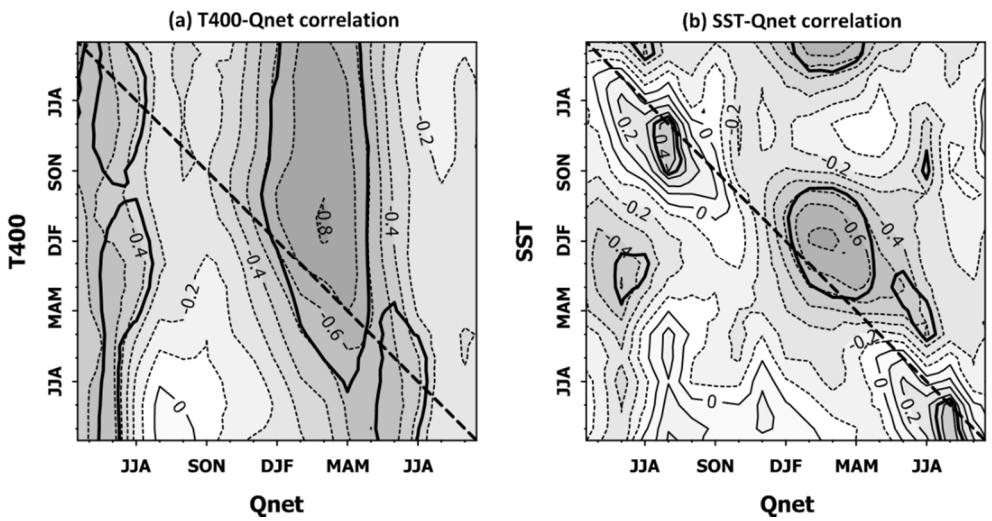

Figure 4.26. Lagged correlation of (a) T400 and (b) SST with Q_{net} for different months during 1981–2013 in the KOE region. JJA, SON, DJF, and MAM denote the averaging months used for constructing yearly time series: for example, DJF means December through February, etc. Negative correlation coefficients are marked with dotted line. The significant correlations at 95% confidence level are marked with thick lines.

4.3.3 Causes of increased contribution of Q_{net} during E1

In section 4.2.3, presented is the epoch-dependent contributions of Q_{net} and ADV to HSR in the KOE region. Q_{net} has stronger temporal variability compared to ADV during E1, while during E2 ADV dominates. Here, explored are the causes of the change in contributions of Q_{net} and ADV for two contrasting periods. As shown in section 4.2.3, the standard deviation of KOE Q_{net} has significantly decreased during E2 (48.0 W m^{-2} during E1 and 19.4 W m^{-2} during E2, Table 4.7), while the standard deviation of ADV is nearly insensitive to the different epochs (27.7 W m^{-2} during E1 and 27.4 W m^{-2} during E2, Table 4.7). This significant (insignificant) difference of temporal standard deviation of Q_{net} (ADV) during the E1 and E2 periods suggests that the epoch-dependent change of the relative contribution of Q_{net} and ADV to HSR arise from the decadal change of temporal variability of Q_{net}.

It is mentioned above that the variability of Q_{net} is mostly determined by ΔT in the KOE region (Tables 4.3 and 4.5). The standard deviation of ΔT in the KOE region is significantly different (0.70°C vs 0.41°C during the E1 and E2 periods, respectively, Table 4.7). The standard deviation of SST also shows significant difference with epochs, while the difference is insignificant for T_a (Table 4.7), suggesting that the SST variability or the upper ocean thermal variability is important for the decadal change of ΔT, that is Q_{net}, variability.

The depth-averaged temperature (T400) can be reconstructed and the contribution of each heat budget term (HSR, Q_{net}, ADV) to the winter temperature variability in the KOE region can be quantified using the temperature tendency equation (4.4), time-integrating from January of the previous year to January of the present year to represent the January T400, the center month of the winter definition (DJF). More precisely, the winter T400 associated with each heat budget term can be reconstructed as:

$$T400_r(yr) = T400_r(yr-1) + \Delta t \times \langle \frac{\partial T}{\partial t} \rangle_{yr-1} \quad (4.23),$$

where $T400_r$ is the reconstructed winter T400 and yr indicates the calendar year. Δt denotes the integration time scale, 1 year. The tendency term $\frac{\partial T}{\partial t}$ includes Q_{net}

and ADV divided by $\rho c_p h$, the sum of which is HSR (See equation (4.4)). The bracket ($\langle\,\rangle_{yr}$) denotes the annual average of *yr* from January to the following January. Integrating January to January temperature tendency term, the KOE T400 series of January, the center month of the defined winter (DJF), can be reconstructed. The corresponding annual time series of reconstructed winter temperature are denoted by $T400_r^Q$, $T400_r^{ADV}$, and $T400_r^{HSR}$, respectively (Figure 4.27). Because of negligible residuals RES (in addition to the erroneous horizontal velocity field on August 2004), ADV is computed as the difference between HSR and Q_{net}. $T400_r^Q$ and $T400_r^{ADV}$ have opposing linear trends reaching up to almost 3°C yr^{-1} in the KOE region, thus mostly compensating each other to yield a small net warming trend of about 0.06°C yr^{-1}. Because only the nonseasonal anomalies of each heat budget term are taken here, the record-length average of each heat budget term is not considered in equation (4.23). Therefore, the reconstructed T400 due to each heat budget term should be zero at the end of reconstruction (Jan. 2013) because it is assumed to be zero at the start (Jan. 1981). The correlation between KOE T400 and KOE $T400_r^{HSR}$ is higher than 0.9, implying that the reconstructed T400 well represents the KOE T400.

As expected from the time series of annual-averaged Q_{net} shown in Figure 4.21, $T400_r^Q$ increases during the E1, while it decreased afterward. $T400_r^{ADV}$ varies in opposition to $T400_r^Q$ with a high negative correlation of -0.94 when $T400_r^{ADV}$ leads by 2 yr. These out of phased variations further strengthen the negative feedback paradigm of ocean-atmosphere interactions in the KOE region, in which Q_{net} is mainly controlled by ocean advection-induced T400 anomalies. In short, the KOE T400 anomaly is determined by ADV and 2 yr lagged response of Q_{net} to ADV variability, regardless of period. However, as described in Table 4.7, the SST variability (much related to T400 variability) is significantly higher, so that Q_{net} variability is much higher during E1 period compared to those during E2 period. This means that ocean dynamics (ADV) play a primary role in determining the upper ocean thermal variability in the KOE region, which makes higher and lower temporal variability of Q_{net} during E1 and E2 periods, respectively. However, it is not obvious how the combined effects of ADV and lagged Q_{net} response to ADV cause the different degree of SST variability in the KOE region during E1

and E2 periods shown in Table 4.7, which needs to be further investigated in future. Because temporal variability of ADV is nearly insensitive to the epochs (Table 4.7), Q_{net} could play an important role to the HSR variability due to its strong variability during the E1 period.

Table 4.7. Standard deviations of winter (DJF) variables averaged over the KOE region (150°–165°E, 36°–42°N). F-Test column is filled with "O" if the standard deviation of two periods is significantly different at 95% confidence level.

Variables	E1 (1981-1990)	E2 (1991-2008)	F-Test
Q_{net} (W m^{-2})	48.0	19.4	O
ADV (W m^{-2})	27.7	27.4	X
ΔT (°C)	0.70	0.41	O
SST (°C)	1.16	0.53	O
T_a (°C)	0.66	0.55	X

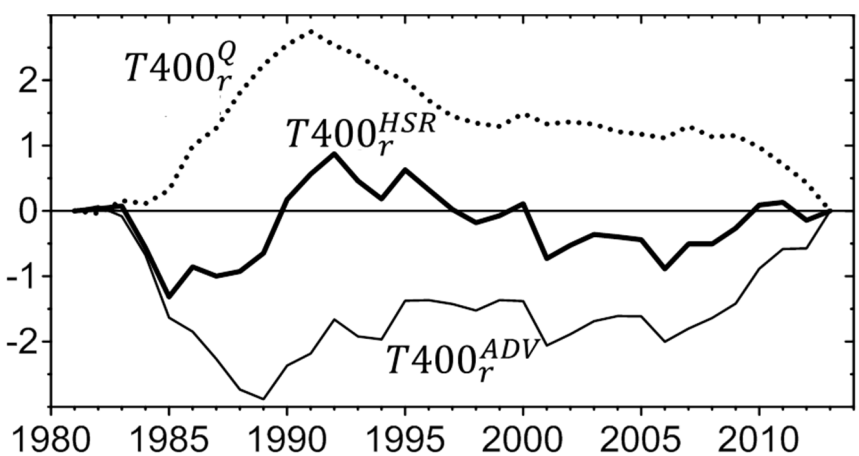

Figure 4.27. Area averaged reconstructed T400 time series obtained from annual averaged HSR ($T400_r^{HSR}$, thick line), Q_{net} ($T400_r^Q$, dotted line), and ADV ($T400_r^{ADV}$, thin line) in the KOE region with a unit of °C.

Chapter 5. Conclusion

5.1. Nonstationary relationship between the EAWM and NPO

The EAWM (determined nearly entirely by the SH variability) and the NPO (a surface expression of the WP) form two predominant climate modes affecting the winter climate of the Far East and the western North Pacific. By analyzing data over 48 winter seasons (1965–2012), it is shown that all the above four climate indices (EAWM, SH, NPO, WP) underwent an abrupt regime shift around 1988, from a strong winter monsoon regime before 1988 to a weaker monsoon regime afterward. The 11-yr running correlation indicates that the EAWM and NPO were tightly connected to each other during the last two thirds of the strong monsoon regime (15 years from 1973 to 87; SM–HC epoch) but nearly completely disconnected during the first two-thirds of the weak monsoon regime (15 years from 1988 to 2002; WM–LC epoch).

This regime-dependent nonstationary relationship between the EAWM and NPO is related to a tight vs insignificant statistical connection in SLP variations between the SH and NPO centers of action during the SM–HC vs WM–LC epoch. This is associated with the pronounced decadal weakening of the SH system over the entire Eurasian continent since the 1988 regime shift as well as the concomitant, positive NPO/WP-like dipole change in surface and upper-level atmospheric circulation patterns over the North Pacific. It is also shown that the EAWM and NPO are consistently well linked to the upper-level blocking events, Ural and Kamchatka blockings, which explain predominantly the variability of the SH and WP, respectively. This is generally consistent with *Takaya and Nakamura* [2013].

These leading modes of atmospheric surface circulation variability affect the western North Pacific SST differently in each regime. During the SM–HC, when the EAWM and NPO were strongly connected to each other, a very similar spatial pattern of SST anomalies was projected by these circulation modes, while a quite dissimilar and weakened pattern was observed during the WM–LC when the EAWM and NPO were practically independent. In particular, impact of the EAWM on SST during the latter epoch shrank remarkably into a limited area in the East

China Sea, making a clear distinction from the NPO impact.

It is paid special attention to the dynamics and mechanism underlying the nonstationary relationship between the EAWM and NPO, where a significant gap exists in common understanding. Statistical analyses on the evolution of storm tracks across the 1988 regime shift and tropical influence (ENSO) enabled us to better understand the Northern Hemisphere winter tropical–extratropical teleconnection in the North Pacific, which also reveals a nonstationary decadal evolution: a significant triple connection among the EAWM, NPO, and ENSO in the western North Pacific basin during the SM–HC, which vanishes in the WM–LC when the ENSO influence is more preferentially projected onto the PNA teleconnection pattern in the eastern basin.

In particular, the correlations between the total precipitable water and the above three indices suggest a tentative mechanism for the nonstationary relationship among the EAWM, NPO, and ENSO indices as follows: During the SM-HC, the East Asian trough deepens because of the enhanced Tibetan orographic forcing under strengthened monsoon winds, creating a well-developed anomalous upper-level cyclone north of the Korean Peninsula. This anomalous cyclone is in phase with the Rossby wave train generated by tropical heating in the Philippine Sea, which reinforces the latter wave train by a near-resonant effect, yielding a tight triple connection among the EAWM, NPO, and ENSO. On the other hand, the abrupt decline of the EAWM after its 1988 regime shift induces a concomitant weakening of the East Asian trough, yielding a pronounced anomalous anticyclone that is locally out of phase to the Rossby wave train from propagating farther northward. As a consequence, the triple connection among the EAWM, NPO, and ENSO vanishes. It is concluded therefore that the nonstationary relationship between the EAWM and NPO is primarily attributable to the recent abrupt decline of the EAWM since the late 1980s, although the causality of the latter decline remains to be investigated. Also, long-term investigation of moving correlation between EAWM and NPO suggests that the historical moving correlation during last 100 years is not well correlated to the intensity of EAWM, which is well related to the intensity of East Asian trough, indicating that above mechanism is not always working well. It is necessary to investigate the other underlying mechanism for this nonstationary relationship using coupled or

atmospheric model in the future.

5.2 Upper-ocean heat content variability in the KOE region

Based on the MERCATOR 1/12°-resolution OGCM ORCA12, I have investigated the upper 400 m heat budget and the winter temperature variability in the KOE region where the ocean-atmosphere interaction is strongest in the North Pacific. Validation against observational data indicates that the model reproduces realistically the KOE region thermal variability with significantly high correlations. In addition, the model heat budget is well closed in that HSR (heat storage rate) is nearly perfectly balanced with the sum of Q_{net} (net surface heat flux) and ADV (ocean heat advection), with a negligible residual. As in previous heat budget studies in the KOE region [*Vivier et al.*, 2002; *Kwon and Deser*, 2007], the seasonal variability of HSR is primarily explained by Q_{net} and secondarily by ADV, while its interannual variability is dominated by ADV during the entire period (1981–2013). It is found that there is a significant epoch-dependent change in the relative contribution of Q_{net} and ADV to winter HSR for two periods before and after the 1990 regime shift. During the E1 period (1981–1990), the temporal variability (standard deviation) of Q_{net} (48.0 W m^{-2}) is stronger than that of ADV (27.7 W m^{-2}) in the KOE region. While they become 19.4 W m^{-2} and 27.4 W m^{-2}, respectively, during the E2 period (1991–2008), suggesting that Q_{net} (ADV) plays relatively more important role for the HSR variability in the KOE region during E1 (E2) period. These model-derived results nicely confirm the observational evidence highlighted in *Park et al.* [2012], which shows a strong atmospheric influence on the SST variability in the western North Pacific during the strong EAWM period before 1990 [see also *Pak et al.*, 2014] but increasingly important ocean dynamics especially in the KOE region during the weak EAWM period after 1990. However, it is found that the upper-ocean thermal variability in the KOE region is not directly influenced by the EAWM, which deserves further research in future work.

The comparison between the two leading PC time series of T400 and the OE and KE indices suggests that the interannual to decadal upper-ocean thermal

variability in the western North Pacific is controlled primarily by the meridional shift of the OE front and secondarily by that of the KE front. The OE index also explains the area-averaged KOE T400 as well as the EOF1 of T400 in the western North Pacific. The meridional shift of the OE is significantly correlated with both the WP and PNA patterns at multiple lags between 0 and 4 yr, suggesting that the meridional shift of OE is influenced by both barotropic and baroclinic Rossby wave dynamics triggered by atmospheric forcing. The EOF2 of T400 is well explained by the KE index, showing the northward (southward) shift concomitant with the strengthening (weakening) of the KE front, in agreement with *Qiu and Chen* [2005], but in contrast to *Taguchi et al.* [2007] which claims the existence of two independent modes of the meridional displacement and strength of the KE.

In the KOE region, the turbulent heat flux (Q_{tur}), which dominates the Q_{net} variability, is best explained by the sea-air temperature difference (ΔT) rather than wind speed or humidity difference, suggesting that the Q_{net} variability of the region is not directly controlled by the atmosphere. The E1 period is characterized by the positive Q_{net} anomaly (less heat loss from the ocean), and smaller ΔT and wind speed as compared to those during the E2 period, in complete opposition to the expected negative Q_{net} anomaly (larger heat loss from the ocean) and stronger wind if the Q_{net} variability would be under direct control of the winter monsoon. This indicates that the temperature difference between ocean and atmosphere, mainly caused by changes in SST, is a critical factor in determining the Q_{net} variability in the KOE region, thus the ocean-to-atmosphere feedback or the negative Q_{net} feedback. The strong negative correlation between the winter ocean temperature and lagged Q_{net} (Figure 4.26) further evidences the negative Q_{net} feedback damping the temperature anomaly driven by the ocean dynamics (ADV).

The decadal changes of contribution of Q_{net} and ADV to the KOE HSR during two contrasting epochs are explained by the difference in the standard deviation of SST during each of the two epochs, which in turn results in the variability of Q_{net} in those two epochs. During E1 period, temporal variability of SST, that is ΔT, in the KOE region is significantly higher than that during E2. This thermal variability is partly (r = 0.6) due to the ocean dynamics represented by meridional shift of OE. The 2yr-lagged response of reconstructed T400 due to Q_{net} to that due to ADV suggest that ocean dynamics plays an important role for determining upper ocean

thermal variability in the KOE region, which yields stronger vs weaker temporal variability of Q_{net} during E1 vs E2 periods, respectively. Because the ADV variability in each epoch is not much different, the epoch-dependent Q_{net} variability plays a relatively important role to the HSR variability during E1 period compared to E2 period. It should be noted that, although the temporal standard deviation of ADV is nearly insensitive to the different epochs (Table 4.8), the epoch-mean of the anomaly of KOE ADV is somewhat different (Figure 4.11a). Because ocean temperature anomaly induced by ADV variability is shown to cause Q_{net} variability, it will be also interesting to investigate the reason for the difference of mean KOE ADV during E1 and E2 periods, which has not been addressed in the thesis. In short, it is imperative to investigate the long-term variability of ADV for understanding the KOE T400 variability.

The model-derived results, which show the predominant role of ocean advection for the KOE thermal variability especially after the 1990 regime shift, are well consistent with previous work [*Park et al.*, 2012] and Chapter 3 [*Pak et al.*, 2014]. This is the first to report that a high-resolution OGCM like ORCA12 is sufficiently realistic enough to complement the observations in a data-poor area for investigating the decadal-scale upper-ocean variability. While the previous study has only qualitatively inferred via statistical methods, it has been shown quantitatively the different main contributor of heat storage rate in the KOE region before and after 1990 regime shift resorting to the model results.

5.3. New findings, limitations, and future studies

This research confirms the results from the previous studies have shown that the atmospheric forcing in the central/eastern basin of the North Pacific is very important for the long-term (interannual to decadal) variability of the KOE SSH/SST, that is, upper-layer thermal variability. First of all, the thesis confirms that the seasonal heat storage rate in the KOE region and western North Pacific is mainly controlled by air-sea heat flux and secondarily Ekman heat transport. On the other hand, many previous researches [*Deser et al.*, 1999; *Schneider and Miller*, 2001; *Seager et al.*, 2001; *Qiu*, 2003; *Qiu and Chen*, 2005; *Ceballos et al.*, 2009;

Sugimoto and Hanawa, 2009] referred in the thesis showed that the upper ocean thermal variability in the KE, OE, and KOE region is well explained by the delayed oceanic response from Rossby wave dynamics propagating westward with various data sets. This thesis also showed similar results that contribution of heat advection always dominates heat flux, when the spatial size of the filtering window is less than 6°×4°. When considering KOE (150°-165°E, 36°-42°N) averaged time series, relative contribution of net heat flux is almost similar or higher than that of heat advection. This is come from the difference of spatio-temporal scale of Q_{net} and ADV. Frankly speaking, the data provided from MERCATOR Ocean is limited in the region near western North Pacific, so that east of dateline is empty now. This is why it is not well tested the westward propagation via first order baroclinic Rossby wave with model data. In the future work, full resolution and full spatial coverage of ocean model data should be provided.

As mentioned in Introduction, *Park et al.* [2012] tried to relate the winter SST variability in the western North Pacific and EAWM, while *Yeh et al.* [2011] tried to relate the Yellow Sea winter SST with NPO. According to the thesis, the winter EAWM and NPO shows gererally similar long-term variability during the recent decades. A closer look suggests that both atmospheric patterns show very similar variability and have very strong impact on the winter SST especially in the western North Pacific before a sudden weakening of EAWM (1988). After the weakening of EAWM, both the relationship between EAWM and NPO and relationship between atmospheric indices and SST in the western North Pacific (especially southern recirculation gyre region) becomes weak. This nonstationary relationship between atmospheric indices and SST as well as between atmospheric indices themselves are not well reported. The weakened correlation between atmospheric indices and SST in the western North Pacific during WM-LC period indicates the influence of magnitude of wind stress or wind stress curl to the winter SST is weakened. *Kako and Kubota* [2007] showed that preconditioning of temperature profiles during preceding summer is also important for the variability of maximum depth of winter mixed layer. Therefore, it is very interesting in the future study to verify whether the vertical density gradient of upper ocean in the study area had been changed before and after 1988 regime shift.

Also, this thesis has found the eastward migration of NPO-like atmospheric

patterns. However, the detail underlying mechanism is not well investigated, because the research of this thesis is mostly based on the simple correlation (and regression) using observational and reanalysis product (and 1 ensemble of realistic ocean model product). In the published paper attached in the appendix, my co-authors and I tried to describe and investigate what is happened during SM-HC and WM-LC periods for the atmosphere and ocean, but those are mostly on the speculation with some limited observation data and previous theories. From the 20th Century reanalysis V2 [*Compo et al.*, 2011], it is also observed that changing of the relationship between EAWM and NPO is not only occurred at 1988 regime shift and it is somewhat difficult to say that changing of the relationship is always related to the intensity of the East Asian trough. Unfortunately, very long-term simulation of coupled model (CESM-LE) results (Figure 3.5c) do not show any evident regime shift (both of the monsoon intensity and the relationship between EAWM and NPO). Also, this thesis only tried to related the nonstationary relationship with changing of ENSO's influence. However, AO is also dominant atmospheric patterns.

To reveal underlying mechanism of these nonstationary relationships, it is necessary to run the coupled climate models to test the hypothesis that suggested in *Pak et al.* [2014], the heating of Philippine is one of heat source for transfering heats to the NPO centers and SH center. Also, it is not well investigated that the reason of changing relationship between SST and atmospheric indices. The weakened relationship between SH or EAWM and SST when EAWM is weakened is reasonable, because the weakened monsoon wind is difficult to influence to the ocean. The NPO and AL influences are rather become stronger after the weakening of EAWM. These undescribed mechanisms should be investigated with coupled climate model with various ensemble runs in the future.

Because the portion of the variability of SST explained by atmospheric indices are decreased after near-1990, it is tempted to think that ocean dynamics play more important role after 1990, and this thesis revealed, at least in the KOE region, that air-sea heat flux which is related to the atmospheric forcing plays lesser role during this period. However, in the above result of nonstationary relationship between SST and atmospheric indices is mainly concentrated on the southern recirculation gyre (SRG) region, not KOE region. In the SRG region, it is not found that the

changing of contribution of Q_{net} (or ADV) near 1990, only near 2005 contribution change was found. So, it is difficult to directly relate the finding of nonstationary relationship between SST and indices mainly in the SRG region before/after 1990 and changing of contribution of Q_{net} (ADV) near 1990 in the KOE region from the ORCA12 data. However, recently, *Sugimoto and Kako* [2016] revealed that ocean dynamics represented by decadal pre-existing (JAS) mean thermocline depth (MTD) plays more important role after 1990, while winter heat flux is important to determine MLD in the SRG region due to stronger MTD anomalies after 1990. Their result is consistent with the results in Chapter 3 showing that atmospheric indices are more important to determine SST variability before 1990. So, it can be said that contribution of ocean dynamics is more important in the KOE and SRG regions. Moreover, very recent periods, atmospheric influence becomes again strong; the intensity of EAWM becomes stronger and the correlation between EAWM and SST in the western North Pacific also becomes stronger.

In addition, Q_{net} has both oceanic and atmospheric contributions to its interannual to decadal variability. Especially, in the Chapter 4, the variability of KOE Q_{net} is dominated by its oceanic contribution (due to SST or upper ocean heat content variability). However, in the Chapter 3, one of the main focus is the atmospheric influences to the winter SST variability, that is due to the magnitude of wind stress or wind stress curl. So, for the consistency between Chapter 3 and 4, it is necessary to extract pure atmospheric contributed Q_{net} variability in the heat budget analysis, which should be conducted in the later study.

It is also interesting that the timing of the regime shift in Chapter 3 (1987/88) leads by 3 years that in Chapter 4 (1990/91). The shift timing in *Park et al.* [2012] is 1989/90 which is almost same with that in Chapter 4. Note that the oceanic variables (SST, T400, and HSR) are mainly considered in Chapter 4 and *Park et al.* [2012], while atmospheric indices (EAWM and NPO) is used to define the regime shift in Chapter 3. The 3-year lag is similar to the time scale of the propagation of 1st order baroclinic Rossby waves from central North Pacific to the KOE region in the midlatitudes. However, in present stage, it is very difficult to explain why there exists 3 years' difference of the timing of major changes between Chapter 3 and Chapter 4.

In the Chapter 3, the analysis period is divided by the regime of intensity of

EAWM. However, in the Chapter 4, changing of contribution of Q_{net} and ADV to HSR is not depedent on the intensity of EAWM. Even, the wind speed is rather stronger during E2 period which corresponds weak EAWM. So, it is reasonable to interpret that a sudden weakening of EAWM is just a phenomenon of the difference of two periods before and after 1990. My future study will be concentrated on this kind of long-term change before and after 1990. Interestingly there are many phenomena of a sudden change before and after near 1990 in the western North Pacific. Some of these phenomena are related to each other and others are not.

1) Strong EAWM -> Weak EAWM
2) Strong correlation between EAWM and NPO -> Weak correlation
3) Eastward shift of NPO (WP)-like dipole pattern
4) Eastward shift of ENSO's influence
5) Strong contribution of Q_{net} to HSR -> Weak contribution
6) Weak contribution of ADV to HSR -> Strong contribution
7) Meander type path of Kuroshio (before Izu Ridge) -> Strait type path [*Seo et al.*, 2014b]
8) Strong correlation MLD-Heat flux -> Strong correlation MLD-MTD [*Sugimoto and Kako*, 2016]
9) NPGO type (and secondarily PDO type) SST change [*Yeh et al.*, 2011]
10) Negative AO -> Positive AO (positive SLP in south)
11) Negative NPO/WP -> Positive NPO/WP (positive SLP in south)
12) Strong SH -> Weak SH
13) Strong correlation between SST gradient and storm track activity -> Weak
14) Strong correlation between NPO and WP -> Weak (but still significant)
15) Weak storm track intensity -> Strong storm track intensity

Bibliography

Adcroft, A., C. Hill, and J. Marshall (1997), Representation of topography by shaved cells in a height coordinate ocean model, *Mon. Wea. Rev.*, 125, 2293–2315.

Alexander, M. A., J. D. Scott, and C. Deser (2000), Processes that influence sea surface temperature and ocean mixed layer depth variability in a coupled model, *J. Geophys. Res.*, 105, doi:10.1029/2000JC900074.

Amante, C., and B. W. Eakins (2009), ETOPO1 1 Arc-Minute Global Relief Model: Procedures, Data Sources and Analysis, NOAA Technical Memorandum NESDIS NGDC-24, 19 pp.

An, S.-I (2008), A mechanism for the multi-decadal climate oscillation in the North Pacific, *Theor. Appl. Climatol.*, 91, 77-84.

Arakawa, A., and V. R. Lamb (1981) A potential enstrophy and energy conserving scheme for the shallow water equations, *Mon. Wea. Rev.*, 109, 18-36.

Barriopedro, D., R. Garcia-Herrera, A. R. Lupo, and E. Hernandez (2006), A climatology of Northern Hemisphere blocking. *J. Climate*, 19, 1042–1063.

Barnier, B., G. Madec, T. Penduff, J.-M. Molines, A.-M. Treguier, J.le Sommer, A. Beckmann, A. Biastoch, C. Böning, J. Dengg, C. Derval, E. Durand, S. Gulev, E. Remy, C. Talandier, S. Theetten, M. Maltrud, J. Mc Clean and B. de Cuevas (2006), Impact of partial steps and momentum advection schemes in a global circulation model at eddy permitting resolution, *Ocean Dyn.*, 56(5-6), 543–567, doi:10.1007/s10236- 006-0082-1.

Becker, J. J., D. T. Sandwell, W. H. F. Smith, J. Braud, B. Binder, J. Depner, D. Fabre, J. Factor, S. Ingalls, S.-H. Kim, R. Ladne, K. Marks, S. Nelson, A. Pharaoh, R. Trimmer, J. Von Rosenberg, G. Wallace, P. Weatherall (2009), Global Bathymetry and Elevation Data at 30 Arc Seconds Resolution: SRTM30_PLUS, *Marine Geodesy*, 32(4), 355 – 371.

Bond, N. A., J. E. Overland, M. Spillane, and P. Stabeno (2003), Recent shifts in the state of the North Pacific, *Geophys. Res. Lett.*, 30, doi:10.1029/2003GL018597.

Boris, J. P., and D. L. Book (1973). Flux-corrected transport, I: SHASTA, a fluid transport algorithm that works, *J. Comput. Phys.*, 11, 38-69.

Bouillon, S., M. A. M. Maqueda, V. Legat, and T. Fichefet (2009), An elastic-viscous-plastic sea ice model formulated on Arakawa B and C grids, *Ocean Modelling*, 27, 174-184.

Cayan, D. R. (1992), Latent and sensible heat flux anomalies over the Northern Oceans: driving the sea surface temperature, *J. Phys. Oceanogr.*, 22, 859-881.

Ceballos, L. I., E. Di Lorenzo, C. D. Hoyos, N. Schneider, B. Taguchi (2009), North Pacific Gyre Oscillation synchronizes climate fluctuations in the eastern and western boundary systems, *J. Climate*, 22, 5163-5174.

Cheng, Y.-H., C.-R. Ho, Q. Zheng, N.-J. Kuo (2014), Statistical characteristics of mesoscale eddies in the North Pacific derived from satellite altimetry, *Remote Sens.*, 6, 5164-5183.

Compo, G. P., J. S. Whitaker, P. D. Sardeshmukh, N. Matsui, R. J. Allan, X. Yin, B. E. Gleason, R. S. Vose, G. Rutledge, P. Bessemoulin, S. Bronnimann, M. Brunet, R. I. Crouthamel, A. N. Grant, P. Y. Groisman, P. D. Jones, M. C.

Kruk, A. C. Kruger, G. J. Marshall, M. Maugeri, H. Y. Mok, O. Nordli, T. F. Ross, R. M. Trigo, X. L. Wang, S. D. Woodruff, S. J. Worley (2011), The twentieth Century reanalysis project, *Q. J. R. Meteorol. Soc.*, 137, 1-28.

Dai, A., and K. E. Trenberth (2002), Estimates of freshwater discharge from continents: Latitudinal and seasonal variations, *J. Hydrometeorol.*, 3, 660-687.

Dawe, J. T., and L.A. Thompson (2007), PDO-related heat and temperature budget changes in a model of the North Pacific, *J. Climate*, 20, 2092-2108.

Dawson, A., A. J. Matthews, D. P. Stevens (2011), Rossby wave dynamics of the North Pacific extra-tropical response to El Nino: Importance of the basic state in coupled GCMs, *Climate Dyn.*, 37, 391-405.

Dee, D. P., S. M. Uppala, A. J. Simmons, P. Berrisford, P. Poli, S. Kobayashi, U. Andrae, M. A. Balmaseda, G. Balsamo, P. Bauer, P. Bechtold, A. C. M. Beljaars, L. van de Berg, J. Bidlot, N. Bormann, C. Delsol, R. Dragani, M. Fuentes, A. J. Geer, L. Haimberger, S. B. Healy, H. Hersbach, E. V. Hólm, L. Isaksen, P. Kållberg, M. Köhler, M. Matricardi, A. P. McNally, B. M. Monge-Sanz, J.-J. Morcrette, B.-K. Park, C. Peubey, P. de Rosnay, C. Tavolato, J.-N. Thépaut, and F. Vitart (2011), The ERA-Interim reanalysis: configuration and performance of the data assimilation system, *Q.J.R. Meteorol. Soc.*, 137, 553–597.

Deser, C., M. A. Alexander, and M. S. Timlin (1999), Evidence for a wind-driven intensification of the Kuroshio current extension from the 1970s to the 1980s, *J. Climate*, 12, 1697-1706.

Deser, C., M. A. Alexander, and M. S. Timlin (2003), Understanding the persistence of sea surface temperature anomalies in mid-latitudes, *J. Climate*, 16, 57-72.

Di Lorenzo, E., N. Schneider, K. M. Cobb, P. J. S. Franks, K. Chhak, A. J. Miller, J. C. McWilliams, S. J. Bograd, H. Arango, E. Curchitser, T. M. Powell, and P. Riviere (2008), North Pacific gyre oscillation links ocean climate and ecosystem change, *Geophys. Res. Lett.*, 35, doi:10.1029/2007GL032838.

Emery, W. J., and R. E. Thomson (1997), *Data Analysis Methods in Physical Oceanography*, Pergamon, 638pp.

Frankignoul, C., N. Sennechael, Y.-O. Kwon, and M. A. Alexander (2011), Influence of the meridional shifts of the Kuroshio and the Oyashio extensions on the atmospheric circulation. *J. Climate*, 24, 762-777.

Frenger, I., N. Gruber, R. Knuti, M. Munnich (2013), Imprint of Southern Ocean eddies on winds, clouds and rainfall, *Nature geoscience*, doi:10.1038/NGEO1863.

Gong, D.-Y., S.-W. Wang, and J.-H. Zhu (2001), East Asian winter monsoon and Arctic Oscillation. *Geophys. Res. Lett.*, 28, 2073-2076.

Grodsky, S. A., J. A. Carton, H. Liu (2008), Comparison of bulk sea surface and mixed layer temperatures, *J. Geophys. Res.*, 113, C10026, doi:10.1029/2008JC004871.

Hare, S. R., and N. J. Mantua (2000), Empirical evidence for North Pacific regime shifts in 1977 and 1989, *Prog. Oceanogr.*, 47, 103-145.

Held, I. M., M. Ting (1990), Orographic versus thermal forcing of stationary waves: The importance of the mean low-level wind, *J. Atmos. Sci.*, 47, 495-500.

Hirose, N., K. Nishimura, and M. Yamamoto (2009), Observational evidence of a warm ocean current preceding a winter teleconnection pattern in the northwestern Pacific, *Geophys. Res. Lett.*, 36, L09705,

doi:10.1029/2009GL037448.
Hosoda, S., M. Nonaka, T. Tomita, B. Taguchi, H. Tomita, N. Iwasaka (2015), Impact of downward heat penetration below the shallow seasonal thermocline on the sea surface temperature, *J. Oceanogr.*, 71, 541-556.
Huang, B., Y. Xue, D. Zhang, A. Kumar, M. J. McPhaden (2010), The NCEP GODAS Ocean analysis of the tropical Pacific mixed layer heat budget on seasonal to interannual time scales, *J. Climate*, 23, 4901-4925.
Ishi, Y., and K. Hanawa (2005), Large-scale variabilities of wintertime wind stress curl field in the North Pacific and their relation to atmospheric teleconnection patterns, *Geophys. Res. Lett.*, 32, L10607, doi:10.1029/2004GL022330.
Jeong, J.-H., T. Ou, H. W. Linderholm, B.-M. Kim, S.-J. Kim, J.-S. Kug, D. Chen (2011), Recent recovery of the Siberian high intensity, *J. Geophys. Res.*, 116, D23102, doi:10.1029/2011JD015904.
Jin, F.-F., B. J. Hoskins (1995), The direct response to tropical heating in a baroclinic atmosphere, *J. Atmos. Sci.*, 52, 307-319.
Jo, H.-S., S.-W. Yeh, and C.-H. Kim (2013), A possible mechanism for the North Pacific regime shift in winter of 1998/1999, *Geophys. Res. Lett.*, 40, doi:10.1002/grl.50798.
Kalnay, E., et al. (1996), The NCEP/NCAR 40-year reanalysis project. *Bull. Amer. Meteor. Soc.*, 77, 437-471.
Karoly, D. J., R. A. Plumb, M. Tang (1989), Examples of the horizontal propagation of quasi-stationary waves. *J. Atmos. Sci.*, 46, 2802-2811.
Kelly, K. A., and S. Dong (2004), The relationship of western boundary current heat transport and storage to mid-latitude ocean-atmosphere interaction, in Earth's Climate (eds C. Wang, S. P. Xie and J. A. Carton), American Geophysical Union, Washington, D. C., doi:10.1029/147GM19.
Kelly, K. A., R. J. Small, R. M. Samelson, B. Qiu, T. M. Joyce, Y.-O. Kwon, and M. F. Cronin (2010), Western boundary currents and frontal air-sea interaction: Gulf stream and Kuroshio extension, *J. Climate*, 23, 5644-5667.
Kim, S.-B., I. Fukumori, T. Lee (2006), The closure of the ocean mixed layer temperature budget using level-coordinate model fields, *J. Atmos. Oceanic Tech.*, 23, 840-853.
Kwon, Y.-O., and C. Deser (2007), North Pacific decadal variability in the Community Climate System Model version 2, *J. Climate*, 20, 2416-2433.
Kwon, Y.-O., M. A. Alexander, N. A. Bond, C. Farnkignoul, H. Nakamura, B. Qiu, and L. A. Thompson (2010), Role of the Gulf Stream and Kuroshio-Oyashio systems in large-scale atmosphere-ocean interaction: A review, *J. Climate*, 23, 3249-3281.
Large, W. G., and S. G. Yeager (2004), Diurnal to decadal global forcing for ocean and sea-ice models: The data sets and flux climatologies, Technical Report TN-460+STR, NCAR, 105pp.
Latif, M., and T. P. Barnett (1994), Causes of decadal climate variability over the North Pacific and North America, *Science*, 266, 634-637.
Levitus, S., J. Antonov, T. Boyer (2005), Warming of the world ocean, 1995-2003, *Geophys. Res. Lett.*, 10.1029/2004GL021592.
Linkin, M. E., and S. Nigam (2008), The North Pacific Oscillation-west Pacific teleconnection pattern: mature-phase structure and winter impacts, *J. Climate*, 21, 1979-1997.
Madec, G. (2008), NEMO ocean engine. Note du Pôle de Modélisation, Institut

Pierre-Simon Laplace (IPSL), No 27.
Madec, G. and M. Imbard (1996), A global ocean mesh to overcome the North Pole singularity, *Climate Dyn.*, 12, 381–388.
Mantua, N. J., and S. R. Hare (2002), The Pacific Decadal Oscillation, *J. Oceanogr.*, 58, 35-44.
Miller, A. J., F. Chai, S. Chiba, J. R. Moisan, and D. J. Neilson (2004), Decadal-scale climate ecosystem interactions in the North Pacific ocean, *J. Oceanogr.*, 60, 163-188.
Mochizuki, T., H. Kida (2006), Seasonality of decadal sea surface temperature anomalies in the Northwestern Pacific, *J. Climate*, 19, 2953-2968.
Moisan, J. R., and P. P. Niiler (1998), The seasonal heat budget of the North Pacific: Net heat flux and heat storage rates (1950-1990), *J. Phys. Oceanogr.*, 28, 401-421.
Nakamura, H., G. Lin, and T. Yamagata (1997), Decadal climate variability in the North Pacific during the recent decades, Bull. Amer. Meteor. Soc., 78, 2215-2225.
Nakamura, H., T. Izumi, and T. Sampe (2002), Interannual and decadal modulations recently observed in the Pacific storm track activity and East Asian winter monsoon. *J. Climate*, 15, 1855-1874.
Nonaka, M., and S.-P. Xie (2003), Covariations of sea surface temperature and wind over the Kuroshio and its extension: evidence for ocean-to-atmosphere feedback, *J. Climate*, 16, 1404-1413.
Nonaka, M., H. Nakamura, Y. Tanimoto, T. Kagimoto, and H. Sasaki (2006), Decadal variability in the Kuroshio-Oyashio Extension simulated in an eddy-resolving OGCM, *J. Climate*, 19, 1970-1989.
Nonaka, M., H. Nakamura, Y. Tanimoto, T. Kagimoto (2008), Interannual-to-decadal variability in the Oyashio and its influence on temperature in the subarctic frontal zone: An eddy-resolving OGCM simulation, *J. Climate*, 21, 6283-6303.
Panagiotopoulos, F., M. Shahgedanova, A. Hannachi, and D. B. Stephenson (2005), Observed trends and teleconnections of the Siberian high: A recently declining center of action, *J. Climate*, 18, 1411–1422.
Pak, G., Y.-H. Park, F. Vivier, Y.-O. Kwon, and K.-I. Chang (2014), Regime-dependent nonstationary relationship between the East Asian winter monsoon and North Pacific oscillation, *J. Climate*, 27, 8185-8204.
Park, Y.-H., J.-H. Yoon, Y.-H. Youn, and F. Vivier (2012), Recent warming in the western North Pacific in relation to rapid changes in the atmospheric circulation of the Siberian high and Aleutian low systems, *J. Climate*, 25, 3476-3493.
Penduff, T., M. Juza, L. Brodeau, G.C. Smith, B. Barnier, J.-M. Molines, A.-M. Treguier and G. Madec (2010), Impact of global ocean model resolution on sea-level variability with emphasis on interannual time scales, Ocean Sci., 6, 269–284.
Plumb, R. A. (1985), On the three-dimensional propagation of stationary waves, *J. Atmos. Sci.*, 42, 217-229.
Qiu, B. (2000), Interannual variability of the Kuroshio Extension system and its impact on the wintertime SST field, J. Phys. Oceanogr., 30, 1486-1502.
Qiu, B. (2001), Kuroshio and Oyashio currents, Academic Press, doi:10.1006/rwos.2001.0350.

Qiu, B. (2003), Kuroshio Extension variability and forcing of the Pacific Decadal Oscillations: Responses and potential feedback, *J. Phys. Oceanogr.*, 33, 2465-2482.
Qiu, B., and K. A. Kelly (1993), Upper-ocean heat balance in the Kuroshio Extension region, *J. Phys. Oceanogr.*, 23, 2027-2041.
Qiu, B., and S. Chen (2005), Variability of the Kuroshio Extension jet, recirculation gyre, and mesoscale eddies on decadal time scales, *J. Phys. Oceanogr.*, 35, 2090-2103.
Qiu, B., N. Schneider, and S. Chen (2007), Coupled decadal variability in the North Pacific: an observationally constrained idealized model, *J. Climate*, 20, 3602-3620.
Rayner, N. A., D. E. Parker, E. B. Horton, C. K. Folland, L. V. Alexander, D. P. Rowell, E. C. Kent, and A. Kaplan (2003), Global analyses of sea surface temperature, sea ice, and night marine air temperature since the late nineteenth century. *J. Geophys. Res.*, 108, doi:10.1029/2002JD002670.
Reynolds, R.W., N.A. Rayner, T.M. Smith, D.C. Stokes, and W. Wang (2002), An improved in situ and satellite SST analysis for climate, *J. Climate*, 15, 1609-1625.
Rodionov, S. N. (2004), A sequential algorithm for testing climate regime shifts. *Geophys. Res. Lett.*, 31, L09204, doi:10.1029/2004GL019448.
Rodionov, S.N. (2006), Use of prewhitening in climate regime shift detection, *Geophys. Res. Lett.*, 33, L12707, doi:10.1029/2006GL025904.
Rodionov, S.N., and J.E. Overland (2005), Application of a sequential regime shift detection method to the Bering Sea ecosystem, ICES *J. Mar. Sci.*, 62, 328-332.
Sainz-Trapaga, S. and T. Sugimoto (2000), Three-dimensional velocity field and cross-frontal water exchange in the Kuroshio Extension, *J. Oceanogr.*, 56, 79-92.
Seo, H., R. Murtugudde, M. Jochum, A. J. Miller (2008), Modeling of mesoscale coupled ocean-atmosphere interaction and its feedback to ocean in the western Arabian Sea, *Ocean Modelling*, 25, 120-131.
Schneider, N., and A. J. Miller (2001), Predicting western North Pacific Ocean climate, *J. Climate*, 14, 3997-4002.
Schneider, N., A. J. Miller, and D. W. Pierce (2002), Anatomy of North Pacific decadal variability, *J. Climate*, 15, 586-605.
Seager, R., Y. Kushnir, N. H. Naik, M. A. Cane, and J. Miller (2001), Wind-driven shifts in the latitude of the Kuroshio-Oyashio Extension and generation of SST anomalies on decadal timescales, *J. Climate*, 14, 4249-4265.
Seo, H., Y.-O. Kwon, and J.-J. Park (2014a), On the effect of the East/Japan Sea SST variability on the North Pacific atmospheric circulation in a regional climate model, *J. Geophys. Res.*, 119, doi:10.1002/2013JD020523.
Seo, Y., S. Sugimoto, K. Hanawa (2014b), Long-term variations of the Kuroshio extension path in winter : meridional movement and path state change, *J. Climate*, 27, 5929-5940.
Stevenson J. W., P. P. Niiler (1983), Upper ocean heat budget during the Hawaii-to-Tahiti shuttle experiment, *J. Phys. Oceanogr.*, 13, 1894-1907.
Sugimoto, S., and K. Hanawa (2009), Decadal and interdecadal variations of the Aleutian low activity and their relation to upper oceanic variations over the North Pacific, *J. Meteorol. Soc. Jpn.*, 87, 601-614.
Sugimoto, S., and K. Hanawa (2011), Roles of SST anomalies on the wintertime

turbulent heat fluxes in the Kuroshio-Oyashio confluence region: Influences of warm eddies detached from the Kuroshio Extension, *J. Climate*, 24, 6551-6561.

Sugimoto, S., and S. Kako (2016), Decadal variation in winter mixed layer depth south of the Kuroshio Extension and its influence on winter mixed layer temperature, *J. Climate*, 29, 1237-1252.

Taguchi, B., S.-P. Xie, N. Schneider, M. Nonaka, H. Sasaki, and Y. Sasai (2007), Decadal variability of the Kuroshio Extension: Observations and an eddy-resolving model hindcast, *J. Climate*, 20, 2357-2377.

Takaya, K., and H. Nakamura (2005a), Mechanisms of intraseasonal amplification of the cold Siberian high. *J. Atmos. Sci.*, 62, 4423-4440.

Takaya, K., and H. Nakamura (2005b), Geographical dependence of upper-level blocking formation associated with intraseasonal amplification of the Siberian high. *J. Atmos. Sci.*, 62, 4441-4449.

Takaya, K., and H. Nakamura (2013), Interannual variability of the East Asian winter monsoon and related modulations of the planetary waves. *J. Climate*, 26, 9445-9461.

Tanimoto, Y., H. Nakamura, T. Kagimoto, and S. Yamane (2003), An active role of extratropical sea surface anomalies in determining anomalous turbulent heat flux, *J. Geophys. Res.*, 108, doi:10.1029/2002JC001750.

Tatebe, H., and I. Yasuda (2005), Interdecadal variations of the coastal Oyashio from the 1970s to the early 1990s, *Geophys. Res. Lett.*, 32, doi:10.1029/2005GL022605.

Tian, Y., H. Kidokoro, T. Watanabe, N. Iguchi (2008), The late 1980s regime shift in the ecosystem of Tsushima warm current in the Japan/East Sea: Evidence from historical data and possible mechanisms. *Prog. Oceanogr.*, 77, 127-145.

Tomita, T., S.-P. Xie, and M. Nonaka (2002), Estimates of surface and subsurface forcing for decadal sea surface temperature variability in the mid-latitude North Pacific, *J. Meteorol. Soc. Jpn.*, 80, 1289-1300.

Trenberth, K. E. (2011), Changes in precipitation with climate change, *Climate Res.*, 47, 123-138.

Trenberth, K. E., and D. A. Paolino (1980), The Northern Hemisphere sea level pressure data set: Trends, errors, and discontinuities. *Mon. Wea. Rev.*, 108, 855-872.

Trenberth, K. E., and J. W. Hurrell (1994), Decadal atmosphere – ocean variation in the Pacific. *Climate Dyn*., 9, 303– 319.

Vimont, D. J., J. M. Wallace, and D. S. Battisti (2003), The seasonal footprinting mechanism in the Pacific: Implications for ENSO. *J. Clim.*, 16, 2668-2675.

Vivier, F., K. A. Kelly, and L.A. Thompson (2002), Heat budget in the Kuroshio Extension region: 1993-99, *J. Phys. Oceanogr.*, 32, 3436-3454.

Wallace, J. M., and D. S. Gutzler (1981), Teleconnections in the geopotential height field during the Northern Hemisphere winter, *Mon. Wea. Rev.*, 109, 784-812.

Wang, L., and W. Chen (2010), How well do existing indices measure the strength of the East Asian winter monsoon? *Adv. Atmos. Sci*., 27, 855-870.

Wang, L., and W. Chen (2014a), The East Asian winter monsoon: Re-amplification in the mid-2000s. *Chinese Sci. Bull.*, 59, 430-436.

Wang, L., and W. Chen (2014b), An intensity index for the East Asian winter monsoon, *J. Climate*, 27, 2361-2374.

Wang, L., W. Chen, and R. Huang (2007), Changes in the variability of North Pacific Oscillation around 1976/1976 and its relationship with East Asian winter climate. *J. Geophys. Res.*, 112, doi:10.1029/2006JD008054.

Wang, L., R. Huang, L. Gu, W. Chen, and L. Kang (2009), Interdecadal variations of the East Asian winter monsoon and their association with quasi-stationary planetary wave activity. *J. Climate*, 22, 4860-4872.

Wang, L., W. Chen, W. Zhou, J. C. J. Chan, D. Barriopedro, and R. Huang (2010), Effect of the climate shift around mid 1970s on the relationship between wintertime Ural blocking circulation and East Asian climate. *Int. J. Climatol.*, 30, 153–158.

Wu, R., and B. P. Kirtman (2007), Regimes of seasonal air-sea interaction and implications for performance of forced simulations, *Climate Dyn.*, 29, 393-410.

Wu, R., and J. L. Kinter III (2010), Atmosphere-ocean relationship in the midlatitude North Pacific: Seasonal dependence and east-west contrast, *J. Geophys. Res.*, 115, D06101, doi:10.1029/2009JD012579.

Wu, R., B. P. Kirtman, and K. Pegion (2006), Local air-sea relationship in observations and model simulations, *J. Climate*, 19, 4914-4932.

Yamamoto, M., and N. Hirose (2011), Possible modification of atmospheric circulation over the northwestern Pacific induced by a small semi-enclosed ocean. *Geophys. Res. Lett.*, 38, L03804, doi:10.1029/2010GL046214.

Yang, S., K. Lau, and K. Kim (2002), Variations of the East Asian jet stream and Asian–Pacific–American winter climate anomalies. *J. Climate*, 15, 306–325.

Yeh, S.-W., and C.-H. Kim (2010), Recent warming in the Yellow-East China Sea during winter and the associated atmospheric circulation. *Cont. Shelf Res.*, 30, 1428-1434.

Yeh, S.-W., Y.-J. Kang, Y. Noh, and A. J. Miller (2011), The North Pacific climate transitions of the winters of 1976/77 and 1988/89, *J. Climate*, 24, 1170-1183.

Yu, L., X. Jin, R. A. Weller (2008), Multidecade global datasets from the objectively analyzed air-sea fluxes (OAFlux) project: latent and sensible heat fluxes, ocean evaporation, and related surface meteorological variables, Woods Hole Oceanographic Institution, OAFlux project technical report, OA-2008-01, 64pp, Woods Hole, Massachusetts.

Yulaeva, E., N. Schneider, D. W. Pierce, and T. P. Barnett (2001), Modeling of North Pacific climate variability forced by oceanic heat flux anomalies, *J. Climate*, 14, 4027-4046.

국문 초록

북태평양 서안 경계 해역의 상층 열용량 장기 변동 기작 연구

박균도
지구환경과학부 (물리해양학), 서울대학교

관측 및 재분석 자료를 통해 북서태평양 해역의 겨울철 상층 해양의 열용량 장기변동성과 그 기작을 조사하였다. 동아시아 동계계절풍(EAWM)과 북태평양진동(NPO)의 상관관계 및 그들이 해표면 수온(SST)에 미치는 영향은 1987/88년도 부근으로 갑작스럽게 체제 변환 한다. 1973-87년 기간 동안에는 EAWM과 NPO는 유의미한 상관관계를 보이지만, 1988-2002년 기간 동안에는 0에 가까운 상관계수를 보인다. 이러한 비정상적인(nonstationary) 관계는 1988년 이후 시베리아 고기압의 약화와 그와 동시에 일어나는 NPO 패턴의 동진과 관련된 것으로 보인다. 더불어 EAWM과 NPO의 겨울철 북서태평양 지역 SST에 미치는 영향도 1988년 부근을 기점으로 하여 강한 영향에서 약한 영향으로 변화한다. 고해상도 해양 순환 모델 자료를 이용해 쿠로시오-오야시오 익스텐전 해역의 상층 400m의 열수지분석 결과, 겨울철 수년-수십년 주기의 열용량 변화율(HSR)의 변동성은 해양-대기 열 플럭스보다는 해양 열 이류에 의해 대체로 결정되는데, 특히 1990년 이후 SST 변동성이 작아지며 열 플럭스의 변동성이 작아져 이류의 역할이 상대적으로 훨씬 커지게 된다. 이 지역에서 열 플럭스는 해양에 의해 생성된 수온 anomaly를 줄이는 역할을 주로 하는 것으로 나타났다. 해양의 수온 anomaly는 주로 Oyashio 프런트의 장기적인 자오선 방향 움직임에 의해서 생성이 되는데, 이 프런트의 움직임은 서태평양양 텔레커넥션(WP) 패턴과 태평양-북아메리카 텔레커넥션 패턴(PNA)과 주로 연관이 되어 이들 패턴들의 변동성으로부터 수년 지연된 반응으로 나타난다.

주요어: 열수지분석, 장기변동성, 해양 열 이류, 해양-대기 열 플럭스, 쿠로시오-오야시오 익스텐전, 체제 변환